

AD-A243 762



✓
②

NAVAL POSTGRADUATE SCHOOL Monterey, California



DTIC
ELECTE
DEC 31 1991
S D D

THESIS

HIGH-FREQUENCY METEOROLOGICAL PHENOMENA
OBSERVED WITH THE NAVAL POSTGRADUATE
SCHOOL'S
HIF DOPPLER WIND PROFILER

by

Daniel H. Streed

December 1990

Thesis Advisor

Wendell A. Nuss

Approved for public release; distribution is unlimited.

91-19140



91 1227 012

Unclassified

security classification of this page

REPORT DOCUMENTATION PAGE				
1a Report Security Classification Unclassified			1b Restrictive Markings	
2a Security Classification Authority			2 Distribution/Availability of Report	
2b Declassification/Downgrading Schedule			Approved for public release; distribution is unlimited.	
4 Performing Organization Report Number(s)			5 Monitoring Organization Report Number(s)	
6a Name of Performing Organization Naval Postgraduate School		6b Office Symbol (if applicable) 35	7a Name of Monitoring Organization Naval Postgraduate School	
6c Address (city, state, and ZIP code) Monterey, CA 93943-5000			7b Address (city, state, and ZIP code) Monterey, CA 93943-5000	
8a Name of Funding/Sponsoring Organization		8b Office Symbol (if applicable)	9 Procurement Instrument Identification Number	
8c Address (city, state, and ZIP code)			10 Source of Funding Numbers	
			Program Element No	Project No
			Task No	Work Unit Accession No
11 Title (include security classification) HIGH-FREQUENCY METEOROLOGICAL PHENOMENA OBSERVED WITH THE NAVAL POSTGRADUATE SCHOOL'S UHF DOPPLER WIND PROFILER				
12 Personal Author(s) Daniel H. Streed				
13a Type of Report Master's Thesis		13b Time Covered From To	14 Date of Report (year, month, day) December 1990	15 Page Count 130
16 Supplementary Notation The views expressed in this thesis are those of the author and do not reflect the official policy or position of the Department of Defense or the U.S. Government.				
17 Cosati Codes			18 Subject Terms (continue on reverse if necessary and identify by block number)	
Field	Group	Subgroup	Doppler Wind Profiler, Wind Profiler, Doppler Radar	
19 Abstract (continue on reverse if necessary and identify by block number) A UHF clear-air Doppler radar wind profiler was purchased by the Naval Postgraduate School and began operation in late-March of 1990. The identification of numerous meteorological phenomena utilizing UHF Doppler radar wind profilers has been successfully documented; however, published work to-date has concentrated on interpretation of hourly-consensus data. But with the onset of improved technology, it is now possible to retrieve reliable data within the hourly period. This study examines the quality of the six-minute data through statistical analysis and determines the overall accuracy of the School's profiler. Specifically, the performance of the profiler is compared with rawinsonde data, other profiler comparison studies, as well as the contract specifications. The study also looks at overall performance of UHF Doppler radar profiler in an environment characterized by a strong marine inversion. Finally the study presents evidence that meteorological phenomena which exhibit time scales on the order of minutes can be observed using the six-minute profiler data.				
20 Distribution/Availability of Abstract <input checked="" type="checkbox"/> unclassified/unlimited <input type="checkbox"/> same as report <input type="checkbox"/> DTIC users			21 Abstract Security Classification Unclassified	
22a Name of Responsible Individual Wendell A. Nuss			22b Telephone (include Area code) (408) 646-2768	22c Office Symbol MR/NU

DD FORM 1473,84 MAR

83 APR edition may be used until exhausted
All other editions are obsolete

security classification of this page

Unclassified

Approved for public release; distribution is unlimited.

High-Frequency Meteorological Phenomena
Observed with the Naval Postgraduate School's
UHF Doppler Wind Profiler

by

Daniel H. Streed
Lieutenant Commander, United States Navy
B.S., United States Naval Academy, 1980

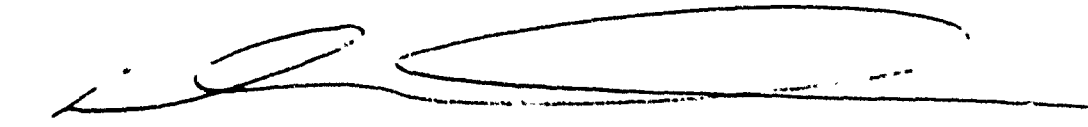
Submitted in partial fulfillment of the
requirements for the degree of

MASTER OF SCIENCE IN METEOROLOGY AND PHYSICAL
OCEANOGRAPHY

from the


NAVAL POSTGRADUATE SCHOOL
December 1990

Author:

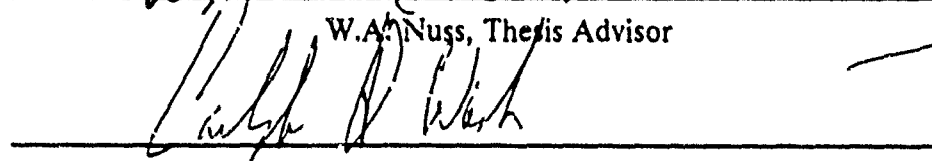


Daniel H. Streed

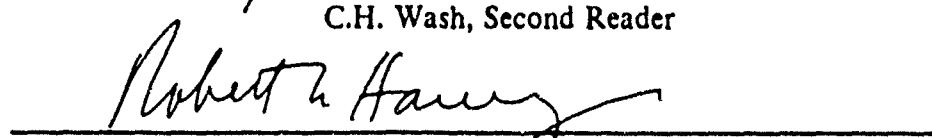
Approved by:



W.A. Nuss, Thesis Advisor



C.H. Wash, Second Reader

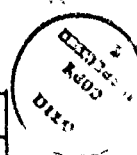


Robert L. Haney, Chairman,
Department of Meteorology

ABSTRACT

A UHF clear-air Doppler radar wind profiler was purchased by the Naval Postgraduate School and began operation in late-March of 1990. The identification of numerous meteorological phenomena utilizing UHF Doppler radar wind profilers has been successfully documented; however, published work to-date has concentrated on interpretation of hourly-consensus data. But with the onset of improved technology, it is now possible to retrieve reliable data within the hourly period. This study examines the quality of the six-minute data through statistical analysis and determines the overall accuracy of the School's profiler. Specifically, the performance of the profiler is compared with rawinsonde data, other profiler comparison studies, as well as the contract specifications. The study also looks at overall performance of UHF Doppler radar profiler in an environment characterized by a strong marine inversion. Finally the study presents evidence that meteorological phenomena which exhibit time scales on the order of minutes can be observed using the six-minute profiler data.

Accession For	
NTIS CRA&I	<input checked="" type="checkbox"/>
DTIC TAB	<input type="checkbox"/>
Unannounced	<input type="checkbox"/>
Justification	
By	
Distribution /	
Availability Codes	
Dist	Avail and/or Special
A-1	



ACKNOWLEDGMENTS

I express my gratitude to Professor Wendell A. Nuss and Professor Carlyle H. Wash for their advice and guidance during the course of most of this work and to Dr. William Shaw for his guidance and helpful discussions from project initiation. I would like to especially thank Mr. Dick Lind who provided countless hours of programming and technical guidance to the study.

TABLE OF CONTENTS

I. INTRODUCTION	1
II. BACKGROUND	7
A. THEORY OF PROFILER OPERATION	7
B. PROFILER DATA PROCESSING	11
C. PROCESSING OF RAWINSONDE DATA	16
D. KNOWN SOURCES OF PROFILER ERROR	17
III. DATA ANALYSIS	24
A. COMPARISON OF MANUFACTURER'S CONSENSUS TO RAWINSONDE DATA	24
B. INVESTIGATION OF VARIABLES AFFECTING DATA QUALITY ..	36
C. INVESTIGATION OF VARIABLES AFFECTING CONSENSUS	47
IV. METEOROLOGICAL ANALYSIS USING SIX-MINUTE PROFILER. DATA	50
A. VELOCITY AND VELOCITY PERTURBATION FIELD ANALYSIS ..	50
B. THERMAL ADVECTION FROM SIX-MINUTE DATA	54
C. SYNOPTIC OVERVIEW FOR 02-03 MAY 1990	59
D. A PROBABLE EXPLANATION OF OBSERVED HIGH-FREQUENCY PHENOMENA	61
V. CONCLUSIONS	70
VI. RECOMMENDATIONS	71
A. MEASUREMENT VALIDATION AND DATA QUALITY IMPROVE- MENT	71
B. ACADEMIC RESEARCH	71
APPENDIX A. EQUIPMENT CONFIGURATION	73
A. WIND PROFILER	73

B. RAWINSONDE	74
APPENDIX B. DERIVATION OF THE RADAR EQUATION FOR CLEAR AIR PROFILERS	77
APPENDIX C. RADAR WIND PROFILER TRIGONOMETRY	82
APPENDIX D. CONSENSUS TECHNIQUES	85
A. CONSENSUS AVERAGING	85
B. COMBINED MEDIAN FILTER AND SHEAR CHECK	87
C. OPTIMAL INTERPOLATION	90
D. RECURSIVE FILTER	91
APPENDIX E. INDIVIDUAL PROFILER COMPARISONS AND RAWINSONDE LAUNCHINGS	95
APPENDIX F. NPS PROFILER SITE SURVEY RECORD AND LAYOUT .	112
APPENDIX G. HIGH-FREQUENCY METEOROLOGICAL DATA	114
LIST OF REFERENCES	115
INITIAL DISTRIBUTION LIST	118

LIST OF TABLES

Table 1. PROFILER PARAMETERS	15
Table 2. STATISTICAL ANALYSIS OF DIFFERENCES BETWEEN RAWINSONDE AND PROFILER-DERIVED VELOCITIES FOR ALL NINE RAWINSONDE LAUNCHES	35
Table 3. S/N THRESHOLD STATISTICS	38
Table 4. SALINAS HOURLY SURFACE WEATHER OBSERVATIONS	69
Table A-1. RAWINSONDE METEOROLOGICAL SENSOR TECHNICAL DATA	76
Table D-1. FUNCTIONAL CONSENSUS PROCESS:	86

LIST OF FIGURES

Fig. 1. Profiler Sites for the NWS Demonstration Network	2
Fig. 2. Topographical Map of area Surrounding NPS Profiler Site	3
Fig. 3. Configuration of the NPS Profiler Site	4
Fig. 4. Illustration of the Generation, Beam Pattern, and Scattering	9
Fig. 5. Illustration of Refractive Index Structure Sampled by the	10
Fig. 6. Typical Vertical Profile of 36 Range Gate Frequency-Power Spectra	12
Fig. 7. Schematic Diagram of the Primary Signal Processing Steps for the Profiler	13
Fig. 8. Functional Diagram of the Time Domain Averaging (TDA) Process	14
Fig. 9. Functional Rawinsonde and Profiler Gate Spacing	18
Fig. 10. Sample of FAA Traffic Control Radar Contamination of NPS Profiler ...	19
Fig. 11. Sample of Velocity Folding in the NPS Profiler	20
Fig. 12. Example of a Double Peak in NPS Profiler Spectra caused by Rain	22
Fig. 13. Example of Rawinsonde Balloon Interference in the NPS Profiler	23
Fig. 14. Profiler-Rawinsonde Comparison Winds for 0100 UTC 20 April 1990 ...	28
Fig. 15. Rawinsonde Sounding for 0100 UTC 20 April 1990	29
Fig. 16. Typical Comparison Plot of Rawinsonde vs Profiler U-Velocity Component (Profiler in Low-Mode)	30
Fig. 17. Typical Comparison Plot of Rawinsonde vs Profiler V-Velocity Component (Profiler in Low-Mode)	30
Fig. 18. Typical Comparison Plot of Rawinsonde vs Profiler U-Velocity Component (Profiler in High-Mode)	31
Fig. 19. Typical Comparison Plot of Rawinsonde vs Profiler V-Velocity Component (Profiler in High-Mode)	31
Fig. 20. Oakland (72493) Sounding for 1200 UTC 06 April 1990	32
Fig. 21. Example of Low Mode Spectra	33
Fig. 22. Sample Low Mode Spectra Depicting Jet Stream Structure	33
Fig. 23. Scatter Plot of Low-Mode Profiler vs Rawinsonde Velocity	34
Fig. 24. Scatter Plot of High-Mode Profiler vs Rawinsonde Velocity	34
Fig. 25. Profiler Hourly-consensus Wind Data from 0605 to 1703 UTC 02 May 1990	37
Fig. 26. Signal-to-Noise Threshold Determination	39
Fig. 27. Plot of Various Power Difference Thresholds Between Off-vertical Beams .	41

Fig. 28. Plot of Various Power Difference Thresholds Between Off-vertical Beams .	42
Fig. 29. Plot of Beam Power Difference vs Velocity Standard Deviation and Mean Plot	43
Fig. 30. Example Spectrum Depicting Velocity Shift due to Double Peak	44
Fig. 31. Comparison of Data Quality Techniques with Wind Profiles	45
Fig. 32. Representative Consensus Data from TCM-90	46
Fig. 33. Comparable Hourly Consensus Profiles from 02 May 1990.	49
Fig. 34. Plot of NPS Profiler Vertical Wind Component for 02 May 1990	52
Fig. 35. Plot of NPS Profiler Horizontal Wind Perturbations for 02 May 90	53
Fig. 36. Temperature Advection Field	58
Fig. 37. Packing of Isotherms due to Turbulence in a Stratified Gas	59
Fig. 38. Vertical Velocity Field	60
Fig. 39. NMC 500 mb Analysis for 1200 UTC 02 May 1990	62
Fig. 40. NMC Surface Pressure Analysis for 1500 UTC 02 May 1990	63
Fig. 41. NPS Radar Profiler Hourly-consensus Data for 02 May 1990	64
Fig. 42. NPS Radar Profiler Hourly-consensus Data for 02 May 1990	65
Fig. 43. NPS Radar Profiler Hourly-consensus Data for 03 May 1990	66
Fig. 44. NPS Radar Profiler Hourly-consensus Data for 03 May 1990	67
Fig. 45. NPS Radar Profiler Six-Minute Data for 02 May 1990	68
Fig. A-1. Functional Diagram of Wind Profiler	73
Fig. A-2. Vaisala DigiCORA Upper Air Sounding System	75
Fig. B-1. Illustration of Geometry for Beam Volume Calculations	78
Fig. C-1. Horizontal Velocity Calculation from the Three Radial Velocities	82
Fig. C-2. Trigonometry Relating Coordinate Axes in the Horizontal Plane	84
Fig. C-3. Trigonometry of Axis Translation for Site Correction	84
Fig. D-1. Data Points from which Median is calculated in the Median Check ..	88
Fig. D-2. Three examples of the vertical consistency	89
Fig. D-3. Schematic of Successive Elimination Process	92
Fig. D-4. Data Search Strategy for Optimal Interpolation Analysis (OI) QC ...	93
Fig. E-1. Profiler-Rawinsonde Wind Comparisons for 20 April 1990	95
Fig. E-2. Rawinsonde Sounding from 20 April 1990	96
Fig. E-3. Profiler-Rawinsonde Wind Comparisons for 1600 UTC 23 April 1990 .	97
Fig. E-4. Rawinsonde Sounding from 1600 UTC 23 April 1990	98
Fig. E-5. Profiler-Rawinsonde Wind Comparisons for 1900 UTC 23 April 1990 .	99
Fig. E-6. Rawinsonde Sounding from 1900 UTC 23 April 1990	100

Fig. E-7. Profiler-Rawinsonde Wind Comparisons for 2000 UTC 02 May 1990	101
Fig. E-8. Rawinsonde Sounding from 1900 UTC 02 May 1990	102
Fig. E-9. Profiler-Rawinsonde Wind Comparisons for 0100 UTC 03 May 1990	103
Fig. E-10. Rawinsonde Sounding from 0100 UTC 03 May 1990	104
Fig. E-11. Profiler-Rawinsonde Wind Comparisons for 0700 UTC 03 May 1990	105
Fig. E-12. Rawinsonde Sounding from 0700 UTC 03 May 1990	106
Fig. E-13. Profiler-Rawinsonde Wind Comparisons for 1300 UTC 03 May 1990	107
Fig. E-14. Rawinsonde Sounding from 1300 UTC 03 May 1990	108
Fig. E-15. Profiler-Rawinsonde Wind Comparisons for 1900 UTC 03 May 1990	109
Fig. E-16. Rawinsonde Sounding from 1900 UTC 03 May 1990	110
Fig. E-17. Rawinsonde Launch Locations	111
Fig. F-1. Atmospheric Profiler, Fort Ord Survey Observation Sketch	113
Fig. G-1. Recorded Data for 03 May 1990.	114

I. INTRODUCTION

Radar technology has undergone continuous refinement since it was first developed early in this century. The development of the modern wind profiler is an outgrowth of research done in the 1920's and 1930's with radars designed to probe the ionosphere. This research was driven by the need to calculate HF radio interference, for example, from the velocity of the free-electrons and ions. Interest faded through the late 1930's. It was not until World War II that work began again with short-wave radars--hoping again for the chance to utilize the ionosphere successfully for communications. Although the initial applications of radar were for communications research and detecting solid objects, such as warships, it was soon discovered that radar could also detect hydrometeors in the atmosphere. It was not until the early 1970's that strong returns were first received in "clear air" (Woodman and Guillen, 1974).

In the late 1970's the first significant work with profilers began in the United States. While the early wind profilers were designed to sample the stratosphere and even the mesosphere, today's versions concentrate on profiling the troposphere and lower stratosphere. The National Oceanic and Atmospheric Administration (NOAA) Environmental Research Laboratory in Boulder, Colorado began research with 50 MHz and 400 MHz radars in the early 1980's and since then have been operating a small network of wind profilers in Colorado (see inset within Fig. 1).

For the past seven years the Denver Weather Service Forecast Office has had access to the profiler network and found the profiler data to be very useful in forecasting winter storms. Although the most experience dealing with wind profilers and their subsequent network capabilities has been in the Colorado area, it is expected that profilers will be extremely useful in other climatic regions.

The NOAA Wave Propagation Laboratory is in the process of setting up a demonstration network of 30 wind profilers by 1991 (locations depicted in Fig. 1 from van de Kamp (1988)). The first UNISYS-produced profiler was officially accepted by NOAA in August of 1989, located at Platteville, Colorado. As the network becomes complete, forecasters and researchers will have the opportunity to compute and evaluate hourly time series of wind profiles and derived kinematic quantities.

The Naval Postgraduate School has purchased a 404 MHz profiler as part of the Marine Atmospheric Measurements Lab in Spanagel Hall. The transceiver antenna was

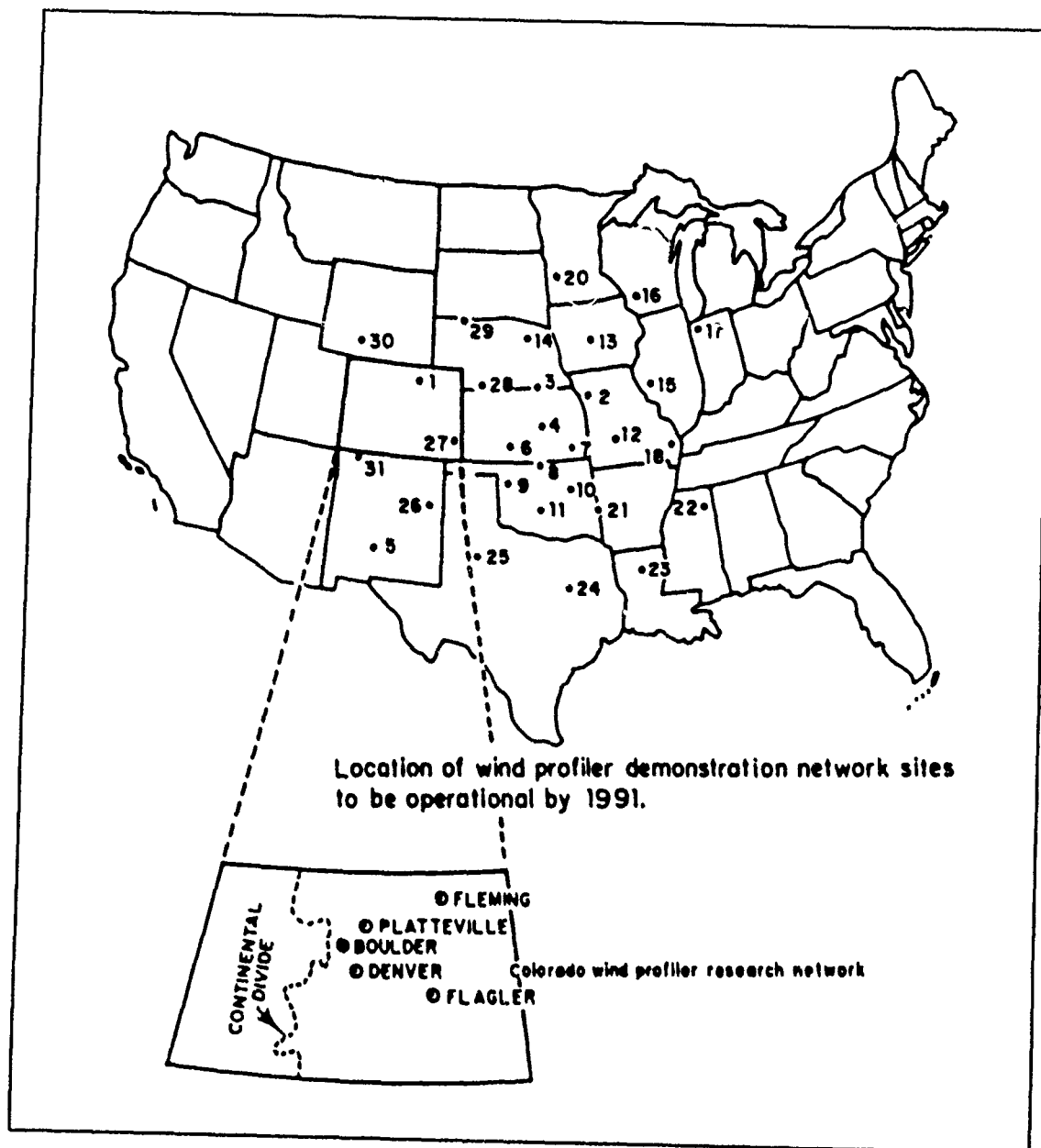


Fig. 1. Profiler Sites for the NWS Demonstration Network: (Source: van de Kamp (1988)).

installed at Fritzsche Field, Fort Ord. The area topography and geographical position of the NPS profiler are presented in Fig. 2. Figure 3 portrays details of the NPS profiler site and flat-bed antenna array. The profiler was operational by late-March 1990.

The NPS profiler was the first UHF profiler placed on the California central coast, and among the first on the North American west coast. The California central coast

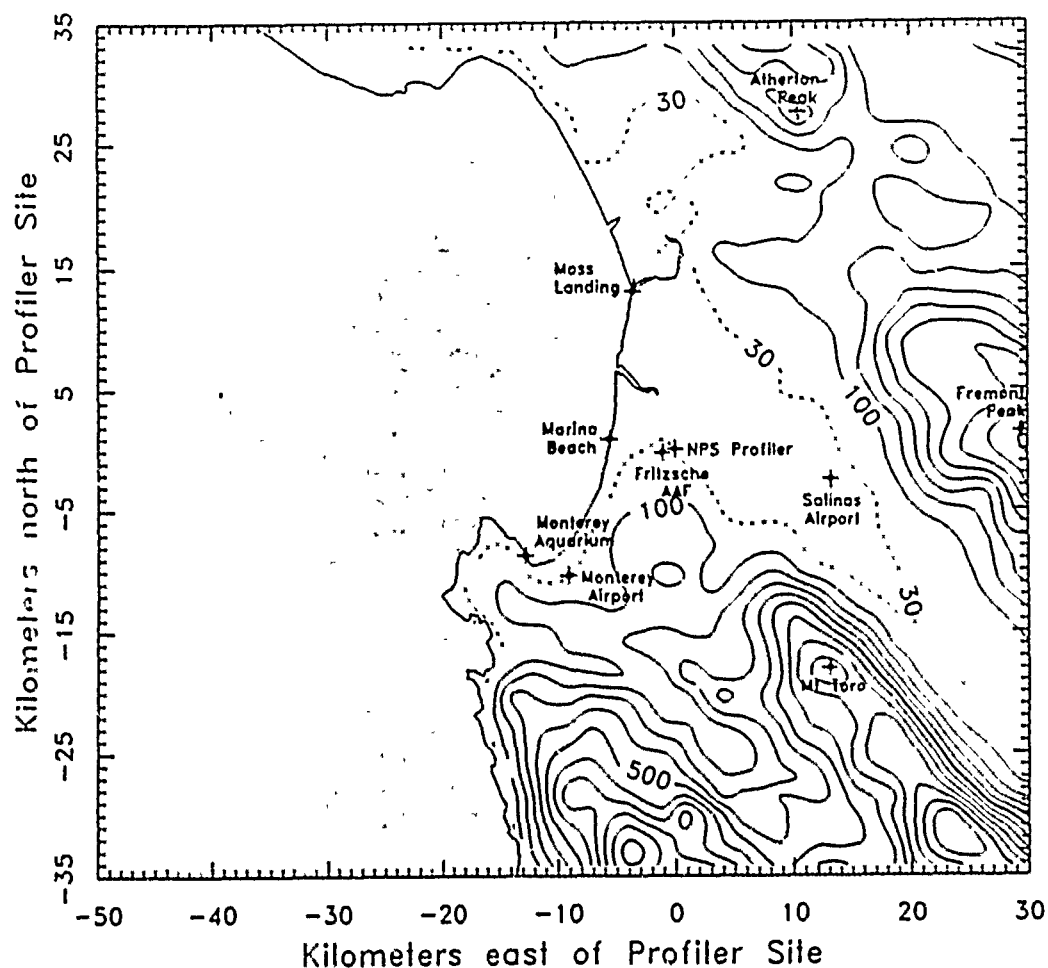


Fig. 2. Topographical Map of area Surrounding NPS Profiler Site

provides a unique environment influenced by cold-water upwelling, a persistent subsidence of dry air due to the eastern Pacific subtropical ridge, and the complex interaction of topography and the land/sea breeze circulation. Consequently, there is need to determine the feasibility of operating a 404 MHz radar profiler in an environment characterized by a strong marine inversion.

Significant work with profiler data has already been accomplished, especially by Kuo *et al.* (1987) utilizing the Colorado network and Forbes *et al.* (1989 and 1990) with the Penn State profilers. Kuo *et al.* found that retrieved temperature derived from a network

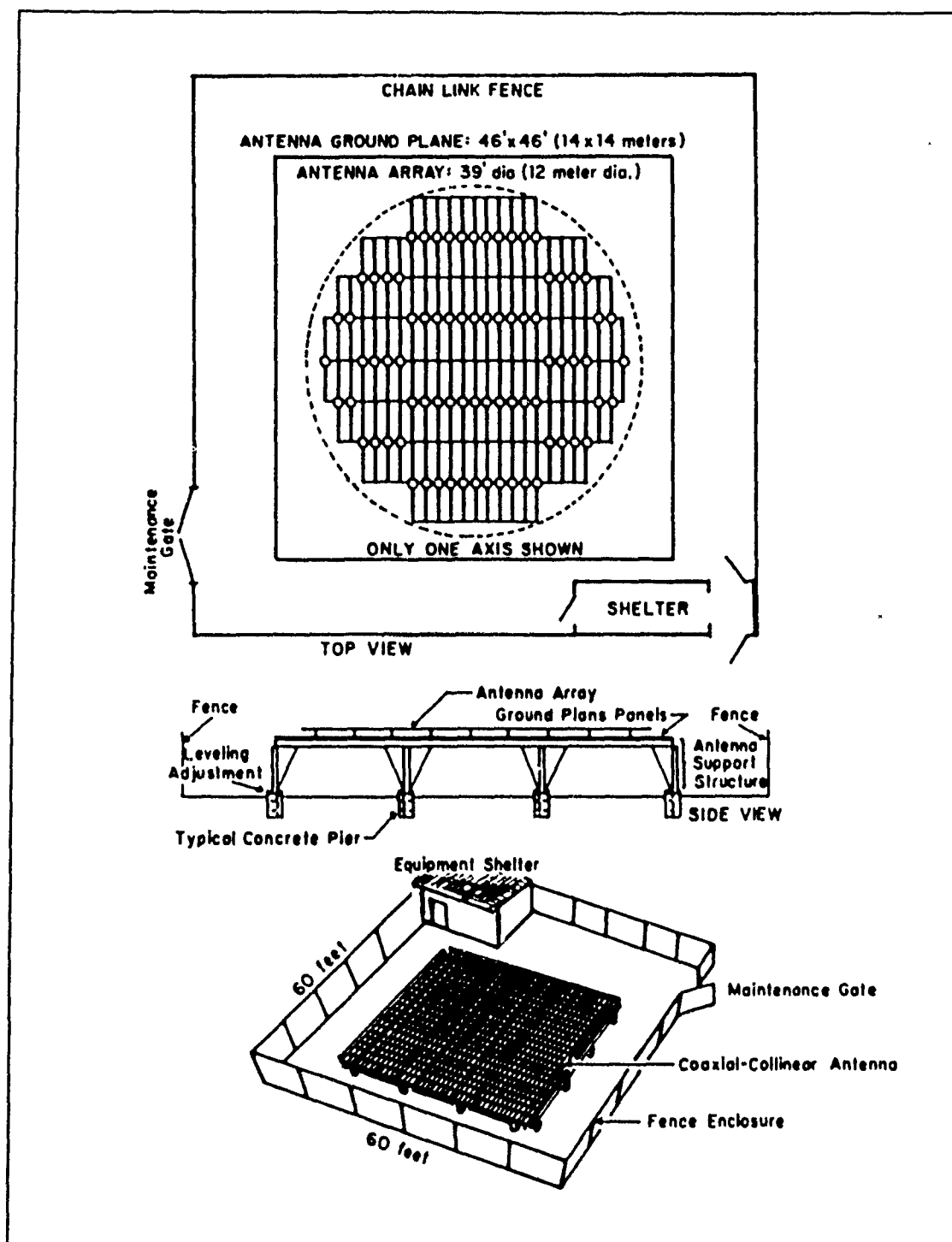


Fig. 3. Configuration of the NPS Profiler Site: (Source: Tycho Technology, Inc., Wind Profiling, 1988)

of VHF wind profilers was significantly more accurate than the direct temperature measurement from a combined satellite- and ground-based microwave radiometric system. Forbes *et al.* documented how wind profiler data together with conventional National Weather Service rawinsonde data proved quite helpful in understanding the cause of subtle weather systems seen in satellite imagery. Forbes *et al.* also examined the utility of profiler-derived temperature gradients, temperature advections and lapse rate gradient information. Both the Colorado and Pennsylvania network of profilers have been operating for nearly a decade and, subsequently, numerous works, beyond which can be cited in this study, have analyzed important aspects of their respective local meteorology, including frontal passages and convective storms.

Published studies to-date have concentrated on interpretation of hourly-consensus data. Forbes *et al.* (1990) discusses, although only briefly, interhour fluctuations detected with the Penn State VHF profiler, but their emphasis is on analyzing significant mesoscale weather. The primary objective of this study, in contrast, is examination of the potential for a clear-air wind profiling Doppler radar to observe small-scale, high-frequency meteorological events--in other words, information within the time scale of one hour, down to time scales of six minutes in the case of the NPS radar. To meet this objective it will be necessary to first ensure data from the individual profiles are as reliable as possible, i.e., throw out the "bad" data. This data quality process will hopefully provide an improved capability to obtain good representative data beyond that which the manufacturer's software provides. It is also hoped that by improving the individual profiles that the hourly-consensus will be improved.

A secondary objective of this study is to document the performance, including accuracy, of the NPS profiler operating in an environment characterized by a strong marine inversion. Determination of system accuracy is important in this study in order to lend insight into the thermodynamic relationships presented later. The study will also compare the data accuracy to other profiler and rawinsonde studies.

Finally, this study hopefully will expose many students and instructors to the capability of a UHF radar profiler, in addition to providing future students the necessary groundwork to expand and analyze specific meteorological phenomena with high-temporal resolution and on a real-time basis.

This study documents research performed during the period of initial operation, 30 March to 05 May 1990. The period was selected for several reasons. First, the profiler was scheduled to be part of Tropical Cyclone Motion experiment (TCM-90) in southeast Asia, which meant disassembly by no later than June 1990. Second, a transmitter am-

plifier failed one month prior to scheduled disassembly, and the amplifier subsequently had to be removed and sent back to the manufacturer. The period left (a little more than a month) was further reduced in length by spurious software failures and power outages.

Several other factors limited the ability to conduct a detailed meteorological investigation. The initial operating period was never meant to be analyzed in such detail as this study is directed. Therefore, the ancillary data-gathering systems such as SODAR and high-frequency pressure and humidity recording devices, were never arranged. Rawinsondes were the only equipment configured for this experiment, but at the last moment the primary rawinsonde system allotted for comparison studies failed. A secondary unit was available but could be used only intermittently, as it had to be scheduled around cruise course requirements. In the end, only nine successful rawinsonde launchings were available, and five of those were from onboard the student cruise boat west outside Monterey Bay.

The equipment configuration used for this study is described in Appendix A. The Radio-Acoustic Sounding System (RASS) modification for the wind profiler was not installed for this period, and the software for C_N computations was not yet available from the manufacturer.

II. BACKGROUND

A. THEORY OF PROFILER OPERATION

The wind profiler, like all radars, detects the transmission or reflection of electromagnetic radiation at certain frequencies, or wavelengths. A phenomenon known as Bragg scatter is critical to receiving the necessary backscattered signal strength in clear air. Bragg scatter comes about in two ways: (1) through the scatter from a surface or layer with a wave speed which is resonant to the cosine of the incident angle of the transmitted radar pulse, or (2) through the presence of multiple refractive layers spaced at the scales of turbulent energy as is in the case of UHF profilers--404 MHz falls in the Ultra High Frequency (UHF) range. Although all scales of turbulence scatter energy, it is not until the turbulence scales approach $1/2$ the transmitted wavelength, or 37 cm in the case of the 404 MHz profilers, that the scattered energy waves interact constructively.

Profilers depend upon the scattering of electromagnetic energy by minor irregularities in the index of refraction of air. Energy is first radiated at 404 MHz from a coaxial colinear antenna (Fig. 4), essentially several cylindrical patterns radiating from interleaved coaxial cabling. Above approximately 200 m, beyond the near-field, these individual cylindrical patterns begin to interact constructively to form the radio wave front. The antenna is constructed so most of the energy is embodied within a five degree circular beam, or cone; although several side lobes are present as illustrated by the insert within Fig. 4. This wave front is not impeded until turbulence on the correct scale is encountered, as shown schematically in Fig. 4. Turbulence produces strong small-scale variability in three dimensions, carrying moisture and temperature discontinuities vertically (and horizontally) adjacent to other air parcels. Atmospheric turbulence is generated at scales of tens to hundreds of meters by wind shear and convection. These large scale eddies break up into smaller eddies, which break up into still smaller ones, and so on until the turbulent energy is dissipated at very small scales by viscous heating. This cascading of kinetic energy occurs partially within a wavenumber space (ranging from only a few centimeters to hundreds of meters) referred to as the "inertial sub-range". It is somewhere within this inertial sub-range where turbulent scales of the multiple of one-half the transmitted wavelength are encountered. When an electromagnetic wave front encounters these areas of variability, the wave front is refracted slightly and a small

amount of energy is scattered in all directions, as represented by the dotted wave fronts emanating from point 'AA' within turbulent layer 'A' in Fig. 4.1 Very high above the troposphere the density of air is such that it cannot support small scale turbulence, hence the first theoretical limitation on the profiler is a maximum altitude that can support turbulence on the scale of 37 cm--a height which varies but is estimated to be between 18-20 km for the West coast.

The degree of turbulence and the variations in refractivity index over short distances affect the energy backscattered (the power returned). The refractive index for the troposphere at UHF frequencies (Balsley and Cage, 1980) is

$$n = 1 + 77.6 \times 10^{-6} \frac{p}{T} + 3.73 \times 10^{-1} \frac{e}{T^2}, \quad (1)$$

where e is the partial pressure of water vapor in mb (humidity), p is the atmospheric pressure in mb, and T is the absolute temperature in K. A refractive index structure function $D_n(\vec{r})$ described by Gossard and Strauch (1983) is used to quantify these variations over short distances as

$$D_n(\vec{r}) = [\overline{n(\vec{x} + \vec{r}) - n(\vec{x})}]^2, \quad (2)$$

where \vec{x} and $\vec{x} + \vec{r}$ are the vectors originating at the profiler antenna and terminating at the centers of two air parcels (depicted as circles) separated by a distance and direction \vec{r} , represented in Fig. 5. Within the inertial sub-range of homogeneous, isotropic turbulence, Gossard and Strauch (1983) state that

$$D_n(\vec{r}) \propto r^{2/3}. \quad (3)$$

To make an equality, a standard parameter C_N^2 , or the "refractive index structure parameter", was conceived. C_N^2 is a constant of proportionality describing the refractive index differences between two parcels of air situated adjacent to one another; so now Eq. (3) becomes

$$D_n(\vec{r}) = C_N^2 r^{2/3}. \quad (4)$$

¹ There is evidence suggested by Doviak and Zmric (1984) and Waterman *et al.* (1985) that at certain wavelengths, the backscattered energy is not isotropic, but rather anisotropic. There is ongoing research to resolve this phenomenon.

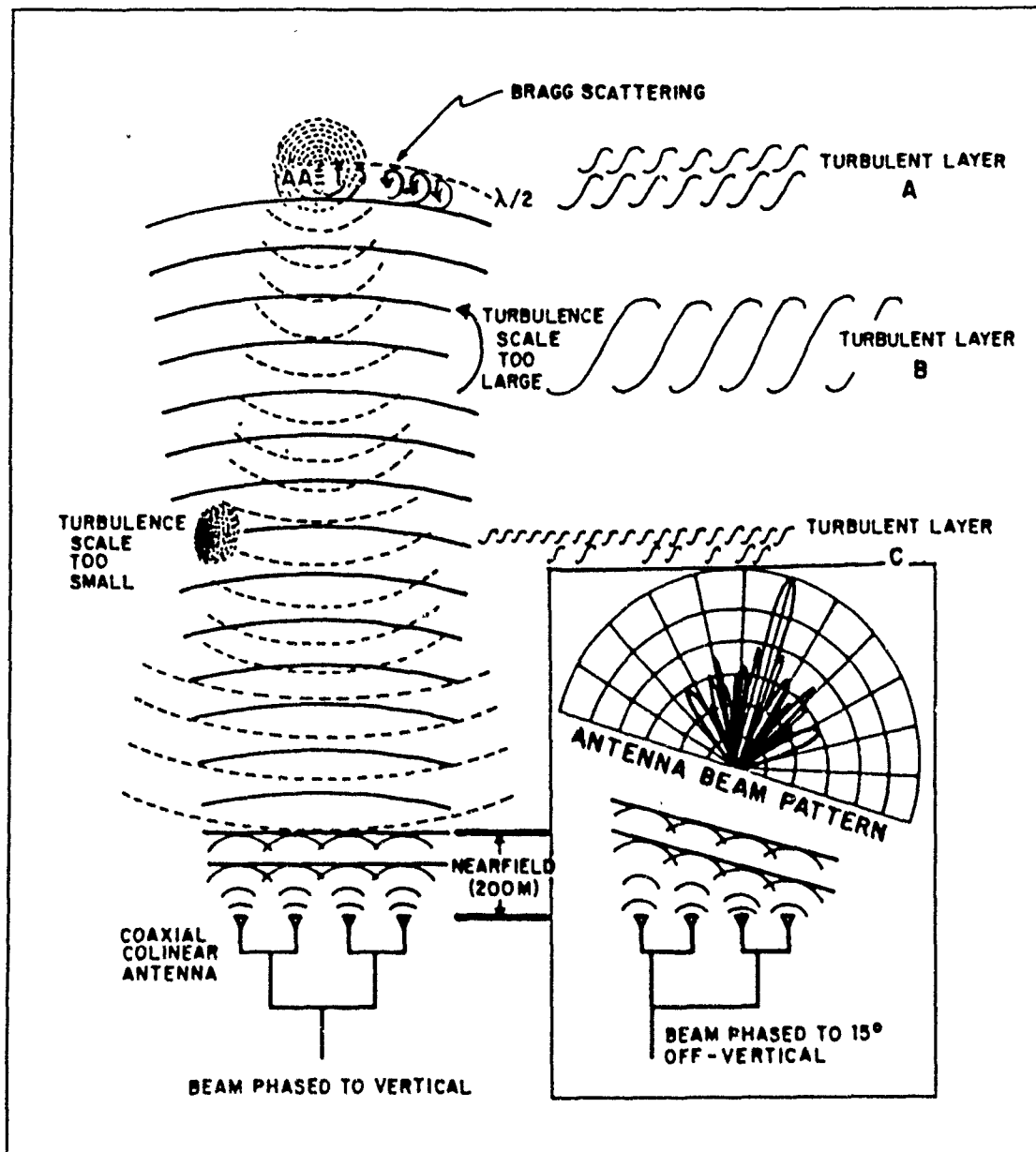


Fig. 4. Illustration of the Generation, Beam Pattern, and Scattering of Profiler Emitted Signals

C_N^2 is dependent on the temperature and humidity, as well as the pressure, as given by the relationship from Peterson (1988)

$$C_N^2 = 79 \times 10^{-6} \left[\frac{P}{T^2} \right] [C_T^2 + .113 C_{TQ} + 3.2 \times 10^{-5} C_Q], \quad (5)$$

B. PROFILER DATA PROCESSING

The wind speed and direction can be derived trigonometrically from the radial velocity of the profiler's individual transmitted beams, of which there are three--one vertical and two off-vertical. Figure 4 graphically depicts how these beams are formed; the off-vertical beams are phased by delaying the transmitted RF pulse to certain portions of the array. The radial velocity is derived from the Doppler frequency shift created by turbulent eddies traveling along with the mean wind. In the presence of turbulence or other velocity inhomogeneities (refractive index fluctuations) within the beam, the return signal spectrum may vary appreciably from one pulse to the next. In order to measure the prevailing flow velocity (by averaging out microscale fluctuations), many samples (about 1400) are composited over a period of integration (i.e., sample period). Even if there were no velocity variations within the beam, the returned signal would be at an assortment of frequencies, since the transmitted signal is not of uniform frequency. (In addition to the 404 MHz frequency, the transmitter also leaks low-intensity "tails" at slightly higher and lower frequencies. As the pulse length decreases the bandwidth increases.)

The period of integration is 58 seconds in the low mode and about 55 seconds in the high mode. The result at the end of the integration period is the most fundamental profiler quantity, a vertical profile of 36 wind velocity spectra. A representative example of the velocity-power spectra is given in Fig. 6. There are six modes of data: two off-vertical and one vertical mode for each the high power and low power configurations. In order to sample the entire troposphere and lower stratosphere, low and high mode profiles are measured sequentially, requiring a total time of approximately six minutes. Thus, 10 sets of tropospheric winds can be obtained per hour.

To get data, a radio wavefront or RF pulse must first be transmitted. After the energy is radiated by the antenna system, an electronic circulator switch is thrown to reconnect the antenna to the receiving equipment. There are 100-150 microseconds between each pulse and it is during this interval that the receiver samples the returned signal at different "gates" or vertical range bands as illustrated at the top of Fig. 7. Then, for each gate, several thousand samples are gathered and time domain averaged by the processor, as shown in the second and third functional steps in Fig. 7. Time domain averaging (TDA) consists of taking the mean of several consecutive samples in time. Figure 8 functionally illustrates how the received energy is broken into quadrature and in-phase components, and the subsequent time-averaging of each component. This time domain averaging is applied to the power spectra of the 36 available

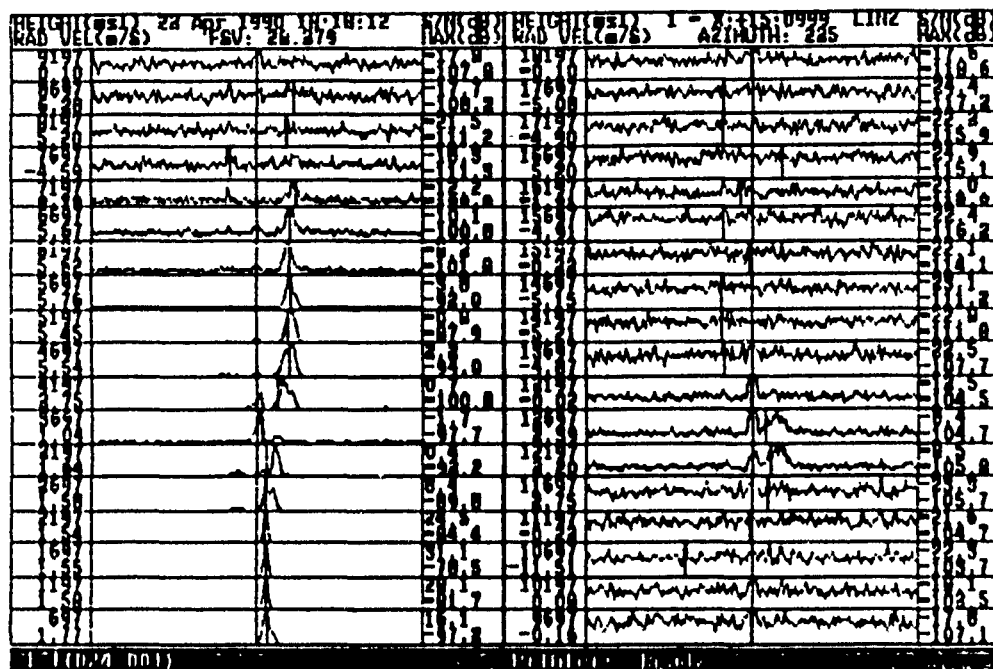


Fig. 6. Typical Vertical Profile of 36 Range Gate Frequency-Power Spectra: (As displayed on the Keyboard Display Unit (KDU).) In the upper-left hand corner of each gate is the center height of the sampled volume in meters. Beneath the height parameter is the resolved radial velocity in $m.s^{-1}$, also indicated by the vertical bar centered within the dominant peak. In the upper-right of each spectrum is listed the signal-to-noise and below this parameter is the maximum power encountered within the spectrum, both in dB.

gates, hence a TDA matrix can be formed as illustrated in Fig. 8, which consists of 256 samples in each of the 36 gates--256 samples are needed for the fast fourier transform (FFT) calculations later. The entire time the processor takes to collect a full matrix for all range gates is approximately three seconds in the low mode.

To this point in the data processing, a typical power spectrum in relation to time is available for each gate. But what is desired is the dominant frequency, therefore frequency domain averaging or spectral averaging subsequently ensues. It consists of calculating a mean spectrum from several consecutive spectra after the FFT computations

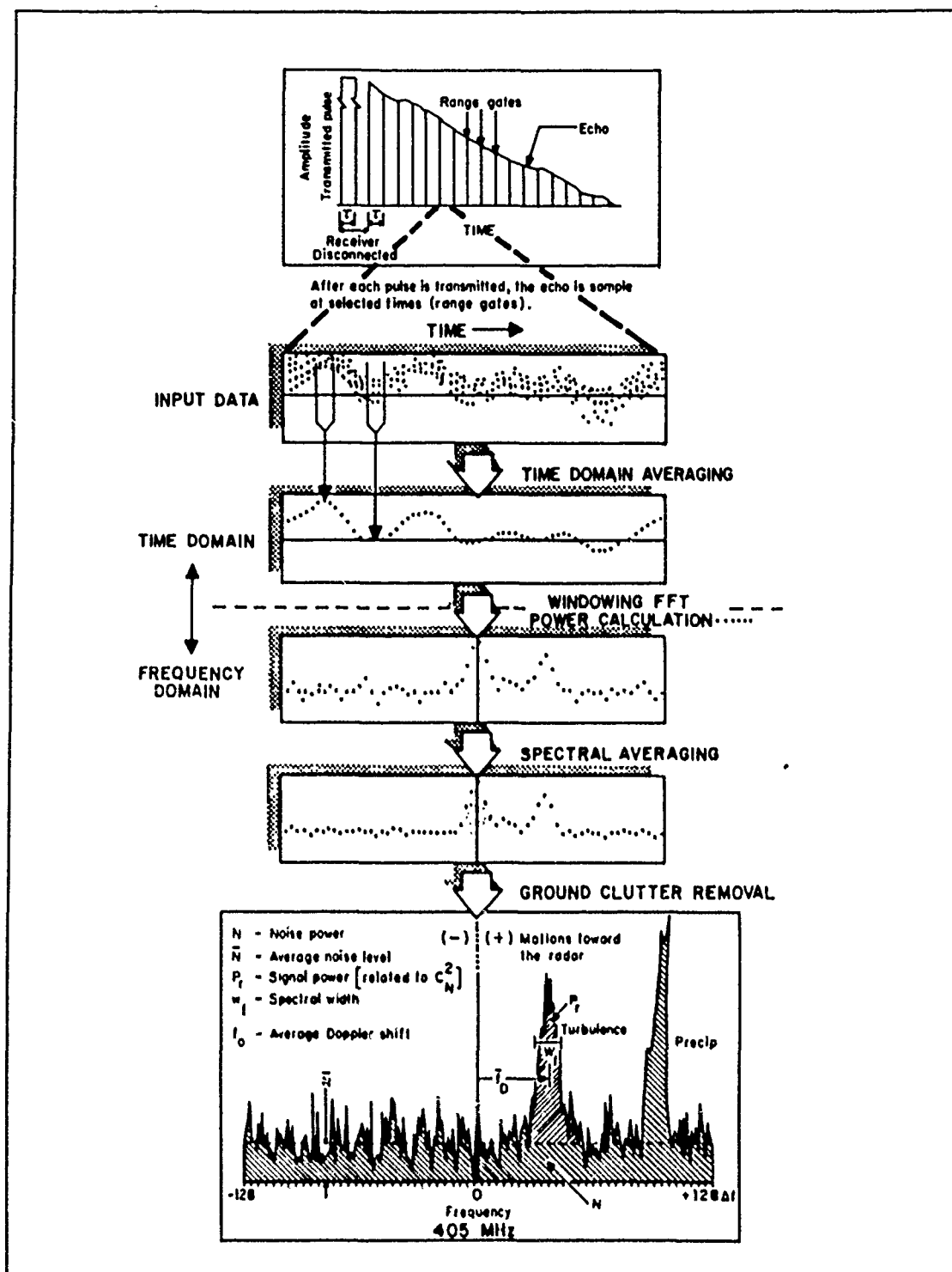


Fig. 7. Schematic Diagram of the Primary Signal Processing Steps for the Profiler

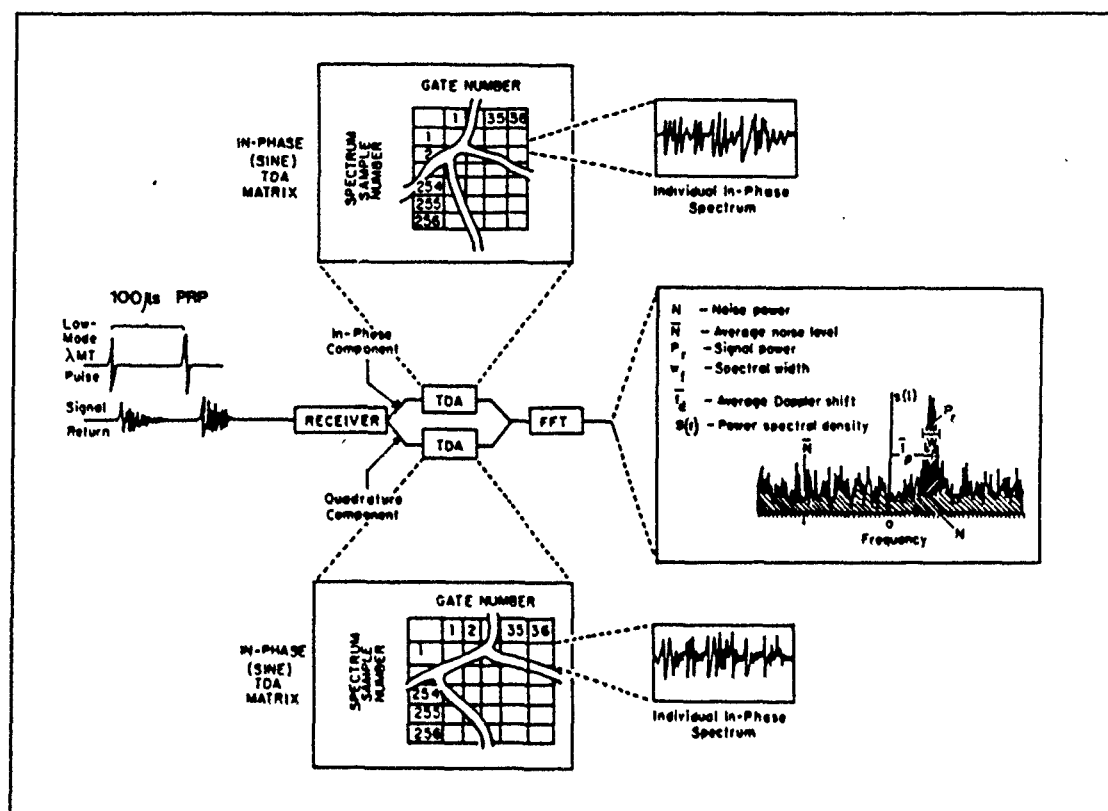


Fig. 8. Functional Diagram of the Time Domain Averaging (TDA) Process

have been performed. Now the time required to complete a spectrum in each of the six modes can be determined:

$$Time_per_spectrum = PRP \times TDA \times 256,$$

where PRP is the pulse repetition period of the radar and TDA is the number of time domain averaging matrices. Finally, the number of spectra utilized in the averaging process of each mode is adjusted, so the total time per spectrum is approximately 60 seconds, and, consequently, the total time per profile is then six minutes, which matches the National Oceanic and Atmospheric Administration reporting requirements for their future profiling network. The number of spectra utilized for a single profile during the first month of operation is listed in Table 1.

At this point, a typical power spectra in the frequency domain has been processed for each mode at each gate from which wind velocities must be determined. Briefly, a wind profiler is a Doppler radar that measures the shift in frequency created by moving targets. In the case of the wind profiler, the targets are turbulent eddies moving with the

Table 1. PROFILER PARAMETERS

Mode	High	Low
No. of TDA Matrices	40	120
PRP	162 μ s	100 μ s
Time per Spectrum	1.65s	3.072s
No. of Spectra	34	19

mean wind. Thus by determining the Doppler shift of the spectral moments, the wind toward and away from the radar can be determined. To accomplish this, a manufacturer's-supplied algorithm computes the Doppler spectral moments of the spectral peak associated with a local maximum in the frequency spectrum. Inputs to this algorithm are the velocity (or frequency) versus power spectrum (with noise and ground clutter removed) and the index of the local maximum determined to be signal. Outputs of this algorithm are the three spectral moments:

- 1) Signal Power (estimated total power of the received signal),
- 2) Mean radial velocity (first moment of the spectral peak), and
- 3) Radial velocity variance (second initial moment, or width, of the spectral peak).

This routine is specified for each mode and for each gate. The Doppler shift of the peak (f_D) can be converted into a radial velocity component of the wind, by re-arranging the following basic equation from Battan (1979):

$$f_D = \frac{-2V_r}{\lambda}.$$

The central frequency (as shown in Fig. 7) corresponds to the transmitted frequency. If a "target" is moving toward the radar, the frequencies will be increased; conversely, if it is moving away, the frequency will decrease. The Doppler return and the width of the peak at each range gate are measures of the degree of turbulence in the sample volume. The second peak within the sample spectra shown in Fig. 7 is an indication of detected precipitation. (Precipitation would be verified by on-site observations.)

Radial velocity components are next decomposed into easterly and northerly components of the Cartesian coordinate system. This is accomplished by the vertical and two off-vertical beams. The vertical beam pattern measures the actual w-component of the wind. With the w-component known, the u- and v-components can then be derived by trigonometry, as shown in Appendix C. Within Appendix C, θ_1 and θ_2 (the angles of the offset beams) are most commonly set at 15° from vertical and ϕ (the angle in the horizontal plane between the two off-vertical beams) is set at 90° for ease of trigonometric calculations.

Finally, the three moments are consensus-averaged, based upon data collected for a one-hour averaging period. The consensus technique is detailed in Appendix D. As suggested by the name, not all the data are averaged, rather only those that mutually agree within a threshold. A 2 m s^{-1} window, or threshold, is used by the manufacturer for the radial velocities. If the consensus group does not have at least four members, then the average value is reported as missing. This subset is then used to calculate the average values of all three moments.

C. PROCESSING OF RAWINSONDE DATA

The rawinsonde signal is sampled by the ground system every ten seconds. The wind data from 24 consecutive ten-second samples are then averaged--this provides smoothing of the initial data to remove noise (see Fig. 9). Consequently, all sharp features are effectively removed. A running average is subsequently maintained with data output every 40 m, based on a four m s^{-1} balloon ascent rate. A detailed presentation of the scheme for deriving rawinsonde data cannot be given within this study because the material is proprietary with Vaisala Corporation. (Winds in the lowest 200 m are handled in a quite different fashion, due to the obvious lack of data required for a running average; this different technique is proprietary information but is not important for this study since there are no profiler wind values at these levels.)

The rawinsonde data then represent approximately a 1000 m (actually 960m) thick volume (with 40 m gate spacing between subsequent data), whereas the wind profiler has 250 m resolution, or interval spacing, in the low mode (with 250 m gate spacing) and 1000 m resolution in the high mode (with 500 m gate spacing), hence different values as illustrated in Fig. 9. Therefore, a typical height of rawinsonde measurements centered within the sampling profiler gate was required for comparison. U and V-velocity rawinsonde components were subsequently averaged through a column centered around

the desired profiler gate height. Likewise, rawinsonde temperature and humidity were linearly averaged with respect to height around the profiler gate heights.

D. KNOWN SOURCES OF PROFILER ERROR

There are many potential sources of noise in the profiler radial velocities. Of most significance for this comparison study, the profiler and rawinsonde sample at different locations. The wind profiler provides simultaneous measurements over all heights at a fixed location. It samples large volumes of atmosphere (up to 1 km deep) and assigns an integrated value to the center height of the sampled column. The rawinsonde, on the other hand, records measurements at different, discrete heights and at different times (a typical ascent will take up to 1-1/2 hours and may cover many kilometers laterally). As a result, the rawinsonde and the wind profiler often obtain measurements at widely separated locations where the winds may be different. Also, the winds over the fixed profiler location are not uniform during the rawinsonde's 1-1/2 hour ascent; therefore, variability of the atmosphere can make the interpretation of any comparisons difficult at times. Furthermore, since these instruments sample in a functionally different manner, comparisons of their measurements cannot provide unambiguous information on the accuracy of either instrument.

Another large source of error is electromagnetic noise present within the pulse volume as a result of nearby power lines or machinery, as well as other contributions from side lobes (power "leaking" from the antenna at angles other than the desired angle). The Federal Aviation Administration began operating a traffic control radar within 60 m of the Ft Ord wind profiler site in April of 1990. Although the operating frequency does not appear to affect profiler operations, the movement of the antenna provides a strong enough Doppler shift of the profiler transmitted frequency to provide a significant return in the side lobes of the receiver antenna and contaminate the lowest gate. There appear to be many forms of this contamination such as the inclusion of a sinusoidal wave pattern in the lowest four gates as represented in Fig. 10. A more common contamination pattern is the occurrence of narrow peaks at approximately 7 m s^{-1} (not shown).

Noisy wind vectors can result from an imbalance of the individual beam sensitivities, since one beam may detect the weak atmospheric turbulent signal while the other may intermittently resolve the background noise as the dominant signal source. In the event that the atmosphere is quite dry and the associated profiler backscatter weak, there is a fairly strong persistent background noise frequently present and the "insensitive" beam

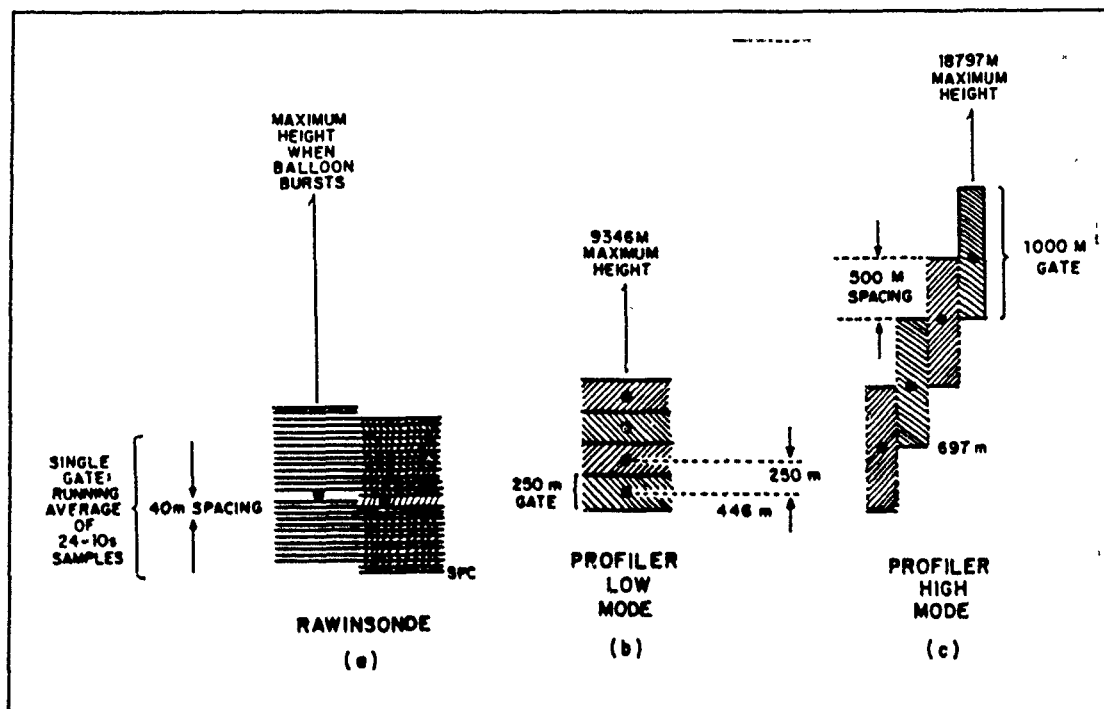


Fig. 9. Functional Rawinsonde and Profiler Gate Spacing

may "lock in on" the background frequency. The result is a high consensus number but an unrealistic wind.

Closely related to this latter error is the susceptibility of each beam to be less sensitive to cross-winds, or those prevailing winds which cross perpendicular to the direction which the beam is formed. Hence, the accuracy of determining these cross-wind velocities is reduced. There is consistent evidence of this bias throughout the course of this study, and analysis of a larger data set would probably define the bias discreetly.

When the radar switches from transmit to receive mode, there is electronic noise in the system that takes a few microseconds to dissipate. Any signals returned by the atmosphere during this brief period are masked by noise. Because the first signals to return come from low in the atmosphere, the lowest sampling gate (446 m) is most susceptible to this problem. No evidence of this effect was discovered through the course of this study.

The profiler operating frequency and sampling interval determine the Nyquist velocity, the maximum radial velocity that can be measured. The well-known Nyquist sampling theorem states that the highest frequency to be resolved in the signal must be sampled at least two times per period. If the signal contains energy at frequencies higher

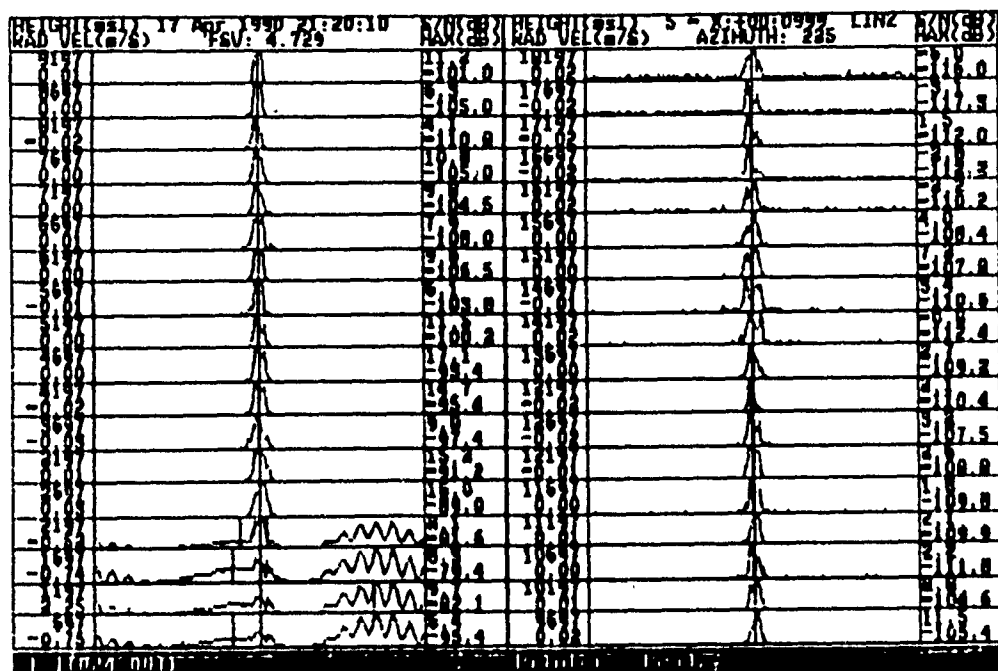


Fig. 10. Sample of FAA Traffic Control Radar Contamination of NPS Profiler: Evident in the four lowest gates. (See Fig. 6 for format description.)

than the Nyquist frequency, the Doppler signal can be aliased by higher frequencies. This means that the energy is "folded back" to frequencies less than the Nyquist frequency (McGillen and Cooper, 1974). For the NPS profiler the Nyquist velocity is about 15 m s^{-1} (30 kt) in the low mode and 60 m s^{-1} (120 kts) in the high mode. Radial velocities greater than the Nyquist velocity are "folded" as illustrated in Fig. 11 at 11697 m. Although velocity folding occurred in two spectra within Fig. 11, fortunately it was not folded into the spectral region "sensitive" to the algorithm. There were no known occurrences of this type error during the study period.

Contributions from persistent vertical velocity, such as in the vicinity of sloping terrain or the closed cells of the land/sea breeze circulation, may cause appreciable contamination of the "horizontal" velocity measured by the off-zenith beams, especially when the horizontal wind speed is low. Since the "horizontal" beams are 15° from

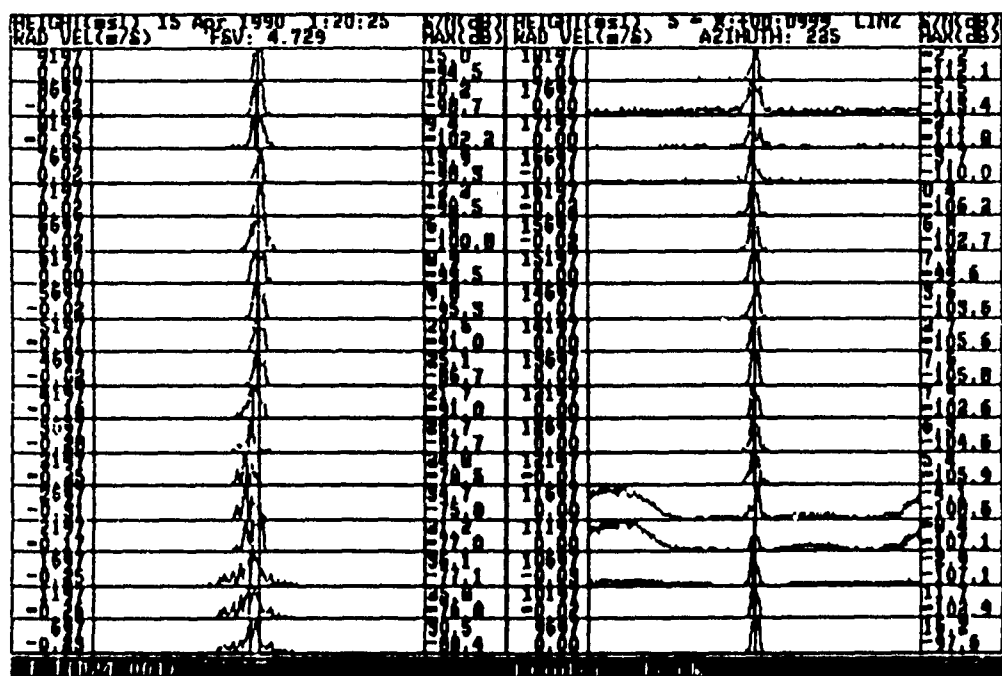


Fig. 11. Sample of Velocity Folding in the NPS Profiler: Seen at the 11697 m level. (See Fig. 6 for format description.)

zenith, 75 percent of the off-zenith radial velocity is sensed as vertical velocity. Thus the horizontal velocity required to produce a 1 m s^{-1} radial component is about 4 m s^{-1} . Synoptic-scale vertical velocities ($\sim 0.1 \text{ m s}^{-1}$) appear not to pose a problem, but smaller-scale systems which may contain vertical velocities as great as several meters per second are clearly a potential source of horizontal beam contamination.

Turbulence accompanied by significant backscatter above a height which the profiler can "see" introduces aliasing into the data. The maximum unambiguous radar height is given by Battan (1974) as

$$R_{\max} = \frac{c(\text{PRP})}{2};$$

where c is the propagation speed of radio energy. PRP as set in the low mode of the NPS profiler is $100 \mu\text{s}$, which sets R_{\max} in the low mode at 15,000 m. (R_{\max} in the high mode is 24,300 m.) Therefore, if the transmitted signal is returned from a source higher than 15,000 m, the radar processor while in the low mode will see this signal as a possible

early return in the lower gates of the next sampled pulse. Consequently, ionospheric and cosmic noise can also be problems. In this case the radar will receive noise in any of the gates, when realistically the signal evolves quite a bit higher beyond that which the radar can measure.

Precipitation and other hydrometeors can also scatter energy back towards the antenna. Typical meteorological radars operate at wavelengths on the order of 5 to 10 cm, whereas wind profilers operate typically near wavelengths of 74 cm. Hydrometeors are some 10^4 times less reflective to wind profilers compared to conventional weather radars. This is indicated by the reflectivity equation given by Gossard and Strauch (1983) for single particle scattering:

$$\eta = \frac{(const)d^6}{\lambda^4},$$

where d is the particle diameter. Precipitation, when detected, can be a problem in some circumstances. Clearly, if there is interest in the vertical motion of the air, precipitation presents a problem, as the vertical velocity measured is that of the precipitation, and not the air. In some cases, spectra from the vertical beam will show a double peak: one corresponding to the clear air and the other precipitation. This is illustrated in Fig. 12.

Rawinsonde operation colocated with the profiler creates a false wind velocity value. Figure 13 presents two spectra from the Keyboard Display Unit. Balloon interference is highlighted at approximately 6000 m in the top frame and 11000 m in the bottom frame. The time difference between these two frames is 25 minutes. Again, assuming a 4 m s^{-1} balloon ascent rate, this is precisely the height the rawinsonde should have attained. The detection of the balloon appears to be due to the different index of refraction value characteristic of the gas within the balloon vice the actual reflection from the non-metallic surface of the balloon. The radio signal of 402 MHz utilized by the rawinsonde for passing data to the ground system does not appear to interfere with profiler operation.

It must also be recognized that the vertical beam and the two off-zenith beams do not sample the same volume of air, in either space or time. There may be up to a 3.2 km difference at an altitude of 12 km. This is especially troublesome in the presence of small-scale mesoscale disturbances.

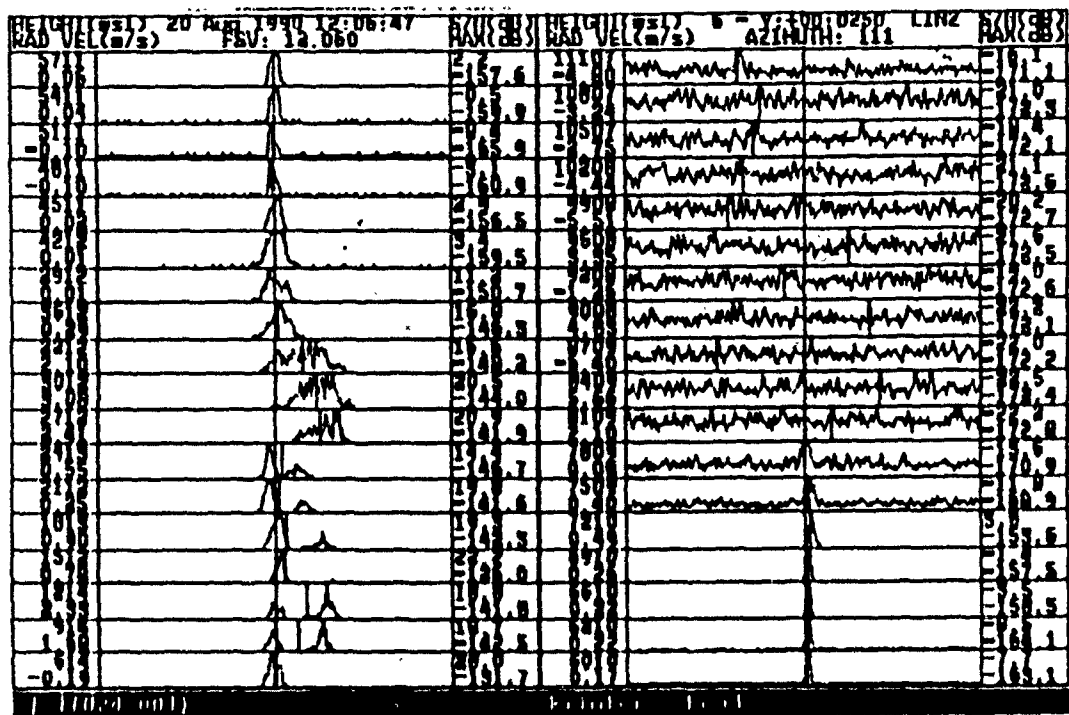


Fig. 12. Example of a Double Peak in NPS Profiler Spectra caused by Rain: Evident clearly at the 914 and 1214 m levels, as well as other disparities extending up to 4000 m. (See Fig. 6 for format description.)

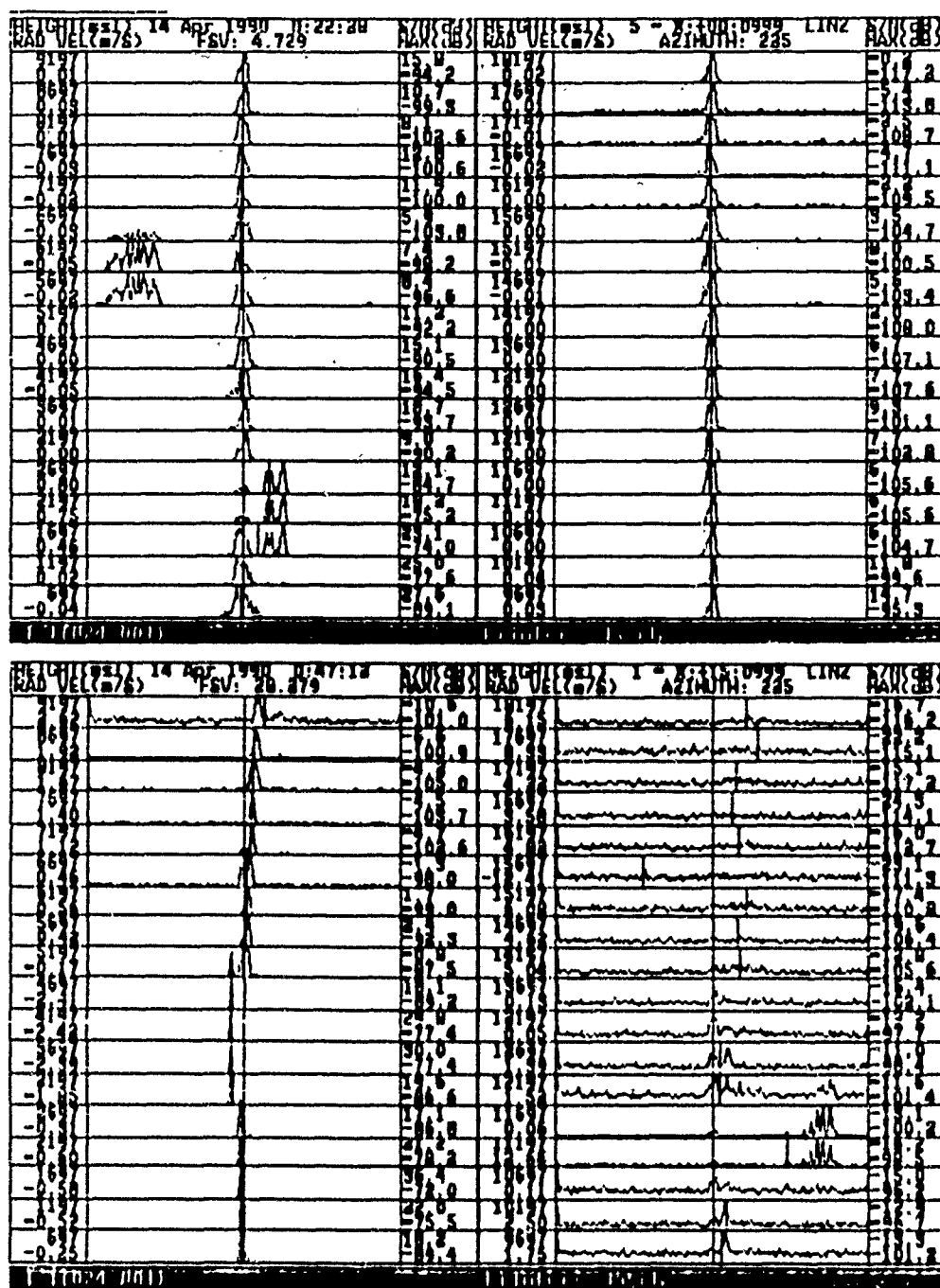


Fig. 13. Example of Rawinsonde Balloon Interference in the NPS Profiler: First evident in the top profile of spectra at 6197 m then in the lower profile of spectra at 11697 m.

III. DATA ANALYSIS

A. COMPARISON OF MANUFACTURER'S CONSENSUS TO RAWINSONDE DATA

Prior to analyzing dynamic, kinematic and thermodynamic relationships derived from the NPS profiler winds, it is necessary to first determine the accuracy of the profiler wind data. This information provides the NPS Marine Atmospheric Measurements Lab a benchmark of how the NPS profiler performs in relation to other profilers as well as verifying requirements within the profiler procurement contract. Both the wind profiler and rawinsonde system provide vertical profiles of wind measurements; therefore, like many previous studies, the accuracy of the profiler will be gaged by the rawinsonde data taken as truth data. A statistical comparison between profiler and rawinsonde wind data was made and used two approaches: (1) each horizontal wind component was correlated between the profiler and rawinsonde as determined by a correlation coefficient, and (2) mean and standard deviations for the difference in each horizontal wind component as measured by the two instruments was calculated. Because such a small rawinsonde data set was available during the first month of operation, a more detailed look into why potentially "bad" profiler data was not in agreement with the rawinsonde data was done manually, providing a third, more subjective approach.

Nine individual profiles are compared to assess the quality of the manufacturer's consensus winds measured by the profiler. Figure 14 is a representative comparison of the vertical profiles of wind speed and direction measurements for 20 April 1990 made by the two instruments. The associated complete rawinsonde sounding is presented in Fig. 15. Additional comparisons for the remaining eight soundings (Figs. E-1 through E-16) as well as the specific positions of the five at-sea rawinsonde launchings (Fig. E-17) are presented in Appendix E. In each case the rawinsonde profile is flanked by its associated Tycho hourly-consensus profiles, approximately 2 hours on either side of the rawinsonde launch time. Subjectively, the profiles correlate very well, at least where consensus in the radar data is achieved. The wind direction correlates very well. Below 5 km the wind speeds are generally within 5 kts of each other, while above 5 km the wind speeds are accurate to within 10-15 kts. The departure between individual profiler and rawinsonde wind barbs in the lowest 2000 m seen from the remaining launch times in

Appendix E could potentially be due to the discrepancy in instrument locations as well as the turbulence detected by the radar profiler in the presence of the marine inversion.

A comparison (rawinsonde vs profiler) of the individual horizontal wind components versus height are illustrated in Fig. 16 and 17 for a representative low mode profile from 0000 UTC 20 April 1990 and Fig. 18 and 19 for a typical high mode profile from 0700 UTC 03 May 1990. There is generally very good agreement below 5-6 km in the low mode and below 8-9 km in the high mode. There is a notable bias in the v-velocity component in the high mode, which appears to be due to the orientation of the prevailing winds in relation to the profiler antenna, which in this case were from the north.

In the low mode the maximum height obtained appears to correlate with the fall-off in humidity (evident in Fig. 15 where the atmosphere becomes dry above 4000 m); but is never greater than approximately 8 km even when humid layers are present aloft. This is due to the weakened signal from geometric spreading. (A humid layer aloft is defined in this paper as a layer with greater than 40% relative humidity above 4000 m.) This limitation is expected since a .74 cm radio signal is four times more sensitive to humidity fluctuations associated with turbulence than to temperature fluctuations, at least in the lower atmosphere (Cage 1990). This is illustrated in Fig. 20, by a deep humid layer which exists to 5 km. This is reflected in both the U and V-velocity component winds in Fig. 18 and Fig. 19.

As additional proof of the dominance of humidity in the lower atmosphere, a nearby sounding was compared with the raw spectra. Fig. 20 is the 1200 UTC 06 April 1990 Oakland sounding, 10 hours prior to the low-power mode profiler spectra in Fig. 21 (0000 UTC 07 April 1990 was not available). Typical conditions for this period of study, as seen in Fig. 21, are first a layer of very strong returns between 500-1400 m, the marine thermal inversion; which is followed by a rapid fall-off of signal return, until approximately 3000 m is reached where the signal levels begin to increase due to humidity. This corresponds very well with the moisture layers in the sounding. This is then followed by a fall-off between 4000-5000 m and a local maximum of -2 dB S/N reached at 5000-5500 m. In summary, a very good subjective correlation between the rawinsonde sounding and profiler spectra is evident.

The maximum height attained in the high mode is about 12 km (significantly less than the theoretical 24 km which the electronics allow), again due to weakened signal return from geometrical spreading. But, what is additionally seen in the U and V components is a 2-3 km gap in consensus data just below the tropopause (see Fig. 18 and Fig. 19). The tropopause is identified by a constant temperature profile seen in the

rawinsonde data. It appears at this time, that this gap is centered around the maximum of the "jet stream", or jet stream core if overhead. This is the most consistent feature seen in the data above 8 km. Apparently, the wind shear throughout this region is minimal, thus, reduced turbulence in a relatively dry region provides little signal return. However, above the jet maximum, winds begin to decrease and radar returns are detectable above noise. This too is seen in the raw spectra in Fig. 22, where signal strength falls off and then increases above -10 dB at the 12197 m level.

To quantify the data accuracy, a statistical comparison was made by computing the correlation coefficient, calculating the standard deviation, and graphically portraying the data "pairs" on scatter plots. The comparisons were based on unedited consensus data from the manufacturer's algorithm. Figures 23 and 24 are scatter plots of component rawinsonde measurements versus wind profiler measurements for the nine combined launchings. Each marker corresponds to a measurement made at about the same hour and height for both instruments. If the two measurements are equal, then the marker will lie on the diagonal. If the marker is positioned off this diagonal the two measurements are different. Consistent markers to one side or the other indicate a bias.

In the low mode, the density of data around the scatter plot diagonal appears good below $7-8 \text{ m s}^{-1}$ (15-17kts). Winds above this value are generally associated with higher heights; and as Fig. 23b illustrates, the "bad" values (the values that do not fall closely along the diagonal) generally lie above 6 km as represented by the markers \diamond and Δ . Similarly, in the high mode data depicted in Fig. 24b there appears to be an appreciable density of data along the diagonal, with any "bad" data related to speeds of 8 m s^{-1} (17kts) above 8 km. The depiction of "good" data at higher speeds indicate that height is the primary contributor to the presence of "bad" data. There is a bias tendency in v-velocity components which is more noticeable in the low mode data. This cannot be explained but may be due to such a small data set, or due to the orientation of the prevailing winds relative to the profiler fixed beams.

Table 2 presents the statistical results broken out by atmospheric layers. The values listed under the column "Mean", represent the mean error away from the mean wind component, while "Standard Deviation", is that value taken around the mean wind component, within one standard deviation or 67% of the data. The "Correlation Coefficient" values were calculated by the Pearson correlation coefficient relating profiler to rawinsonde data. The guidelines this study has set for "good" data is a correlation coefficient above .93 and a standard deviation less than 2.5 m s^{-1} , which are taken from the findings by Weber and Wuertz (1990). However, the performance of the radar in

relation to the rawinsonde system never quite met these criteria. The table reveals good correlation in the low mode below 6 km in both components. Good correlation in the high mode is seen below 8 km. There is poor correlation in the lowest 2-3 km under the presence of the inversion layer, i.e., there is turbulence created by the wind shear, the inversion jet, and/or convective thermal cells. The statistical results appear to reinforce the conclusions made earlier by the subjective analysis.

An accuracy determination would not be complete without the inclusion of the site survey, which establishes exactly where the antenna is oriented. For consideration, the elevation accuracy of the antenna base height is ± 1 m, while the azimuthal accuracy is $\pm 3'$ of arc. The results and the survey site layout are presented in Appendix F. The accuracy to which the profiler array was established is considered negligible for this study, but is presented for completeness and for the record to accommodate future studies.

The NPS wind profiler appears from the statistical analysis to be accurate to within only $3\text{--}4\text{ m s}^{-1}$ in the lower atmosphere (or more specifically within the moist layer below 6 km). This error is slightly greater than the 2.5 m s^{-1} standard deviation computed by Weber and Wuertz (1990). The profiler error is significantly greater than the 1 m s^{-1} accuracy specification listed in the procurement contract. Meanwhile, Strauch *et al.* (1987) found a standard deviation of about 1.3 m s^{-1} in clear air and Wuertz *et al.* (1988) found a standard deviation of about $2\text{--}4\text{ m s}^{-1}$ in precipitation. Thomson and Williams (1990) reported amazing accuracies in profiler data of $\pm 1\text{ m s}^{-1}$. The studies by Weber and Wuertz, as well as the other studies presented, analyzed several thousand pairs of rawinsonde and profiler data, while this study only was able to look at a few hundred. A larger data set would be expected to reveal a lower standard deviation based on the small mean error values listed in Table 2, for heights below 6 km.

Sonde High Mode Comparison Data: 90 04 19 at 23 23 GMT

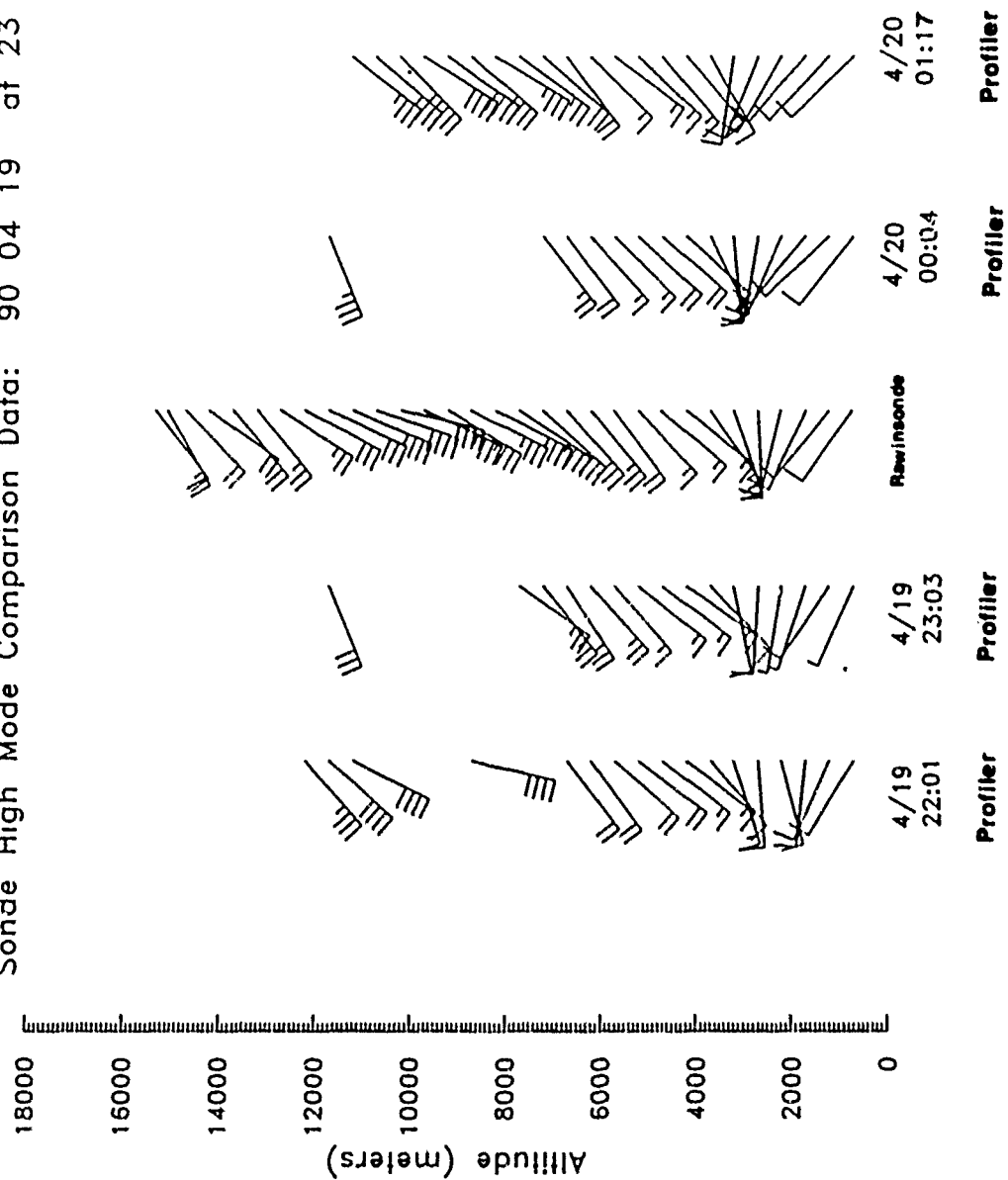


Fig. 14. Profiler-Rawinsonde Comparison Winds for 0100 UTC 20 April 1990

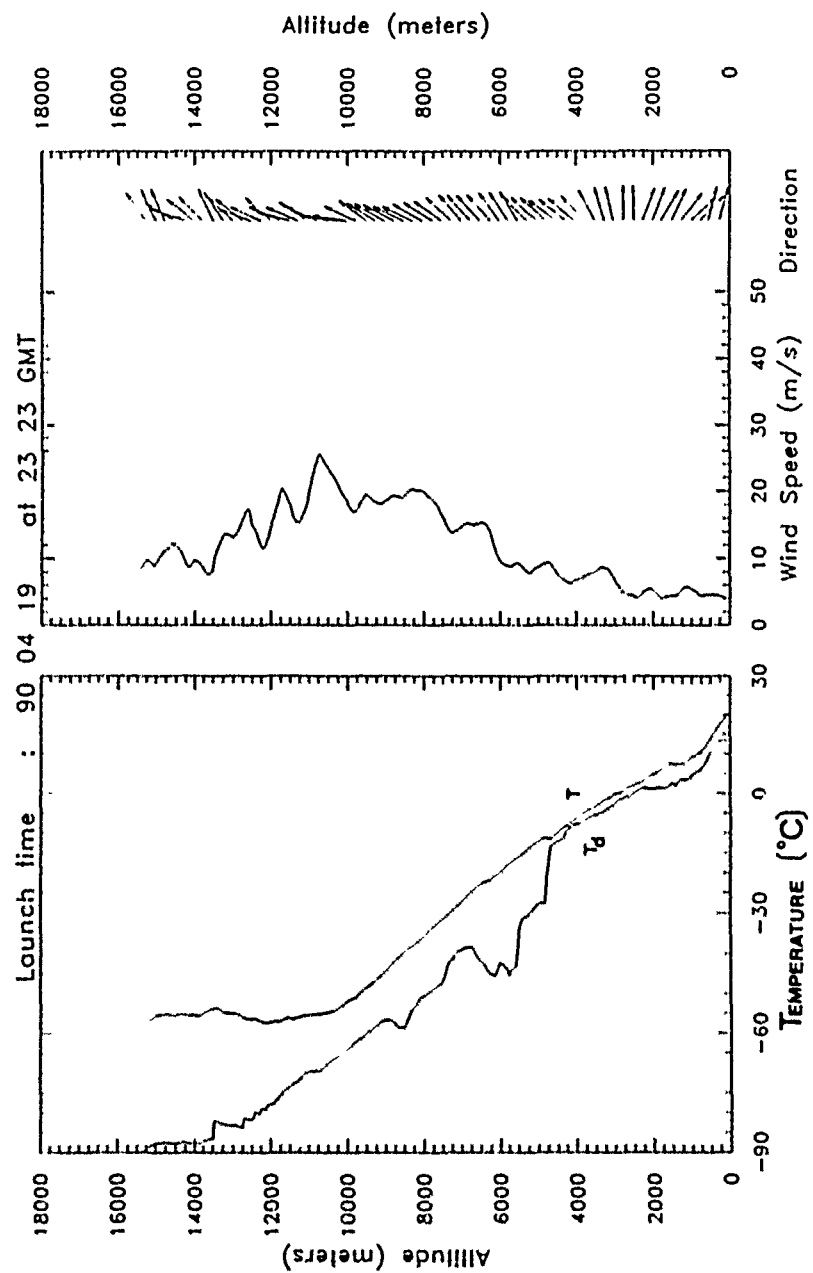


Fig. 15. Rawinsonde Sounding for 0100 UTC 20 April 1990

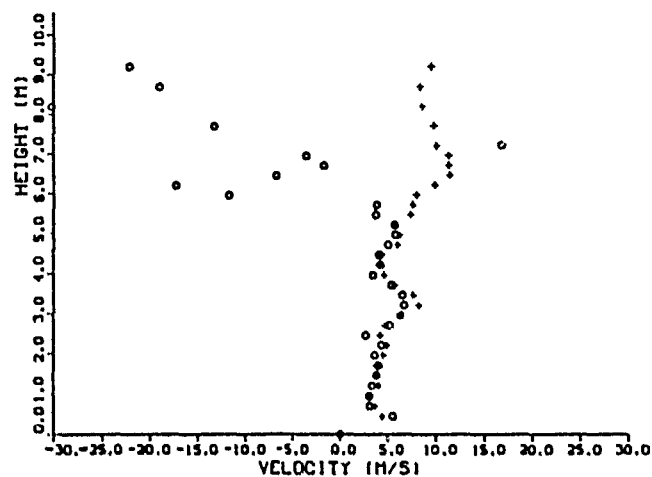


Fig. 16. Typical Comparison Plot of Rawinsonde vs Profiler U-Velocity Component (Profiler in Low-Mode): Rawinsonde winds are indicated by the \circ marker, while the profiler-derived winds are indicated by the $+$ marker.

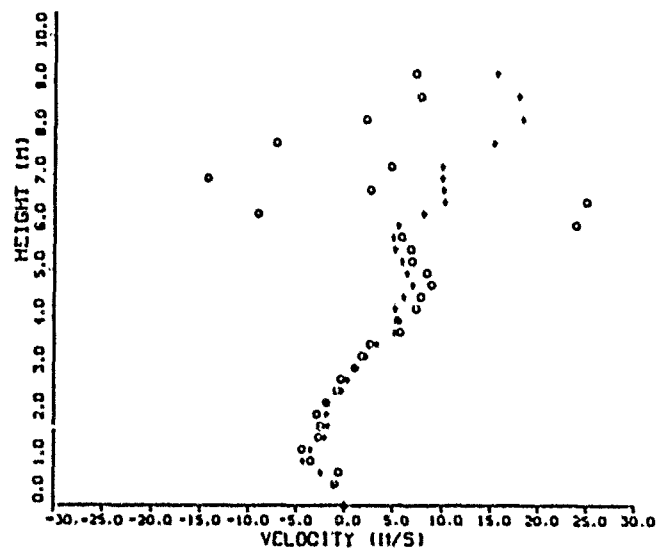


Fig. 17. Typical Comparison Plot of Rawinsonde vs Profiler V-Velocity Component (Profiler in Low-Mode): Rawinsonde winds are indicated by the \circ marker, while the profiler-derived winds are indicated by the $+$ marker.

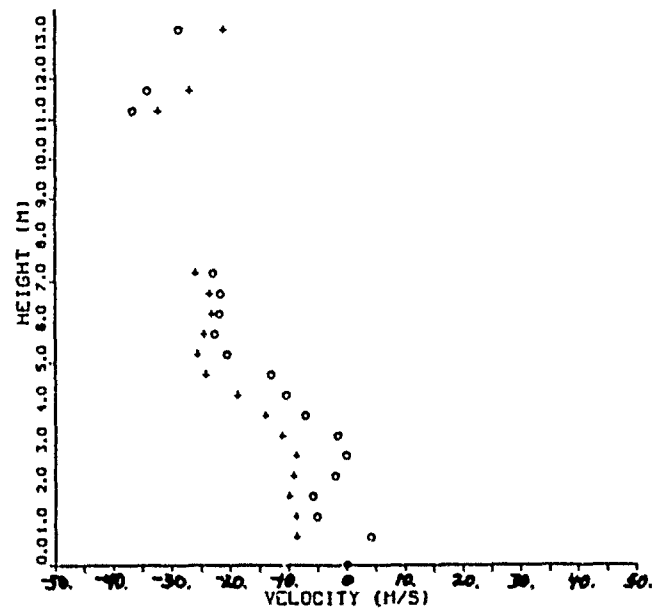


Fig. 18. Typical Comparison Plot of Rawinsonde vs Profiler U-Velocity Component (Profiler in High-Mode): Rawinsonde winds are indicated by the o marker, while the profiler-derived winds are indicated by the + marker.

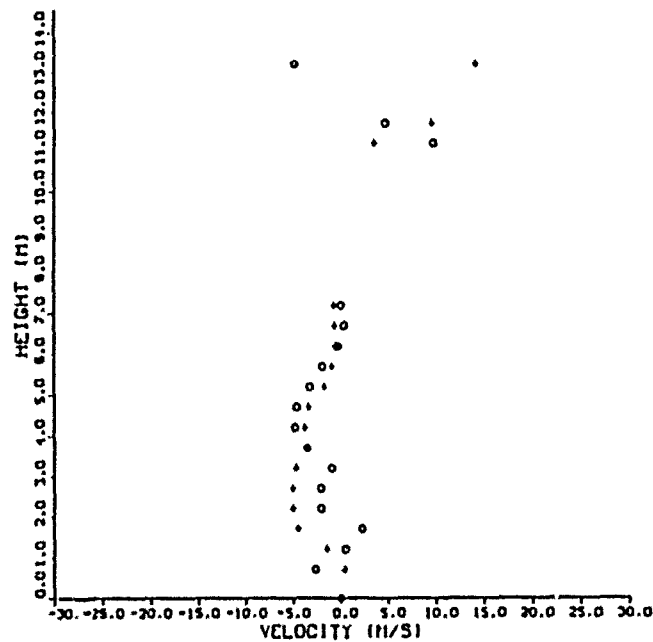


Fig. 19. Typical Comparison Plot of Rawinsonde vs Profiler V-Velocity Component (Profiler in High-Mode): Rawinsonde winds are indicated by the o marker, while the profiler-derived winds are indicated by the + marker.

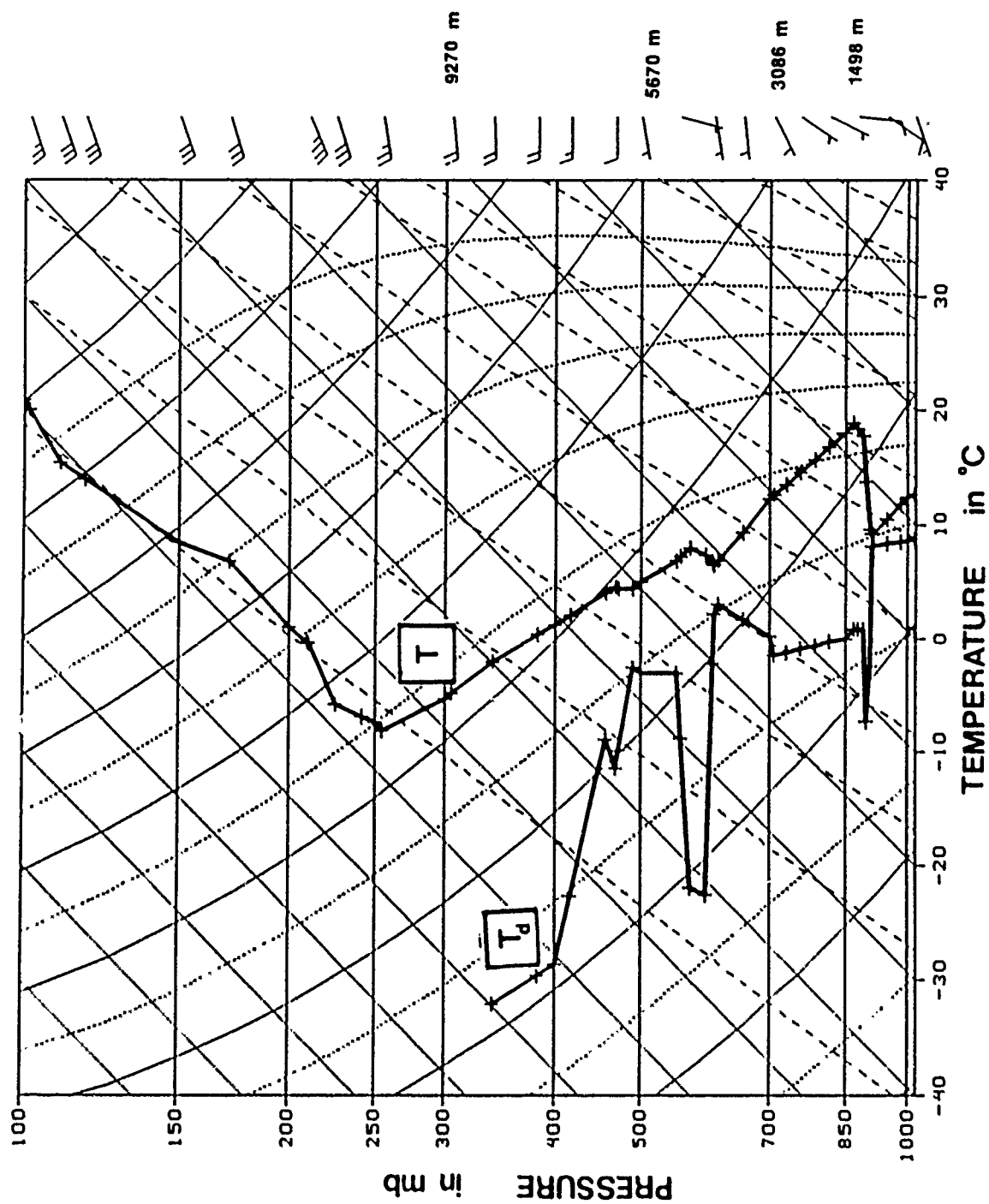


Fig. 20. Oakland (72493) Sounding for 1200 UTC 06 April 1990

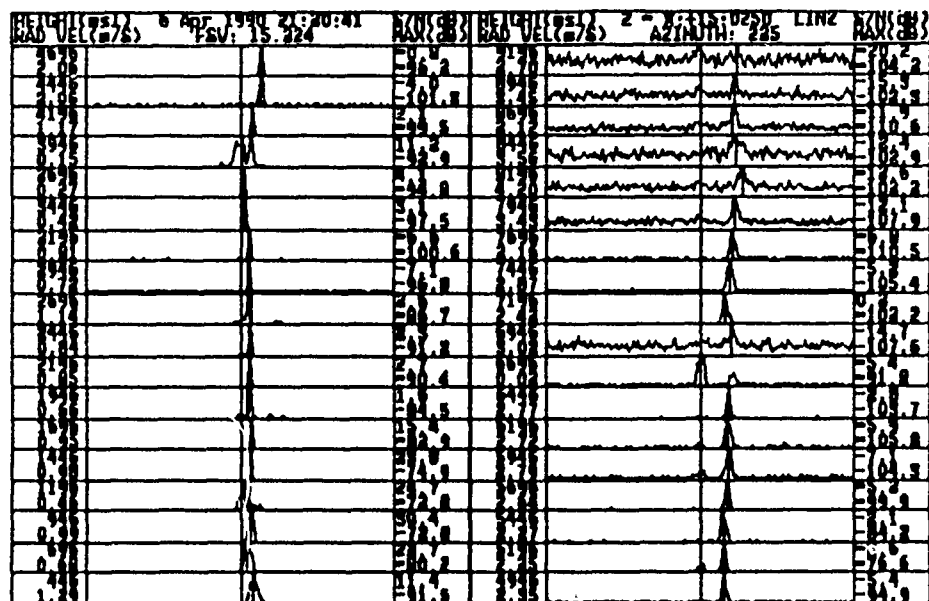


Fig. 21. Example of Low Mode Spectra: There is increased signal strength in the 5196 and 5446 m levels due to humidity.

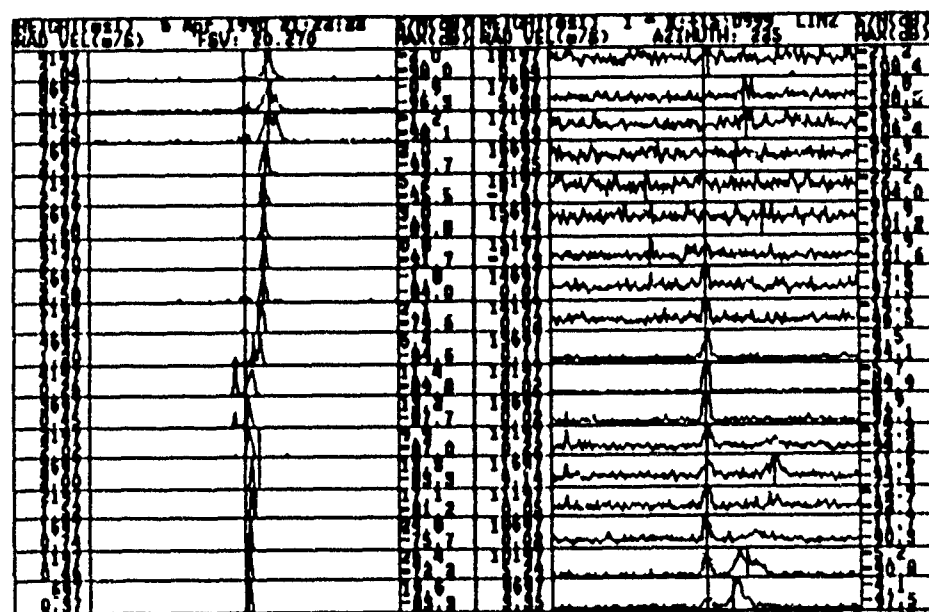


Fig. 22. Sample Low Mode Spectra Depicting Jet Stream Structure: Evident is an increase of signal strength at the 12197 m level.

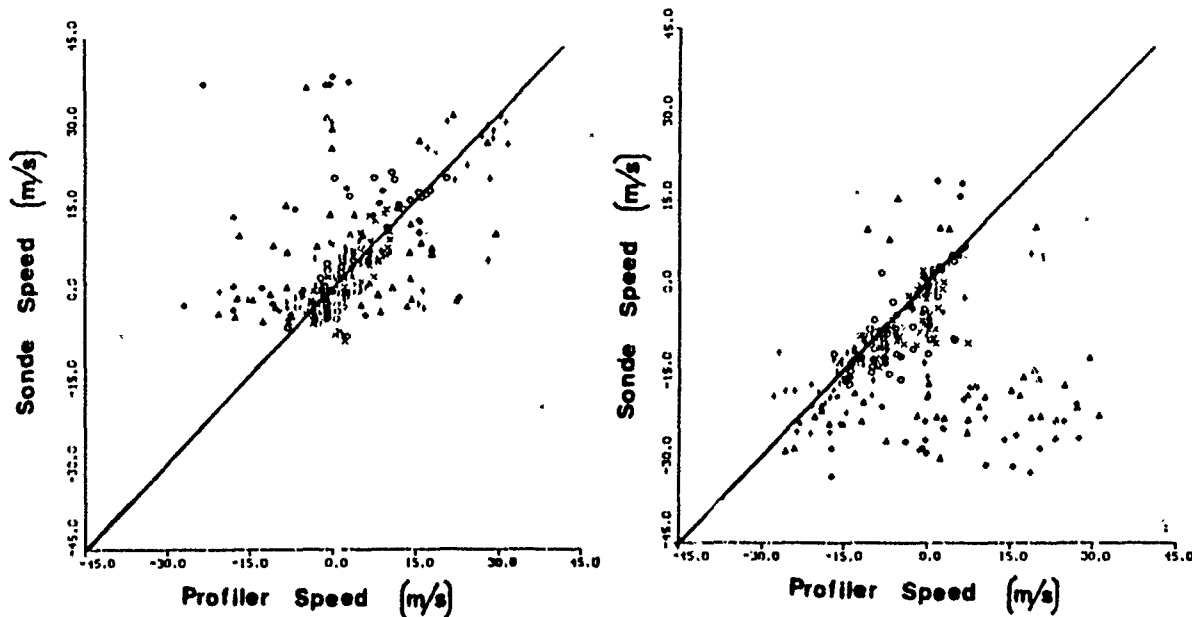


Fig. 23. Scatter Plot of Low-Mode Profiler vs Rawinsonde Velocity: Data taken from all nine rawinsonde launches. The marker \times represents those winds derived below 2 km, \circ from 2 to 4 km, $+$ from 4 to 6 km, Δ from 6 to 8 km, and \diamond any winds above 8 km.

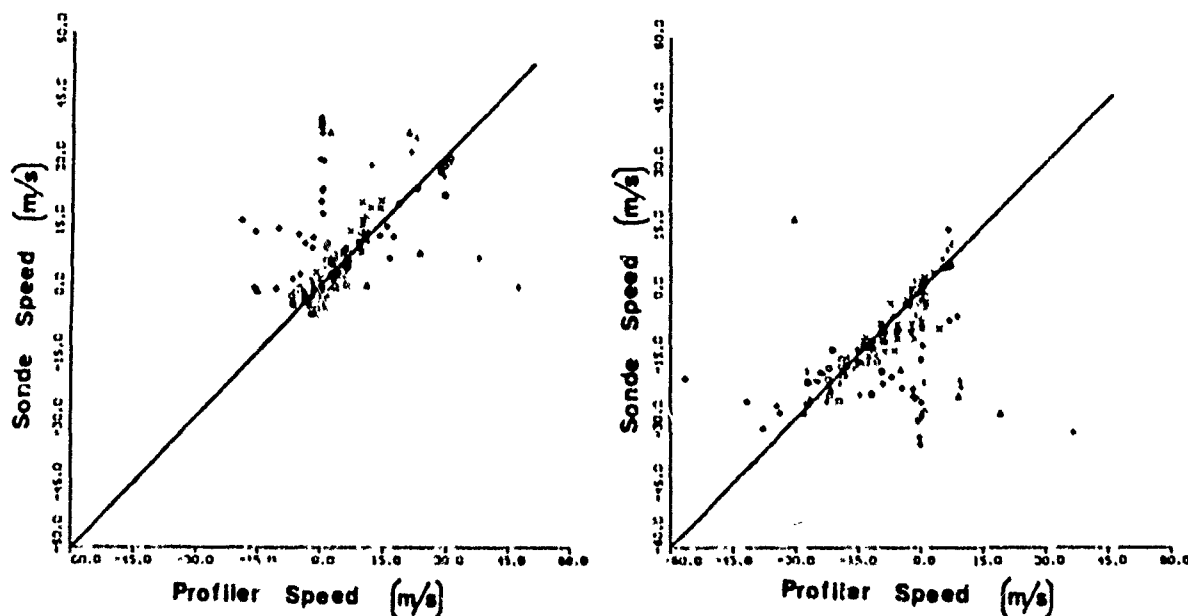


Fig. 24. Scatter Plot of High-Mode Profiler vs Rawinsonde Velocity: Data taken from all nine rawinsonde launches. The marker \times represents those winds derived below 4 km, \circ from 4 to 6 km, $+$ from 6 to 8 km, Δ from 8 to 10 km, and \diamond any winds above 10 km.

Table 2. STATISTICAL ANALYSIS OF DIFFERENCES BETWEEN RAWINSONDE AND PROFILER-DERIVED VELOCITIES FOR ALL NINE RAWINSONDE LAUNCHES

Mode	Component	Layer	Mean Error	Standard Deviation	Correlation Coefficient
Low	U Velocity	All Heights Combined	2.49	10.31	.490
		< 2 km	0.083	3.4	.791
		2-4 km	-.828	4.66	.815
		4-6 km	-.899	8.4	.783
		< 6 km	-.553	5.78	.793
		6-8 km	-4.59	14.09	.285
		> 8 km	-13.0	18.68	.077
Low	V Velocity	All Heights Combined	7.54	14.31	.415
		< 2 km	2.06	4.04	.634
		2-4 km	1.67	4.31	.757
		4-6 km	3.10	8.01	.714
		< 6 km	2.22	5.65	.740
		6-8 km	18.98	19.25	0.01
		> 8 km	26.0	20.34	-.048
High	U Velocity	All Heights Combined	-4.94	12.05	.439
		< 4 km	-.996	3.275	.912
		4-6 km	-1.04	3.091	.970
		6-8 km	0.627	13.78	.516
		< 8 km	-.717	6.44	.805
		8-10 km	-15.36	21.43	.063
		> 10 km	-16.35	14.69	.647
High	V Velocity	All Heights Combined	4.88	12.83	.361
		< 4 km	1.985	3.817	.742
		4-6 km	0.547	3.916	.914
		6-8 km	4.29	10.77	.611
		< 8 km	1.99	5.79	.783
		8-10 km	16.88	29.61	-.609
		> 10 km	11.59	18.96	.217

B. INVESTIGATION OF VARIABLES AFFECTING DATA QUALITY

Given that there are numerous sources of error in the profiler operation that influence the six-minute profiles and hourly-consensus, it may be possible to eliminate bad six-minute data in order to subsequently improve overall performance. To assess the six-minute data, several parameters related to the basic moments calculated for each gate are examined: Signal-to-Noise power Ratio (S/N), beam power differential, and velocity variance (or width). Although one of the most effective data quality control techniques is a running comparison, this study will attempt to identify only those parameter thresholds indigenous to their respective six-minute profiles, in the hope of retaining as many mesoscale atmospheric features as possible. This study also proceeds with the presumption that by improving six-minute profiles, the hourly consensus will be improved.

In order to place any credence on these thresholds it was necessary to analyze the largest data base possible. Unfortunately due to the combination of power outages, international project requirements, and equipment maintenance downtimes, the data base is limited. Also, in order to compare these thresholds the direction and speed of the prevailing winds would have to be the same. By using the profiler consensus data, a 10-hour period on 02 May 1990 (0600-1600 UTC) was chosen which displayed the most uniformity over time in the 5000-7000 m levels. Based on findings from the previous section, this is the highest elevation which the radar can feasibly measure reliably, i.e., within $3\text{-}4\text{ m s}^{-1}$. The upper atmosphere (above 7 km) was assumed to be less variable than the lower levels (no major synoptic-scale traveling features could be identified in the NMC upper air analyses), and the lower atmospheric layers below 5 km were probably just as variable as at any other time period which could be chosen (again, there were no identifiable wind shifts from frontal passages, for example, which could be identified). The manufacturers consensus data for this analysis period is presented in Fig. 25, and does in fact indicate very uniform conditions.

The sensitivity of the receiver electronics is expected to be a limiting factor. This is expressed as a ratio of returned signal strength to noise. Signal-to-Noise (S/N) was first calculated for each of the profile gates from

$$S/N = \text{Power} - [\text{Noise} + 10 \log_n(\omega)],$$

where *Power* is the integrated power of the peak signal, *Noise* is the signal strength of noise under the peak, and ω is the bandwidth to compensate for the noise not being integrated. In the analysis, $\omega = 256$, for 256 different sampling points in the frequency

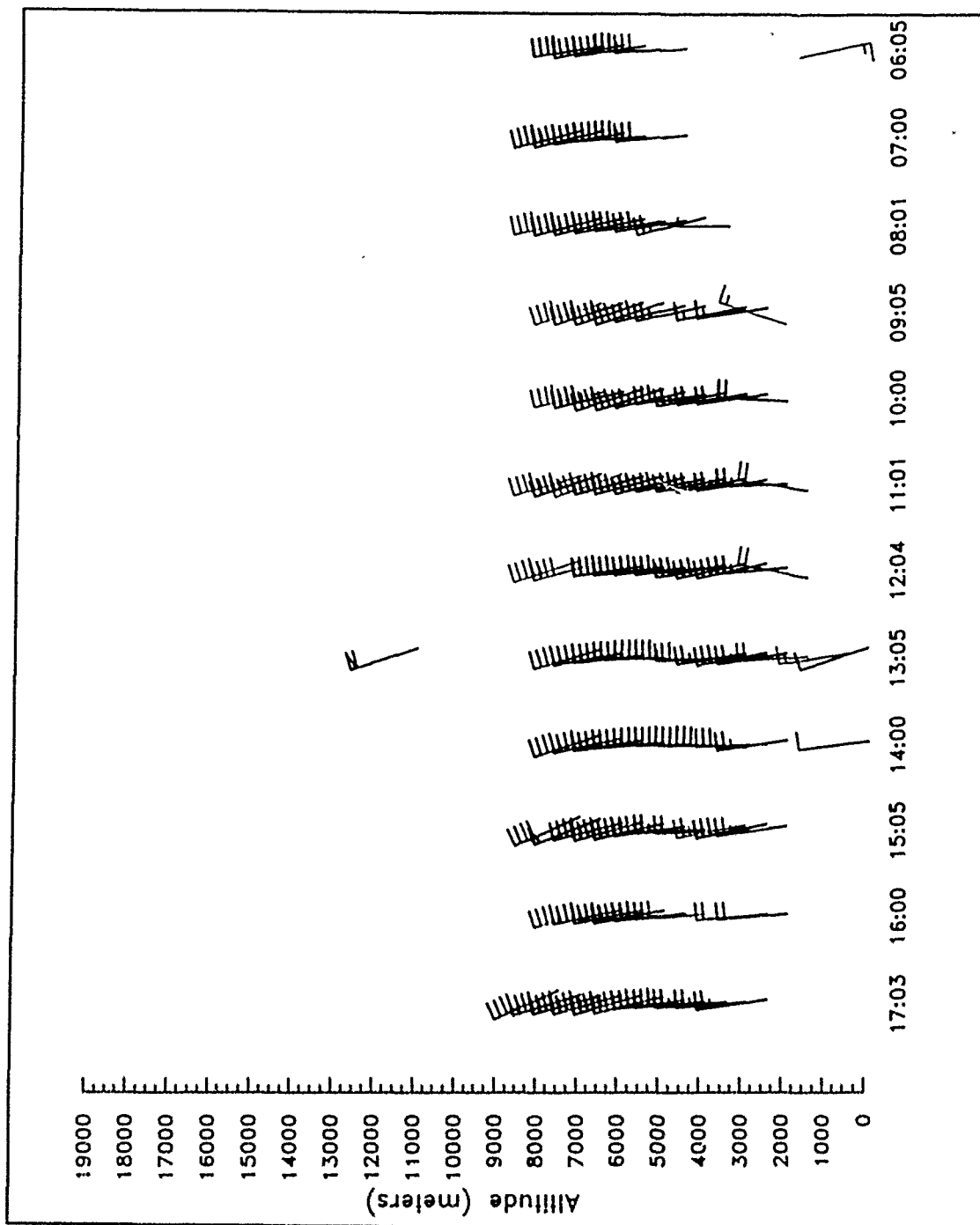


Fig. 25. Profiler Hourly-consensus Wind Data from 0605 to 1703 UTC 02 May 1990: This consistent period represents the data set used to calculate specific thresholds from the spectral moments.

spectrum. Next, the U and V wind components from the six-minute files were decomposed into the original radial velocities. Each of these radial velocities are plotted versus their associated S/N value in Fig. 26, all heights included. The result is a large concentration of points above -19 dB, and, conversely, a very broad scatter of points below -19 dB. Statistically the standard deviation decreases dramatically, as noted in Table 3. The S/N thresholds in Fig. 26 are slightly different in each of the beams, e.g., -18 dB might be used as a value instead of -19 dB--which is presumed to be related to the direction of the prevailing wind, out of the north, which would favor the X-beam. Further studies on larger data sets of profiler wind data could better define this threshold.

Table 3. S/N THRESHOLD STATISTICS

Velocity Component	< -21 dB	-21to-20 dB	-20to-19 dB	-19to-18 dB	> -18 dB
X	29.94	23.86	10.36	8.84	6.47
Y	41.72	31.09	24.45	10.16	10.20

As discussed earlier, the profiler resolves horizontal winds by sampling large volumes of air by offset beams displaced by several meters from one another. Therefore, a threshold is needed to throw out data where supposedly one beam will lock on a helicopter, airplane, or atmospheric noise and possibly even ionospheric noise. Thus, to relate the two beams a power difference is calculated, simply one returned power value subtracted from the other. Figures 27 and 28 represent the power difference between the X and Y-beams, for above 5000 m and less than 3000 m respectively. Above 5000 m the beam power differential does not affect the mean velocity nor the standard deviation of the data points, that is to say, the density of markers seem to be equally dispersed around the mean wind velocity component. This is presumably because the signals are relatively so much weaker. Below 3000 m, however, a shift in the mean velocity is evident when a 5 dB differential is exceeded; the mean velocity and standard deviation are plotted out separately in Fig. 29. In the X-beam, the shift in mean velocity is quite evident above 5 dB, but not so evident in the Y-beam (a shift of only 1 m s^{-1} at 6 dB). The standard deviation throughout the plots, represented by the length or range of the shaded bars, show no apparent trend. Again, the X-beam statistics are presumed more prominent due to the orientation to the prevailing winds. Subjectively, by eyeballing individual wind barb plots which highlight suspected "bad" winds, the 5 dB value can

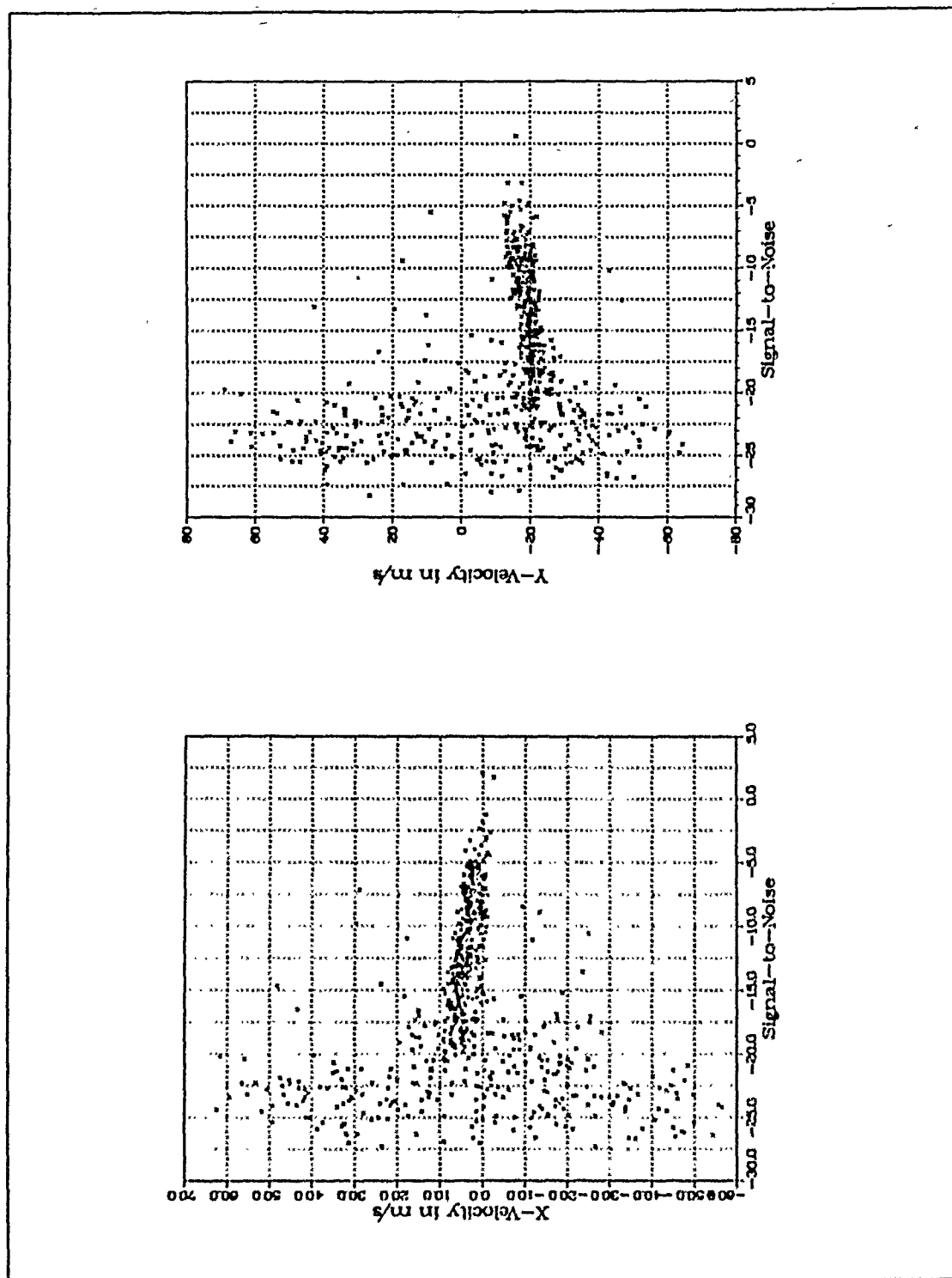


Fig. 26. Signal-to-Noise Threshold Determination

be refined to 6 dB, i.e., more good data in relation to the consensus is retained. After all, an objective of this study is to make the six-minute profiles as representative and as useful as possible.

Finally, the velocity variance was examined. This proved the most difficult threshold to determine. The premise was that the manufacturer's algorithm could not distinguish between two different peak velocities, and, consequently, would average out the two peaks--effectively masking the true wind velocity by the presence of another signal, such as rain or helicopters. This is illustrated by Fig. 30 at 914 to 1214 m in the spectrum analysis. The vertical bar indicates the velocity which the manufacturer's algorithm calculated, yet there are two peaks, one of which is false and the other which yields the data desired. Unfortunately, there were only five sets of spectra with this feature which were obtained during the first month of operation, therefore only a subjective analysis based on a very small data set could be achieved. By comparing the velocity variance contained in the six-minute data to five sets of spectra, a velocity variance of 3.0 m s^{-1} was chosen; and it was only in the lowest 2 km where the velocity variance ever exceeded this value, possibly due to extreme turbulence within the inversion layer.

If each of these criteria are applied to the six-minute profiles, the six-minute profiles should resemble the manufacturer's consensus. Fig. 31 shows these side-by-side comparisons of the six-minute data and the manufacturer's consensus. Each of the colors represent data which would be thrown out by the three thresholds determined earlier in this section: red barbs are winds which exceed the velocity variance, cyan barbs exceed the power differential between the two beams, and green barbs exceed the minimum power requirements. Black wind barbs conversely are classified as the good data. It appears evident from this final product that quality control within the six-minute data is definitely useful, in that the black-colored barbs match well with the consensus data. Generally, the height of the radar is limited by the return strength of the signal, which is related to the amount of humidity present. Preliminary data from Kadena airfield site in Japan during the Tropical Cyclone Motion experiment (TCM-90) proves that higher heights are obtainable in a deep, moist atmosphere, as seen in Fig. 32. There are bad data in the lower atmosphere as well, which are also related to beam difference problems and excessive turbulence.

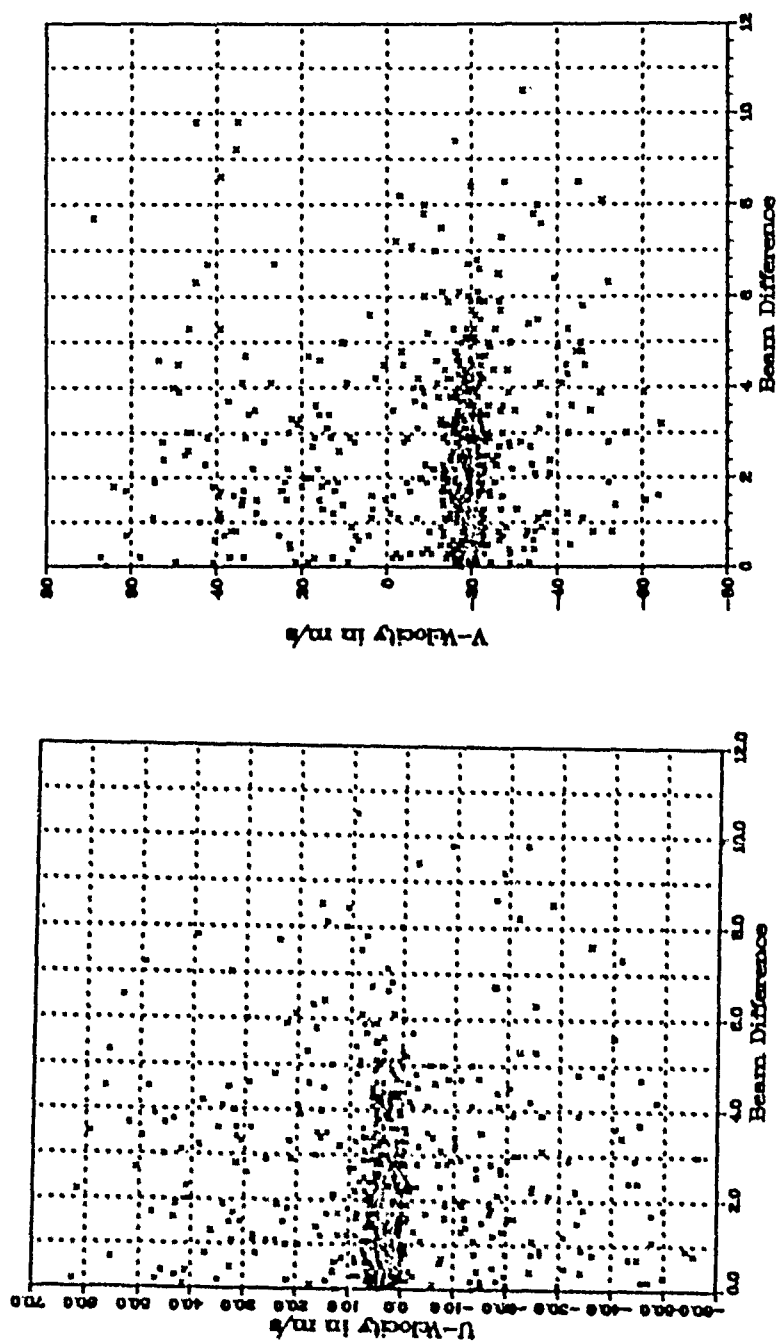


Fig. 27. Plot of Various Power Difference Thresholds Between Off-vertical Beams: Combined Heights from 5197-9197 m for 0605-1505 UTC 02 May 1990.

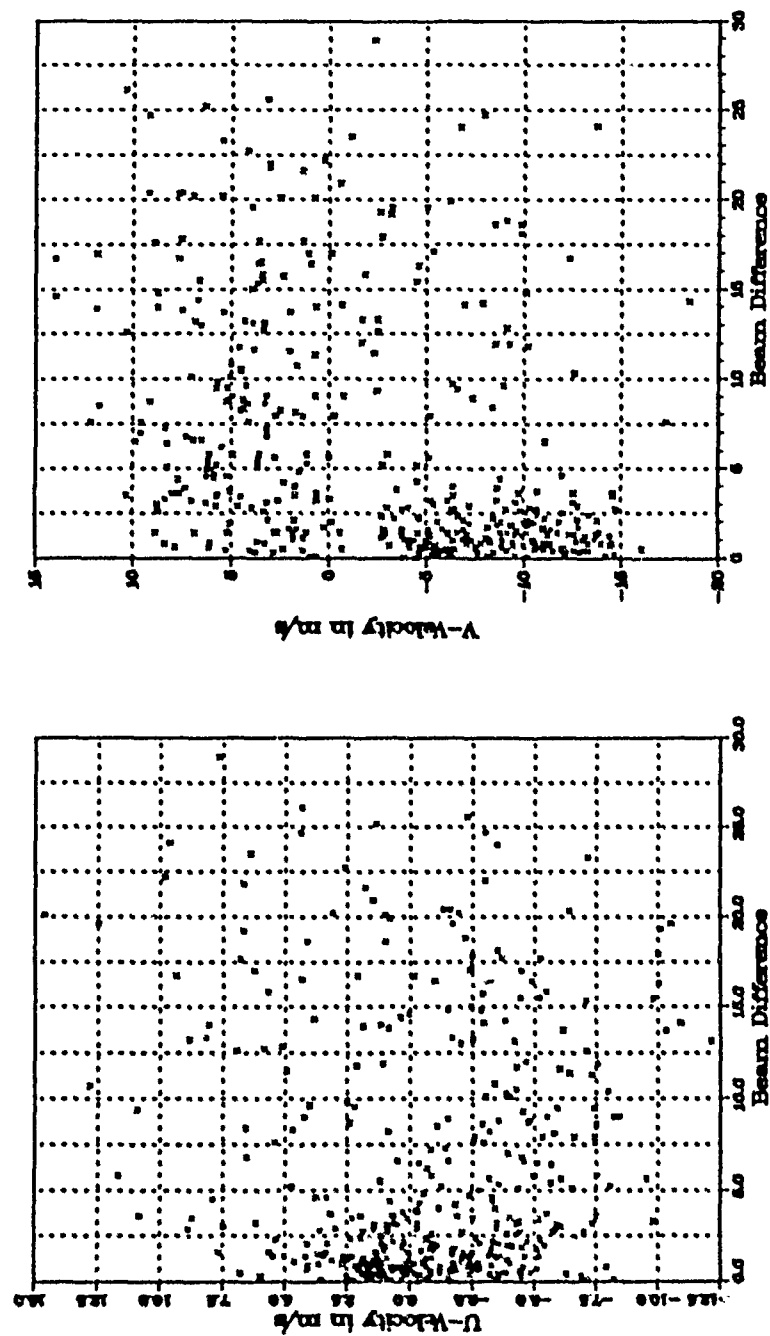


Fig. 28. Plot of Various Power Difference Thresholds Between Off-vertical Beams: Combined Heights below 3000 m for 0605-1505 UTC 02 May 1990.

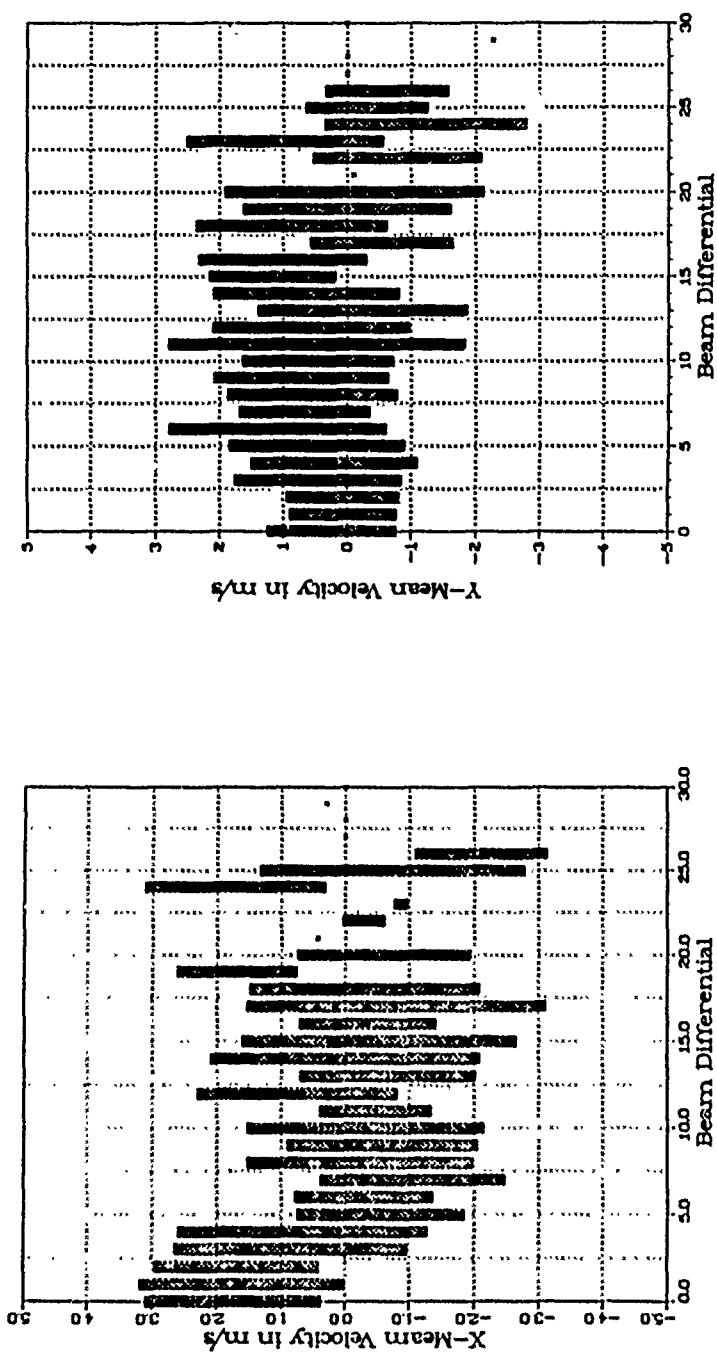


Fig. 29. Plot of Beam Power Difference vs Velocity Standard Deviation and Mean: Combined Heights below 3000 m for 0605-1505 UTC 02 May 1990.

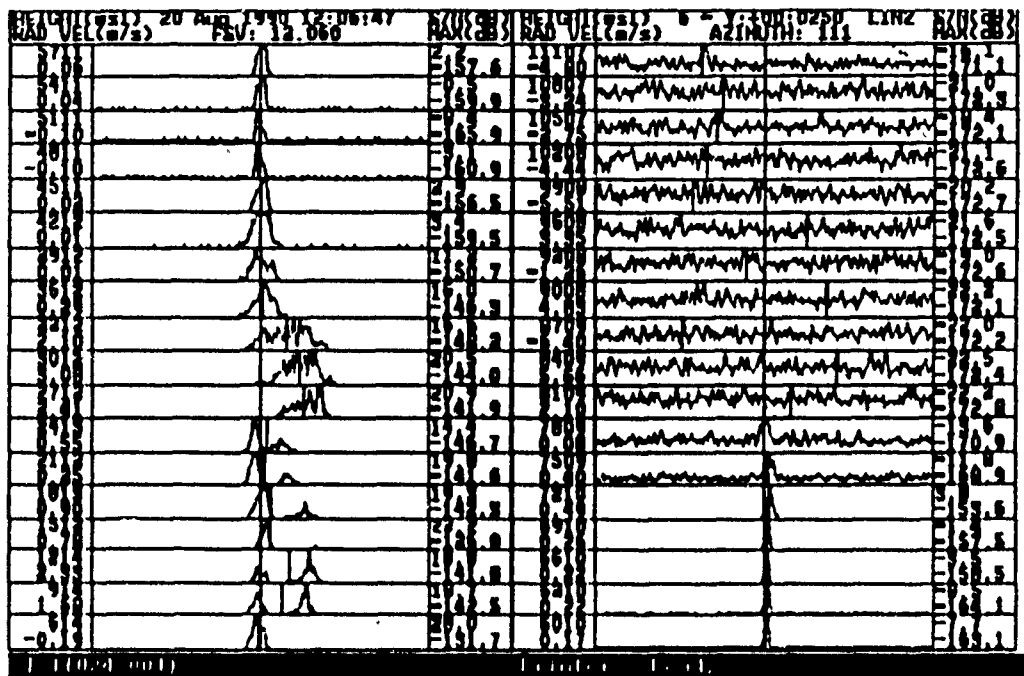


Fig. 30. Example Spectrum Depicting Velocity Shift due to Double Peak

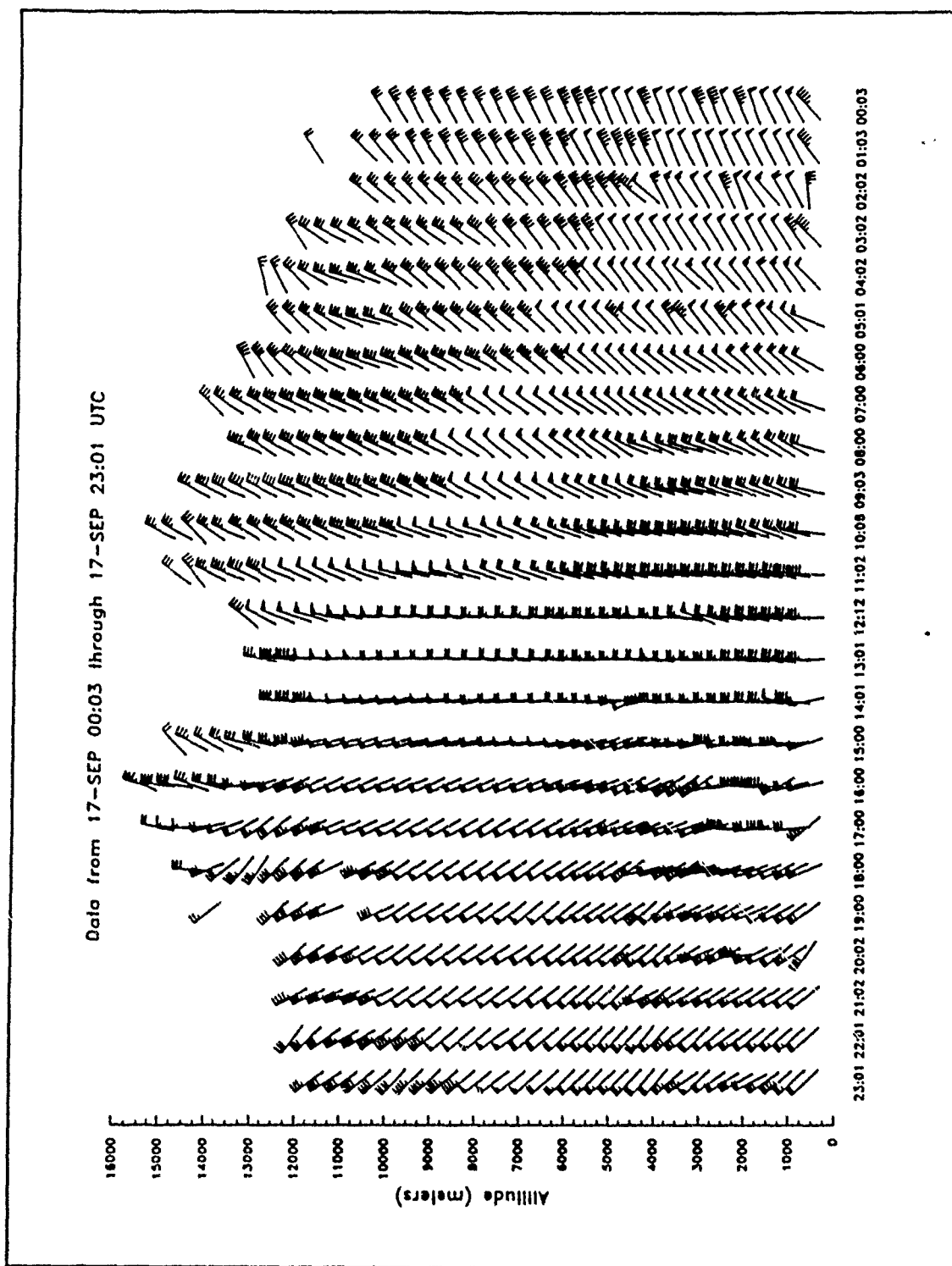


Fig. 32. Representative Consensus Data from TCM-90

C. INVESTIGATION OF VARIABLES AFFECTING CONSENSUS

The two variables which can be feasibly changed within the manufacturer's consensus procedure (i.e., software modifications) are the minimum number of points accepted for the consensus and the velocity threshold.² The minimum consensus number theoretically cannot be improved because the occurrences of incomplete hours (satellite interference automatic shutdown periods, power outages, frontal passages, etc.) prohibits reducing the value below four. This is dictated by research done by NOAA's Wave Propagation Laboratory (as outlined in their contract specifications to purchase a network of wind profilers from UNISYS). Therefore, an attempt was made to improve consensus by varying only the velocity threshold from 2.0 m s^{-1} .

Subjectively, Fig. 33 illustrates that by varying the velocity threshold from 1.0 to 5.0 m s^{-1} there generally is little effect on the final hourly consensus profile. However, when the velocity threshold is diminished below 1.0 m s^{-1} , there are noticeable deviations regarding direction of the individual wind barbs from the Tycho-provided consensus, which is most notable below 2000 m . To validate the visual conclusions, the difference between the new consensus (obtained with the new threshold) and the manufacturer's consensus was calculated. Then the error, or "departure", of each individual six-minute datum was computed by subtracting the six-minute velocity from the new consensus. Statistically, differences between the six-minute u-velocity and v-velocity components and the consensus confirm what is seen graphically, in that there are numerous "departures" greater than 2.0 m s^{-1} . Graphically, there are also notable deviations from the Tycho hourly-consensus when a velocity threshold of 5.0 m s^{-1} is exceeded, which are again reflected in the statistical data. For a velocity threshold above 5.0 m s^{-1} there are numerous "departures" of the six-minute data from consensus, i.e., "departures" greater than 2.0 m s^{-1} .

These results indicate that there remains a possibility of reducing the velocity threshold below 2.0 m s^{-1} , in order to improve the reliability of the hourly data. This threshold was not necessarily important for the period on which this study concentrated, however, in other atmospheric conditions, implementation of a diminished velocity threshold may be useful. For example, this technique of reducing the velocity threshold might be more effective higher in the atmosphere, where the signal is weak and, subsequently, the consensus number would be low.

² Personal conversation with Tycho Industries' technicians.

The data also indicates that the profiler accuracy can fall within 2.0 m s^{-1} , since a consensus can be obtained with the velocity threshold set at 1.0 m s^{-1} . A larger data set of rawinsonde, or more accurate truth data, would probably confirm the accuracy of the profiler to be within $1\text{-}2 \text{ m s}^{-1}$.

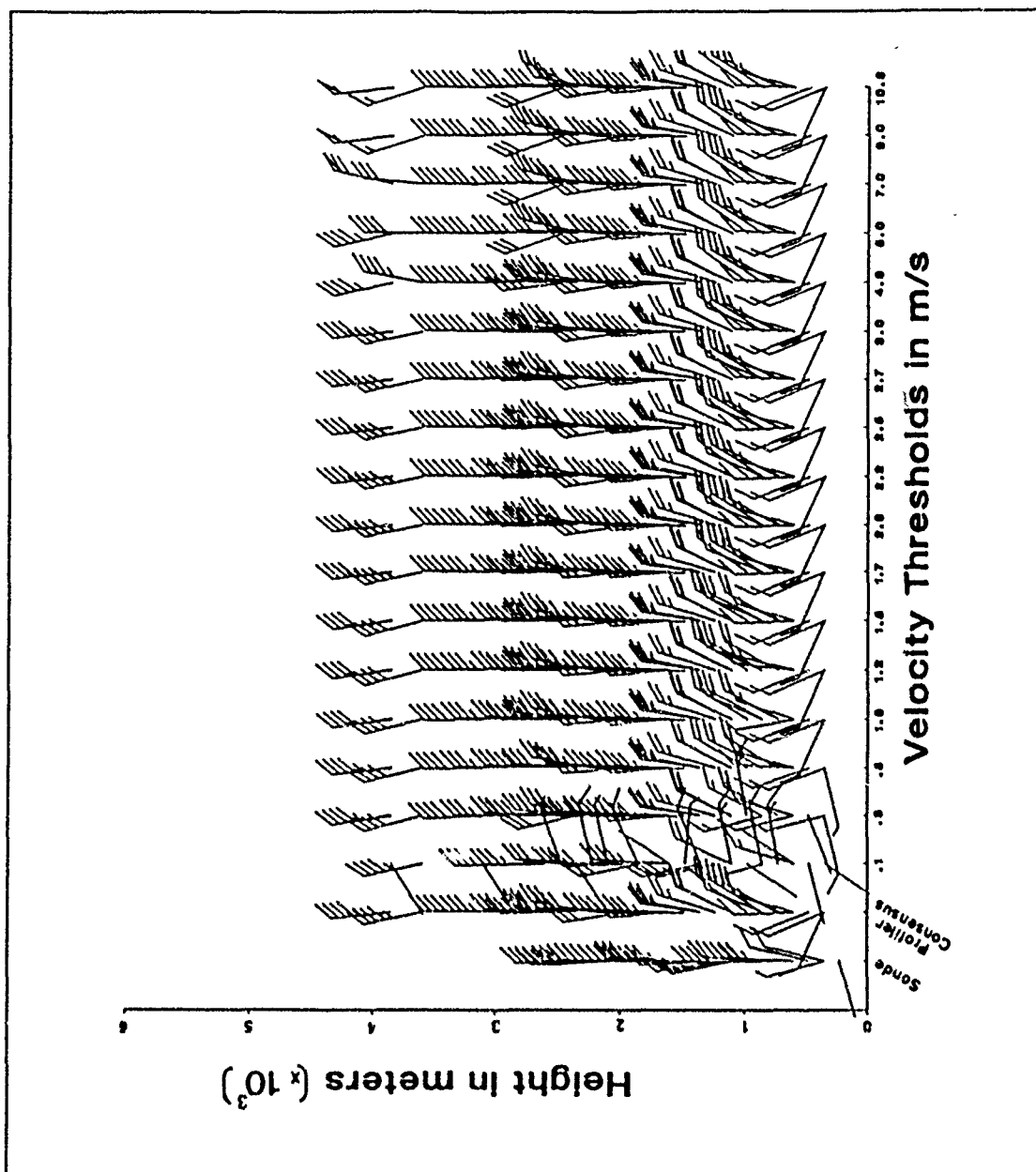


Fig. 33. Comparable Hourly Consensus Profiles from 02 May 1990.: Different hourly consensus profiles are plotted utilizing different velocity thresholds varying from 0.1 to 10.0 $m s^{-1}$. The hourly consensus based on the manufacturer's 2.0 $m s^{-1}$ velocity threshold is plotted as "Radar Profiler Consensus". The rawinsonde data associated with this period is plotted as the "Sonde" profile in the left column.

IV. METEOROLOGICAL ANALYSIS USING SIX-MINUTE PROFILER DATA

With the quality of six-minute data now established, as well as some limitations which constrain the accuracy, the presence of high-frequency meteorological phenomena can be examined. Reviewing the 30 March 1990 to 05 May 1990 period of profiler operation, only one distinct subperiod in the pressure, temperature, wind speed and direction, and moisture data seemed to indicate the presence of any high-frequency fluctuations. The subperiod occurred on 02-03 May 1990. Five-minute meteorological data from 03 May 1990 recorded at the Monterey Bay Aquarium Research Institute (MBARI) is presented in Appendix G. The wind is highly variable from 0000 to 0700 UTC, and periodic pressure perturbations occur at 0800 and 1100 UTC in the MBARI data. The pressure perturbations (approximately 1 to 1 1/2 mb over one-half hour) though subtle, are large compared to the normally smooth diurnal change experienced in the Monterey Bay area. These pressure perturbations have been verified with other high-temporal resolution barograph data from the NPS Meteorological Laboratory.

A. VELOCITY AND VELOCITY PERTURBATION FIELD ANALYSIS

The most common display of six-minute profiler data is the "time versus height" field of velocity. An alternative and possibly more useful way to examine the presence or absence of high-frequency phenomena is to examine the velocity perturbation field; i.e., the vector velocities remaining after a mean value has been removed. Both of these methods will be utilized.

Although the six-minute data of horizontal wind components can yield useful and reliable information, detection of high-frequency, low-amplitude fluctuations can be difficult due to the relatively high mean horizontal wind speed. However, vertical motion measurements could reveal high-frequency perturbations, since the mean vertical motion along the West Coast under the influence of the subtropical high pressure ridge is on the order of centimeters per second. In fact, periodic motions reveal themselves clearly in Fig. 34, a time-height series of vertical motion. A demarcation line is drawn in Fig. 34 to separate general regions of upward and downward motions. The regions are characterized by maximum vertical velocities on the order of 1 m s^{-1} . The demarcation line appears to be both oscillatory and periodic, approximately 2 hours and 10 minutes. Because the approximate structure of the oscillations are too small to be sampled by si-

multaneous measurements from the available weather network, some principles of time-space conversion, as presented by Forbes *et al.* (1989) was implemented. Forbes states that "the object of time-space conversion is to take frequent measurements from a single location while the prevailing synoptic winds [and high-frequency propagating phenomena] pass overhead." When time-space conversion is applied to Fig. 34, an internal-gravity or Kelvin-Helmholtz-like wave is suggested. It would be an error to assume that this high-frequency phenomena is southward propagating simply because the prevailing winds are out of the north. Kelvin-Helmholtz and internal-gravity waves traveling along a stable boundary could easily propagate against the prevailing winds. More information from other sites would have to be presented to determine a direction of wave propagation.

Given the presence of some periodic forcing in the vertical motion, it is anticipated that corresponding periodic forcing is present in the horizontal velocities as well. To examine the periodic forcing of the horizontal velocity, velocity perturbations were calculated by subtracting the mean velocity from the individual six-minute observations (see Fig. 35). The mean was calculated at each level from the long-term consensus for a ten-hour period beginning 0600 UTC 02 May 1990. The horizontal velocity perturbation components reveal a similar periodicity as noted in the previous paragraph for the vertical velocity, although it is not as well defined. As expected from the "typical" pattern of spring/early-summer winds in the area, there was the presence of the land to sea breeze shift (regions highlighted by a solid line at approximately 2000 m within Fig. 35). However, Fig. 35 shows perturbed winds from the southwest between 4000-6000 m from 0923 to 1012 UTC and from the northeast from 1317 to 1406 UTC, which correspond to two of the periods dominated by downward motions in Fig. 34. These regions of consistent, large perturbation velocities in the direction of the prevailing winds also have been highlighted in Fig. 35 by regions bordered by thick dashed lines. Note that the direction of perturbed winds in these latter regions are opposite in direction to each other, yet both occur during corresponding times of downward motion in Fig. 34, which is hard to explain given the limited data and therefore left for future study. However, the directionality of these perturbations (aligned northeast-southwest) suggest that, considering conditions over the ocean are uniform and the perturbations are due only to the high-frequency source, the source is located to the northeast, or in the general direction of the pass between Atherton Peak and Fremont Peak.

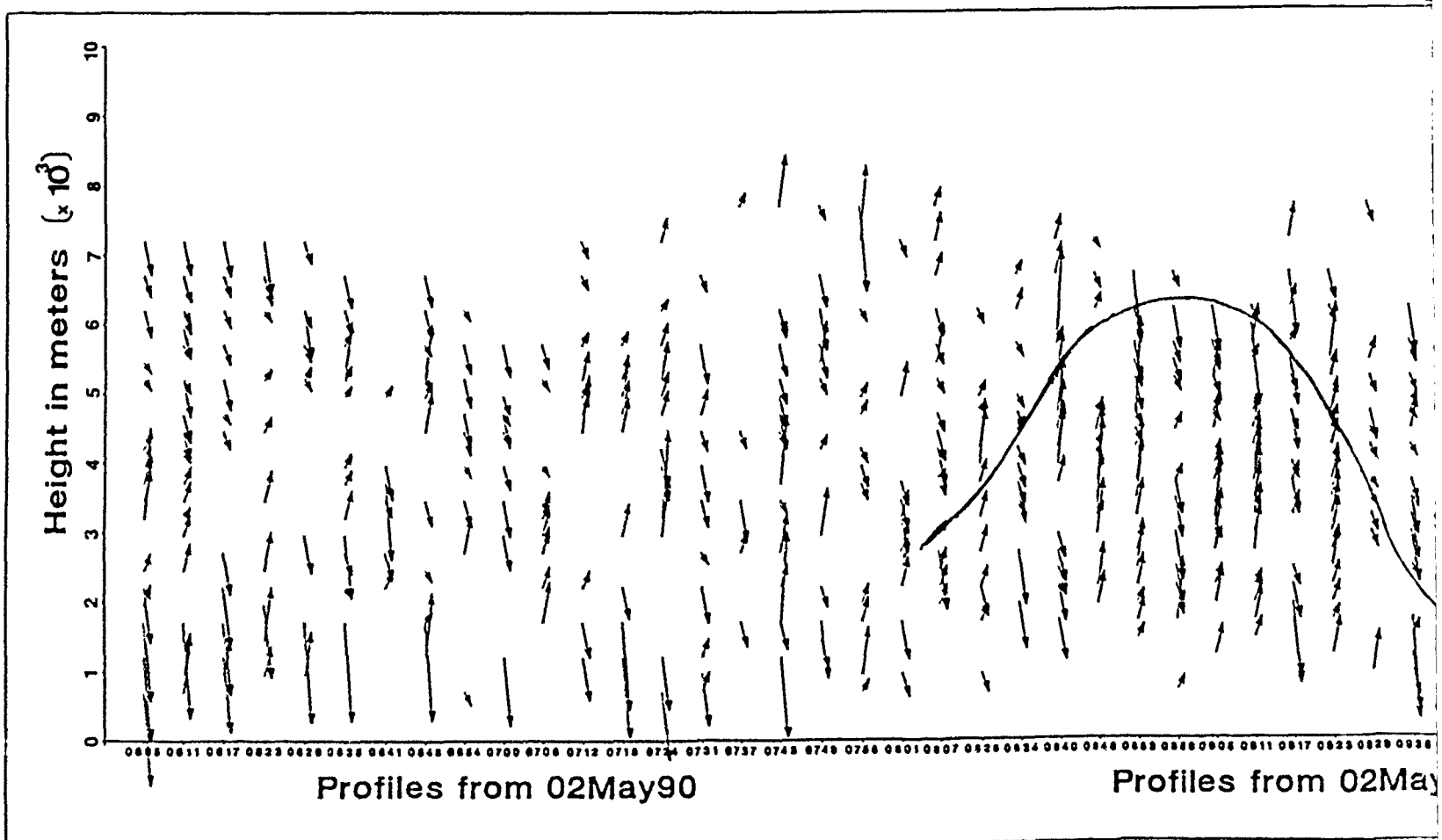
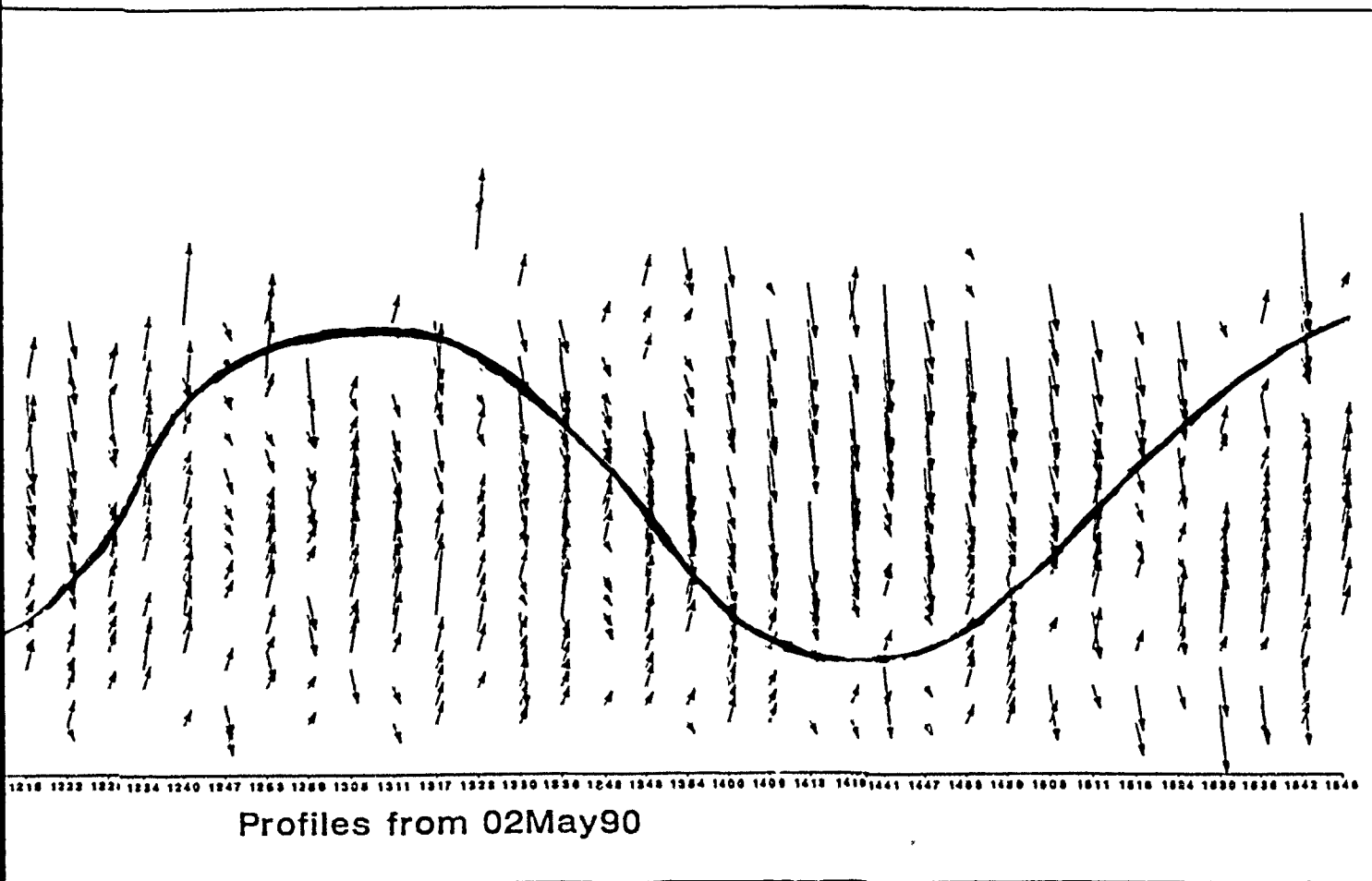


Fig. 34. Plot of NPS Profiler Vertical Wind Component for 02 May 1990: One inch equals 1 m s^{-1} . Arrows have been offset from the vertical to eliminate overlap.



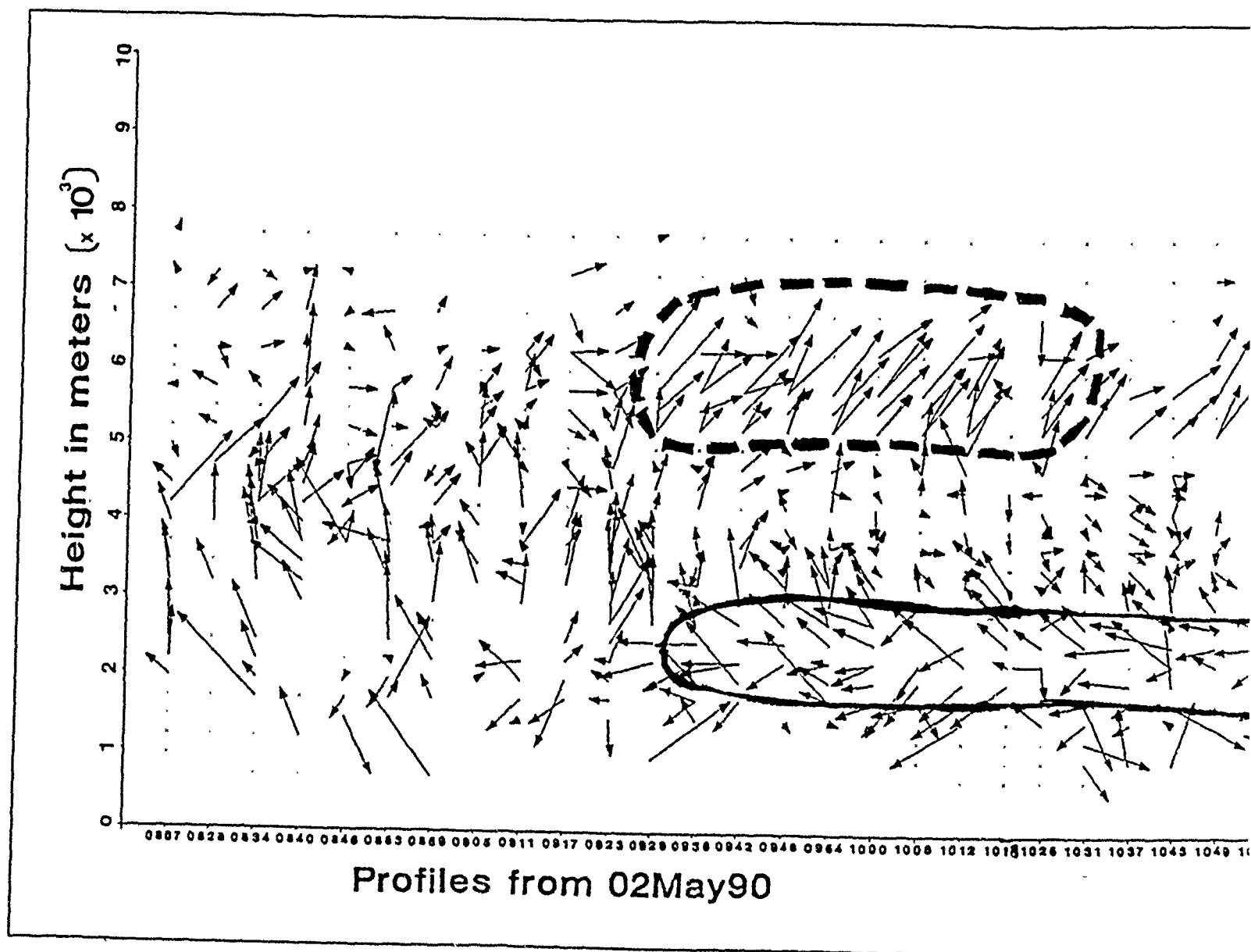
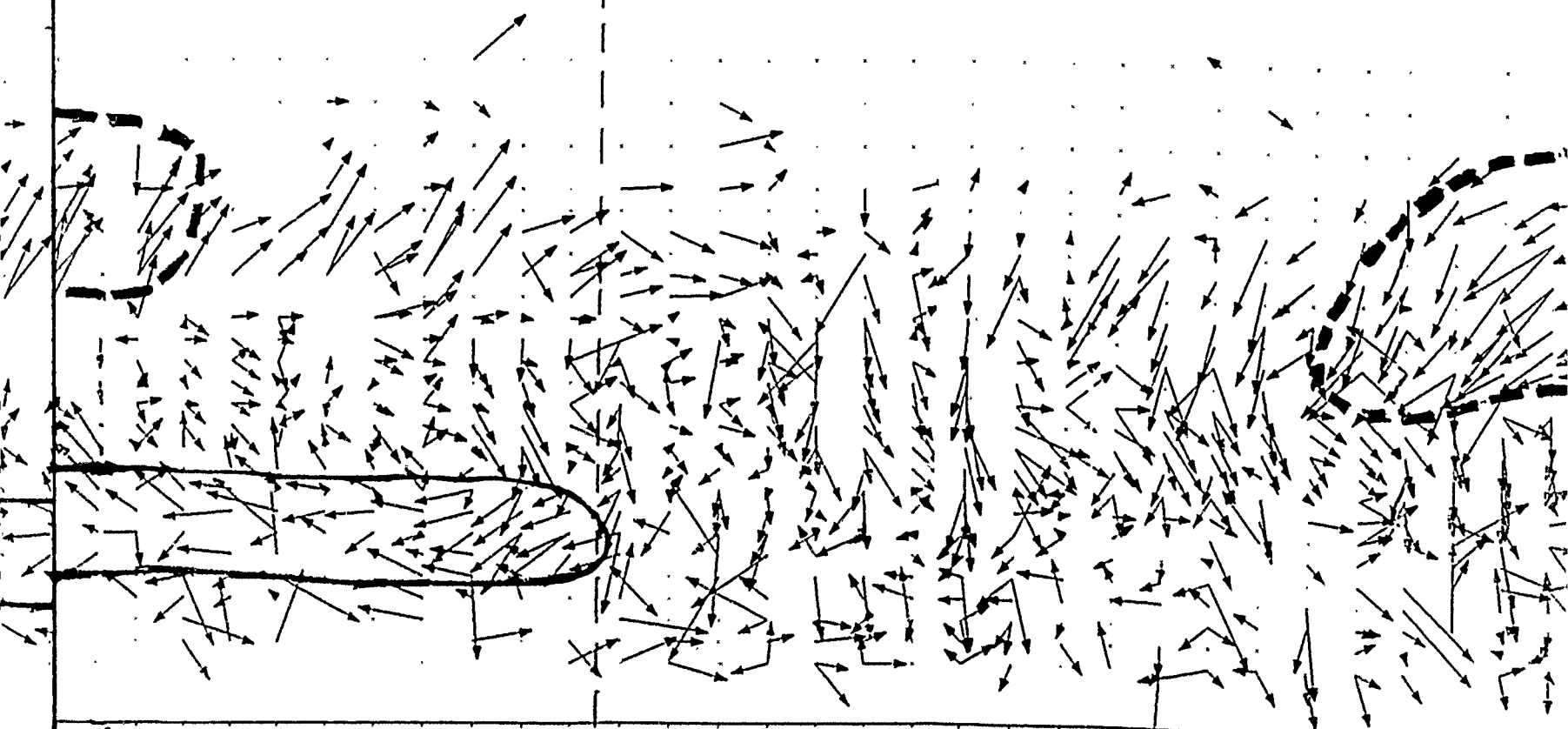
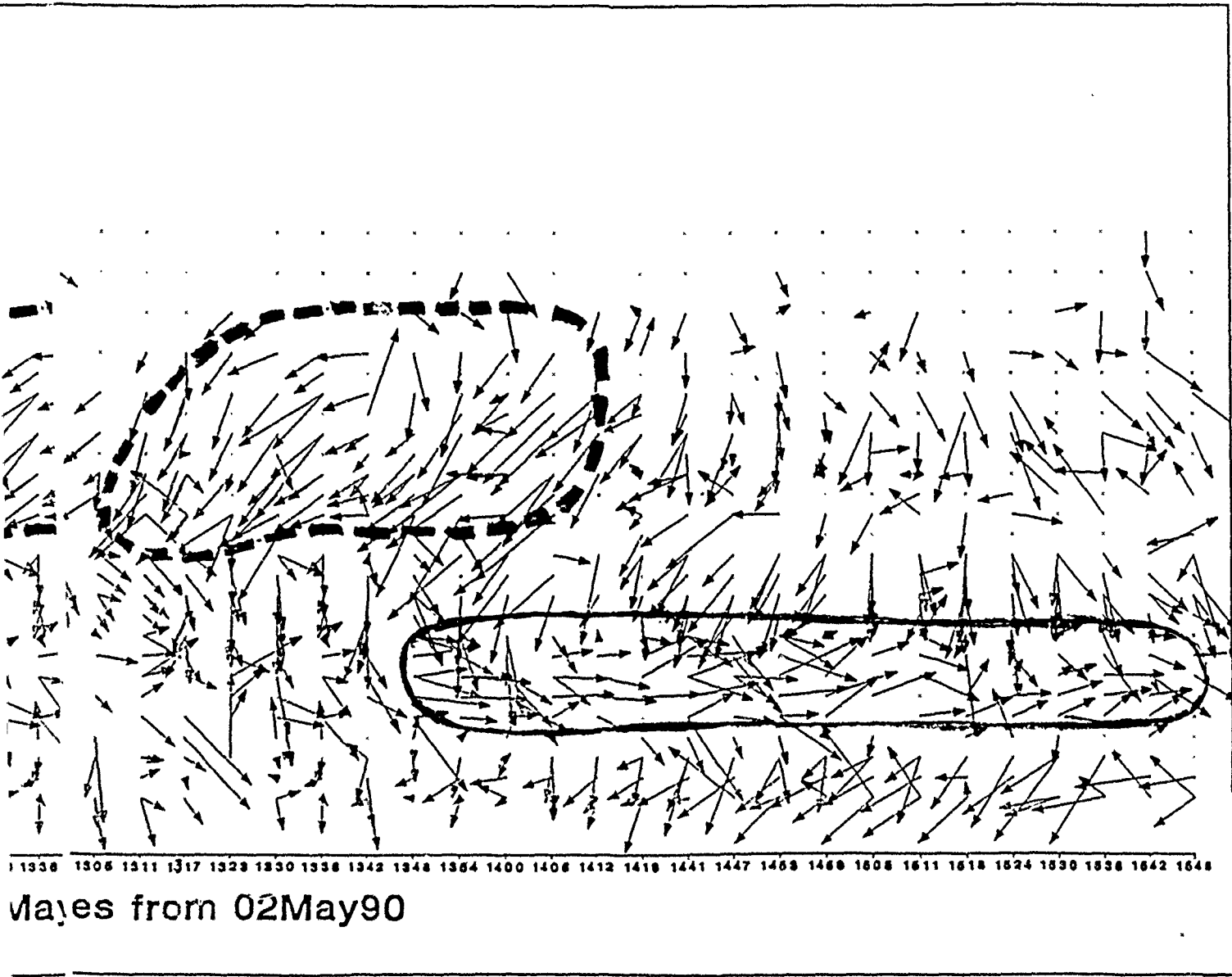


Fig. 35. Plot of NPS Profiler Horizontal Wind Perturbations for 02 May 90: One inch equals 10 m s^{-1} .



1018 1026 1031 1037 1043 1049 1056 1101 1108 1114 1120 1139 1146 1161 1167 1204 1210 1216 1222 1228 1234 1240 1247 1263 1269 1306 1311 1317 1323 1330 1336

Profiles from 02Ma



B. THERMAL ADVECTION FROM SIX-MINUTE DATA

To better understand the high-frequency phenomena observed by the vertical velocity and horizontal perturbation velocity analysis in the previous section, some estimate of the high-frequency thermodynamic properties of the atmosphere would be useful. Although the profiler does not measure thermal properties of the atmosphere without a special acoustic modification (RASS), some aspects of the thermal structure can be inferred from profiler wind data. In particular, a single wind profiler measures

$$u, \frac{\partial u}{\partial z}, \frac{\partial u}{\partial t};$$

$$v, \frac{\partial v}{\partial z}, \frac{\partial v}{\partial t};$$

$$w, \frac{\partial w}{\partial z}, \frac{\partial w}{\partial t}.$$

From these quantities, the thermal advection can be estimated, given some rather severe assumptions about the flow.

To determine the thermal advection, it is assumed that all Coriolis, earth curvature, frictional, and vertical acceleration terms are negligible compared with those involving the vertical pressure force and the force of gravity. This leads to the hydrostatic equation presented by Holton, 1979

$$dz = \frac{dp}{\rho} g, \quad (1)$$

where dz is the layer thickness, dp the pressure difference between layers, ρ the density, and g the acceleration of gravity. The thermodynamic state of the atmosphere at any point is determined by the values of pressure (p), virtual temperature (T_v), and density (ρ) at that point. If the fluid can be regarded as incompressible these field variables can be related to each other by the equation of state for an ideal gas as presented by Campbell (1973)

$$p = \rho R_d T_v, \quad (2)$$

where R_d is the gas constant for dry air. Solving Eq. (2) for ρ , and then substituting Eq. (2) into Eq. (1)

$$dz = -\frac{R_d T_V}{g} \frac{dp}{p}. \quad (3)$$

Integrating Eq. (3) throughout the layer gives

$$\int_{z_1}^{z_2} dz = \int_{p_1}^{p_2} \frac{R_d T_V}{g} \frac{dp}{p}. \quad (4)$$

The term on the left side of Eq. (4) is a definite integral, and R_d and g are constants; therefore, from Eq. (4)

$$\Delta z \Big|_{z_1}^{z_2} = -\frac{R_d}{g} \int_{p_1}^{p_2} T_V dp \int_{p_1}^{p_2} \frac{1}{p} dp. \quad (5)$$

Next, assume that temperature is linear throughout the layer and Eq. (5) becomes

$$\Delta z = -\frac{R_d}{g} \bar{T}_V \int_{p_1}^{p_2} d \ln p. \quad (6)$$

Two more equations are needed. Holton presents the hypsometric equation, which relates pressure differences to height or thickness changes as

$$\Delta z = \frac{(\Delta \ln p) R_d}{g} \bar{T}_V. \quad (7)$$

Finally, an assumption is made that the accuracy of the geostrophic wind as an approximation to the observed wind is a good one, and the difference is negligible, i.e., Coriolis force exactly balances the pressure gradient force. Gill (1982) presents the geostrophic approximation in component form as

$$u_g = -\frac{g}{f} \frac{\partial z}{\partial y}, \text{ and} \quad (8)$$

$$v_g = \frac{g}{f} \frac{\partial z}{\partial x}; \quad (9)$$

or in the vector form,

$$\vec{V}_g = \frac{g}{f} \vec{k} \times \nabla_p z. \quad (10)$$

The vector difference is clearly

$$\Delta \vec{V}_g = \vec{V}_{g2} - \vec{V}_{g1}, \quad (11)$$

which by substitution of Eq. (10) into Eq. (11) yields

$$\Delta \vec{V}_g = \frac{g}{f} \vec{k} \times \nabla_H (z_2 - z_1) = \frac{g}{f} \vec{k} \times \nabla_H (\Delta z). \quad (12)$$

Substituting Eq. (7) into Eq. (12)

$$\Delta \vec{V}_g = \frac{g}{f} \frac{R_d}{g} \ln\left(\frac{p_1}{p_2}\right) \vec{k} \times \nabla_H \bar{T}_v; \quad (13)$$

but, $R_d/g[\ln(p_1/p_2)] = \Delta z/\bar{T}_v$, by Eq. (7), so Eq. (13) now becomes

$$\Delta \vec{V}_g = \frac{g}{f} \frac{\Delta z}{\bar{T}_v} \vec{k} \times \nabla_H \bar{T}_v. \quad (14)$$

By definition of the thermal wind by Holton (1972), and substitution of Eq. (14) into the definition

$$\vec{V}_T \equiv \frac{\Delta \vec{V}_g}{\Delta z} = \frac{g}{f \bar{T}_v} \vec{k} \times \nabla_H \bar{T}_v, \quad (15)$$

or in component form

$$u_T = \frac{\Delta u_g}{\Delta z} = -\frac{g}{f \bar{T}_v} \frac{\partial \bar{T}_v}{\partial y}, \text{ and} \quad (16)$$

$$v_T = \frac{\Delta v_g}{\Delta z} = \frac{g}{f \bar{T}_v} \frac{\partial \bar{T}_v}{\partial x}. \quad (17)$$

Finally, temperature advection can be defined as

$$\frac{\partial T}{\partial t} \equiv T_{Adv} = -\vec{V} \cdot \nabla T, \text{ or}$$

$$T_{Adv} = -u \frac{\partial T}{\partial x} - v \frac{\partial T}{\partial y}. \quad (18)$$

Substitute Eq. (16) and Eq. (17) into Eq. (18), and replace u with u_c (the consensus velocity) yields

$$T_{Adv} = -u_c \left[\frac{\Delta v_g}{\Delta z} \frac{f \bar{T}_v}{g} \right] - v_c \left[-\frac{\Delta u_g}{\Delta z} \frac{f \bar{T}_v}{g} \right]. \quad (19)$$

Realistically, u_c and v_c are not known so u and v , the profiler-derived winds, are substituted. \bar{T}_v was calculated from a formula derived from Stull (1988), $\bar{T}_v = (1 + .61q)\bar{T}$, using data from the 1300 UTC 03 May 1990 rawinsonde launch. Large deviations away from geostrophic balance are possible for six-minute time scales so the geostrophic assumption is likely to produce substantial errors in $V \cdot \nabla T$. Note that this analysis will highlight regions of strong vertical shear in the horizontal ageostrophic (perturbation) winds.

When temperature advection values are calculated from Eq.(19) with the six-minute profiler data, the result is generally nothing short of a random distribution of minimum and maximum values. However, throughout a two-hour period on 03 May 1990, depicted in Fig. 36, a startling consistent pattern of concentrated minimum and maximum values lying along sloped lines is revealed. Again, the profiler does not measure temperature, but if it is assumed for a moment that Fig. 36 truly is temperature advection, then it would be expected to also have packed isotherms in the regions of the large advection values (i.e., packed isotherms would be needed in order that homogeneous atmospheric vertical motion would carry "drastic" changes in temperature.) The high values of temperature advection in Fig. 36, both positive and negative, are probably associated with tighter temperature gradients, but not directly. The slight pressure perturbations that are induced by wave activity also set-up temperature gradients, similar to the packed isotherms Gossard (1990) revealed regarding turbulence in a stratified gas (see Fig. 37). These isotherm gradients in turn set up weak velocity perturbations which are subsequently detected by the profiler. Although this phenomenon is easily depicted using this temperature advection computation, it is actually only an artifact created by the associated weak velocity perturbations observed by the profiler.

Subsequently, the vertical velocity for the period represented in Fig. 36 was also plotted, as Fig. 38. Lines indicating regions of the highest density of extreme temperature advection values from Fig. 36 were transferred to Fig. 38. There is a tendency for

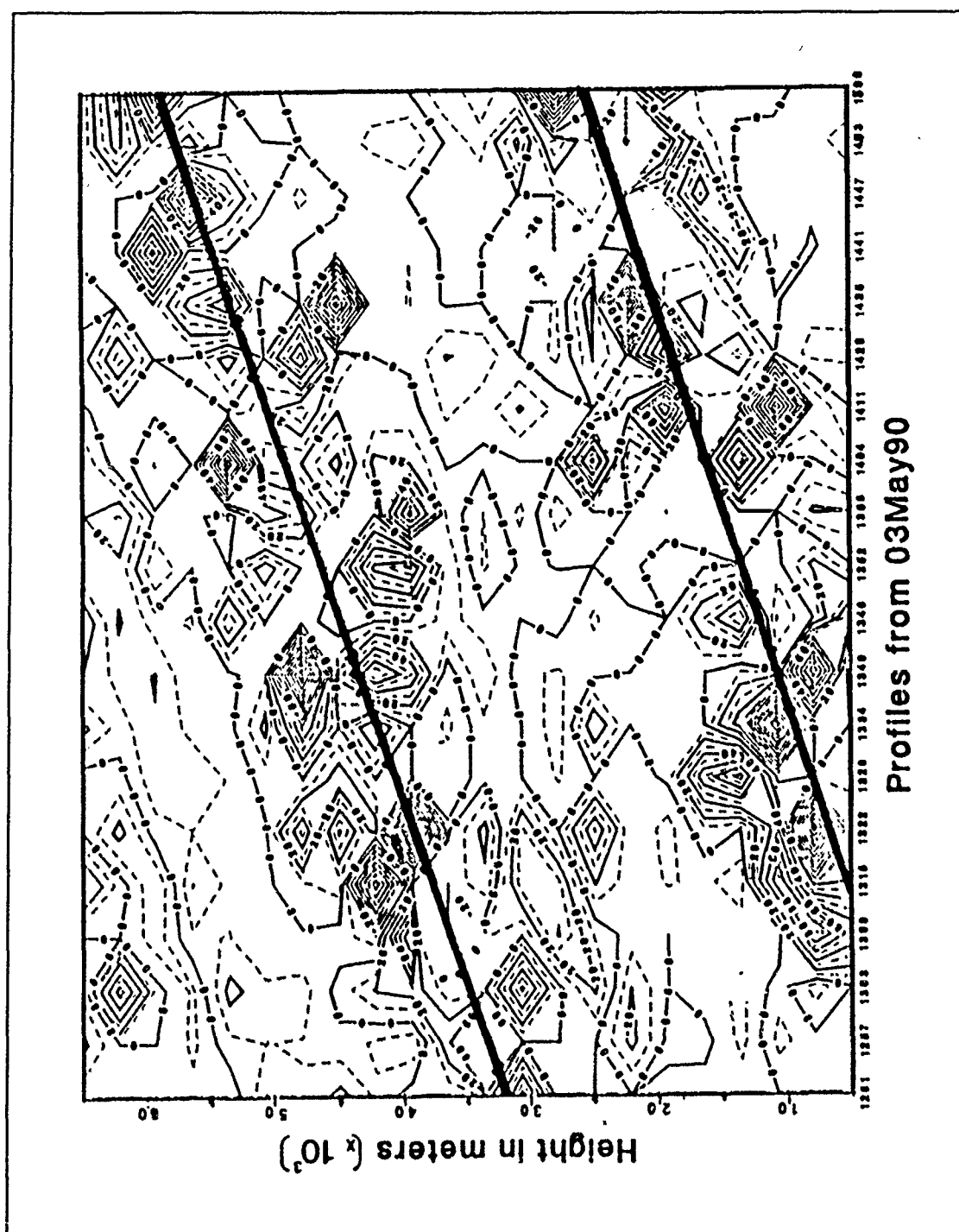


Fig. 36. Temperature Advection Field: Reveals areas of high vertical shear in the horizontal winds.

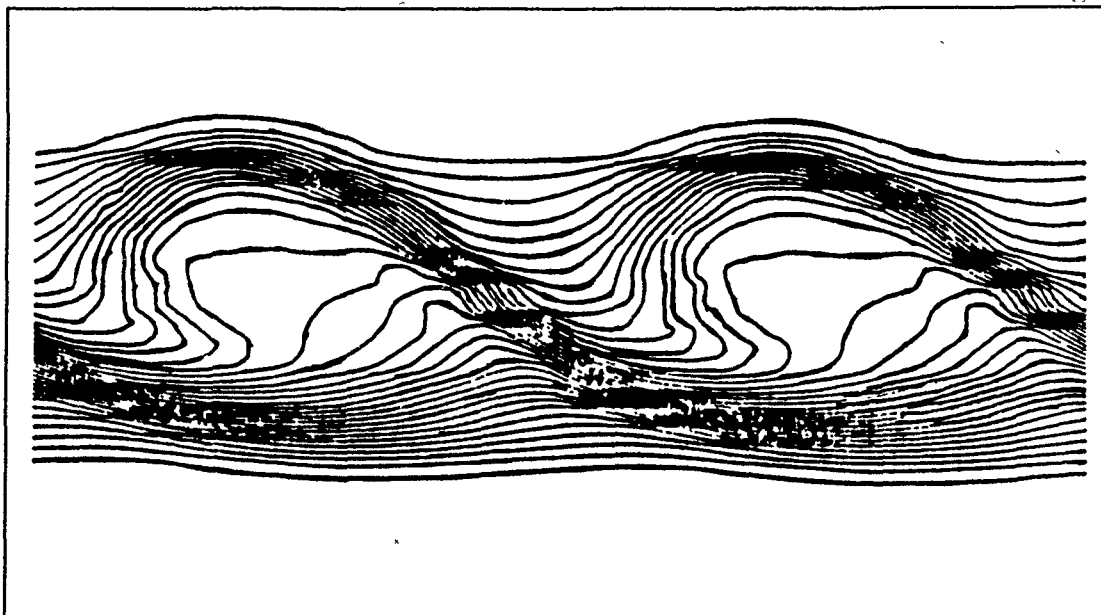


Fig. 37. Packing of Isotherms due to Turbulence in a Stratified Gas: (Source: Gossard (1990).)

vertical convergent winds (Fig. 38) to correspond to the large values of temperature advection (Fig. 36), which supports the idea that substantial changes in the horizontal velocity perturbations are occurring across these layers.

C. SYNOPTIC OVERVIEW FOR 02-03 MAY 1990

Synoptic conditions at the 500 mb and surface, representative of the period 02-03 May 1990, are presented in Fig. 39 and 40, respectively. The combination of an upper-level low height center over southern Arizona and a high pressure ridge along the West coast force prevailing 500 mb winds out of the north over California. Surface conditions along the West coast are influenced by a surface pressure trough extending from the Arizona-New Mexico border to northern California. This trough creates north by north-westerly flow principally parallel to the California coast; however, southerlies lying along the California central coast to the south of Monterey are against the synoptic scale pressure pattern. This suggests a possible mesoscale eddy or low pressure center to the north and west of Monterey.

Local hourly-consensus data from the profiler for the period 02-03 May 1990 are presented in Fig. 41 through Fig. 44. Winds out of the north prevail from 2000-6000 m. The land-sea breeze shifts are evident in the lowest 2000 m of the atmosphere.

Specifically, westerlies depict the sea breeze crossing the Marina shoreline of the Monterey Bay, which persist from approximately 2100 UTC to 0300 UTC. From 0400 UTC to 2000 UTC, the land breeze sets up from the southeast, very much aligned to topography of the Salinas River valley. Hourly observations at Salinas, California (20 km down into the valley, southeast of the Monterey Bay) are presented in Table 4. The onset of the land breeze is evident at 0500-0700 UTC on both days in the hourly surface observations, denoted by the large speed decrease in the northerlies.

The six-minute data for this period of land/sea breeze shift is presented in Fig. 45. As seen from the six-minute data presented in Fig. 45, there is a "burst" of easterlies in the lowest 4000 m after about 0414 UTC 02 May90 (as well as on 03 May 90 at approximately the same time). (This "burst" is more evident in the hourly consensus data, Fig. 41.) The easterlies are really a vector summation of two different circulation patterns: (1) the land breeze from the south by southeast, and (2) the prevailing northeasterly synoptic-scale surface flow. This "burst" of easterlies occurs because the sea breeze (out of the west) dams the synoptic northeasterlies between Atherton and Fremont Peaks, and when the sea breeze collapses the northeasterlies now flow through the pass easily and abruptly. (Refer to Fig. 2 for topography of the local area.)

D. A PROBABLE EXPLANATION OF OBSERVED HIGH-FREQUENCY PHENOMENA

Although the determination of the source and propagation nature of the oscillatory wave seen in Fig. 34 are beyond the scope of this study, a hypothesis is required to plan future research work. Two possible explanations are that some type of internal-gravity or Kelvin-Helmholtz instability waves exist. Although the wave pattern certainly resembles the propagation nature of an internal-gravity wave, a calculation of the Vaisala-Brunt frequency at 2000 to 4000 m yields a value of $9.7 \times 10^{-3} \text{ s}^{-1}$ which equates to an oscillatory period of approximately two minutes. This period differs considerably from the two hour period which is seen Fig. 34. Therefore, I conclude that the high-frequency phenomena is probably due to shear instability, specifically from the shear induced by the reversal of the sea breeze (i.e., land breeze southerlies under the prevailing northerlies aloft). This is particularly convincing as the oscillations begin shortly after the land breeze begins. Additional six-minute profiler data can be used to confirm this hypothesis in the future.

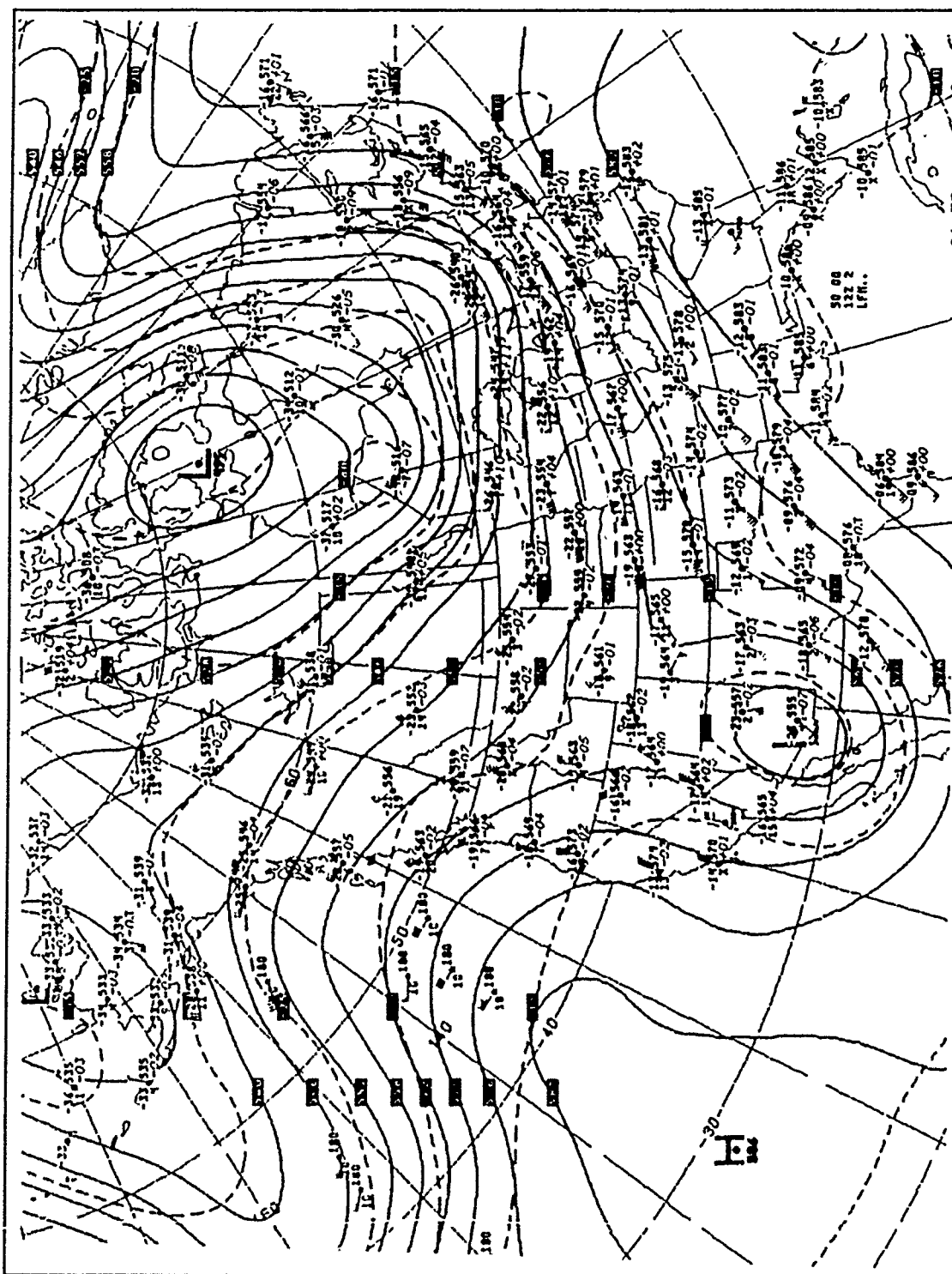


Fig. 39. NMC 500 mb Analysis for 1200 UTC 02 May 1990



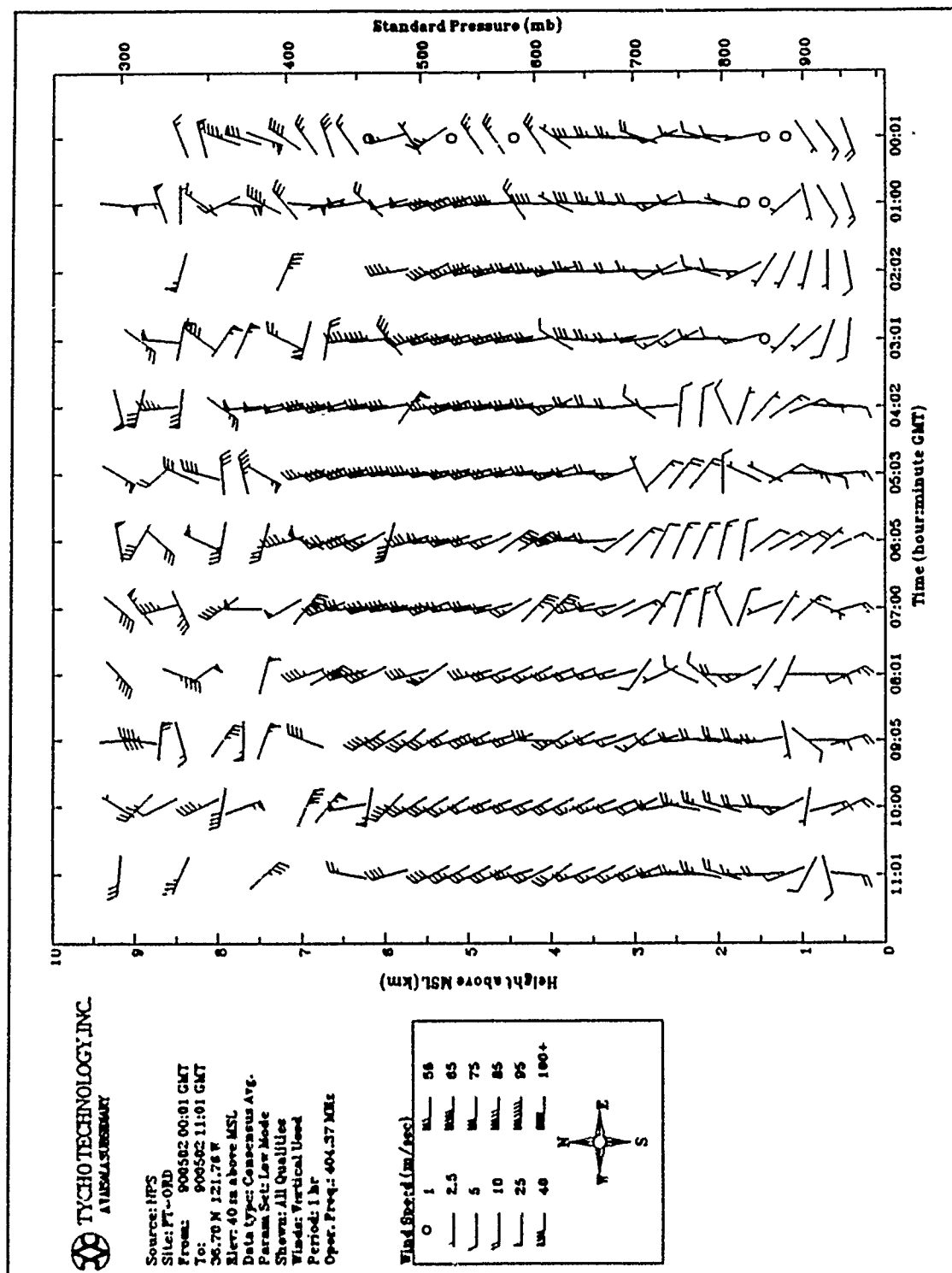


Fig. 41. NPS Radar Profiler Hourly-consensus Data for 02 May 1990

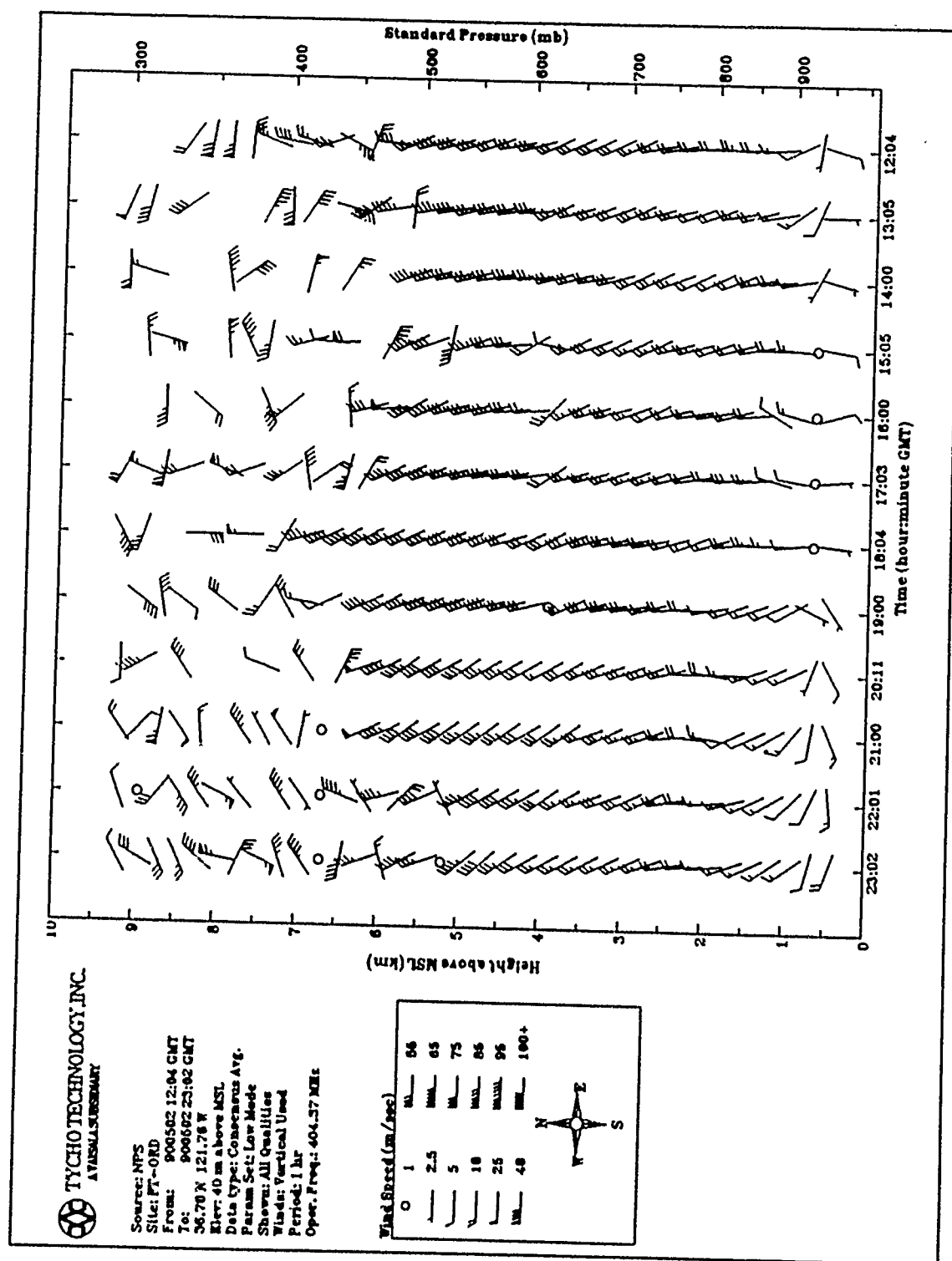


Fig. 42. NPS Radar Profiler Hourly-consensus Data for 02 May 1990

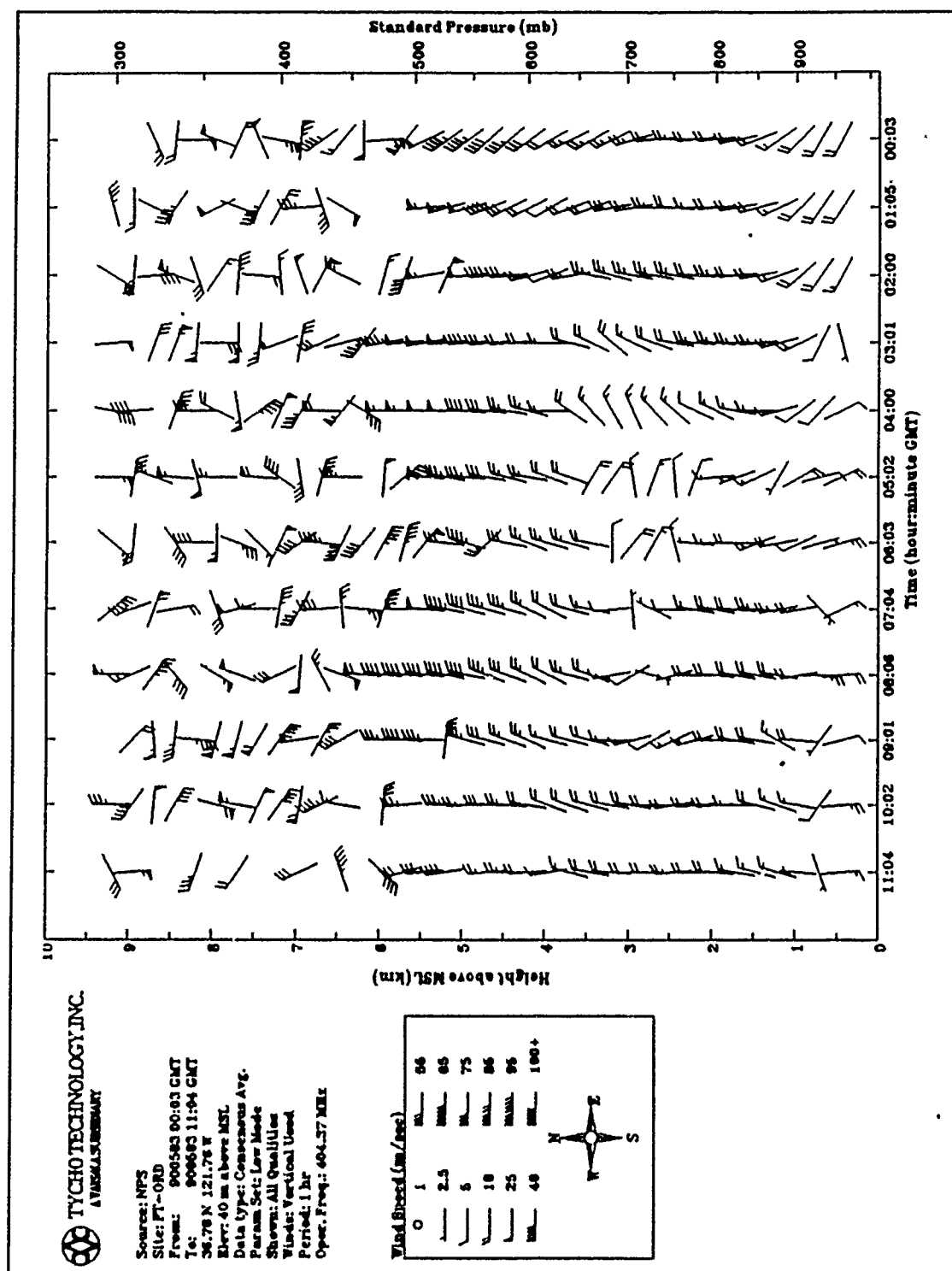


Fig. 43. NPS Radar Profiler Hourly-consensus Data for 03 May 1990

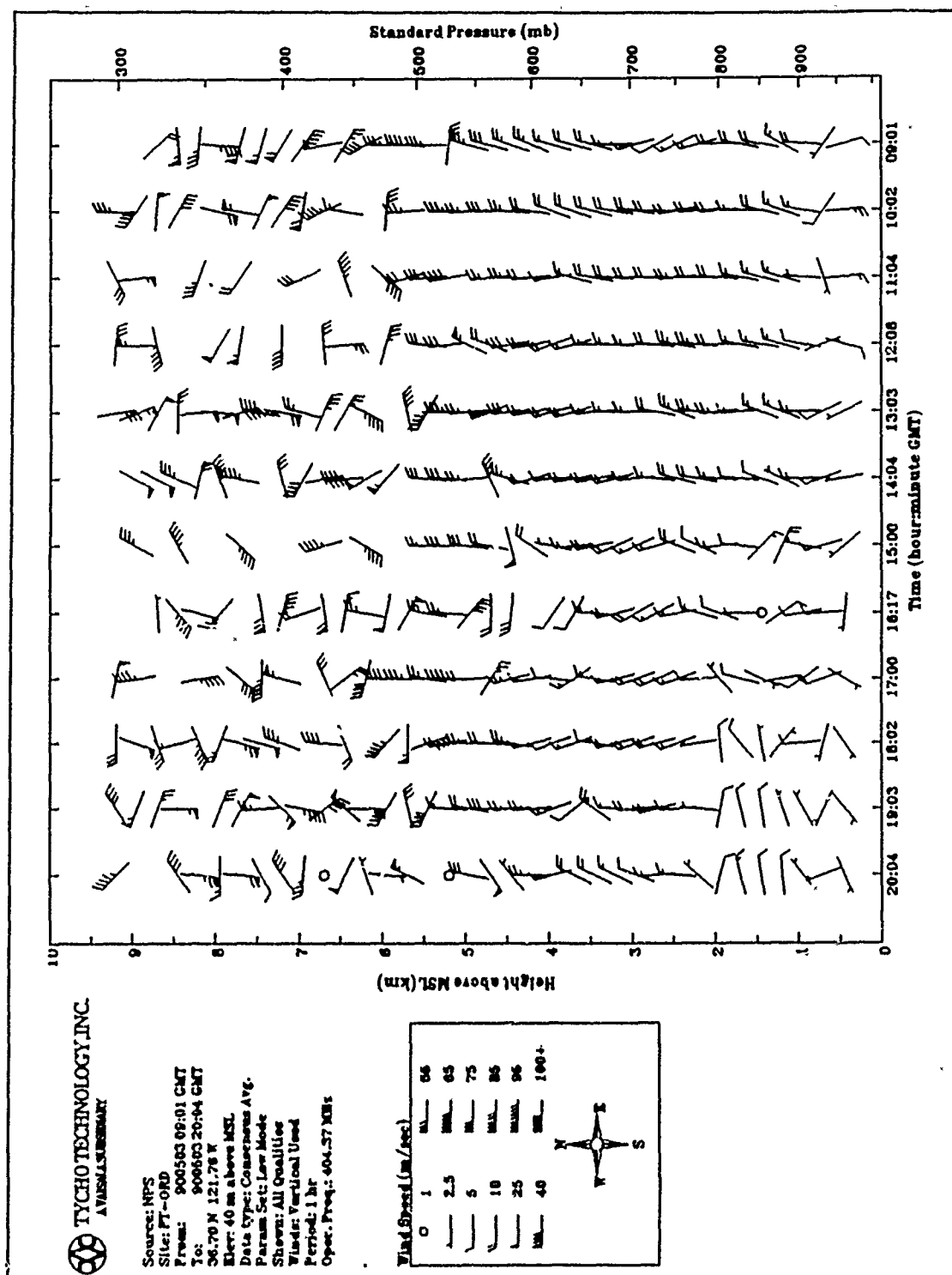


Fig. 44. NPS Radar Profiler Hourly-consensus Data for 03 May 1990

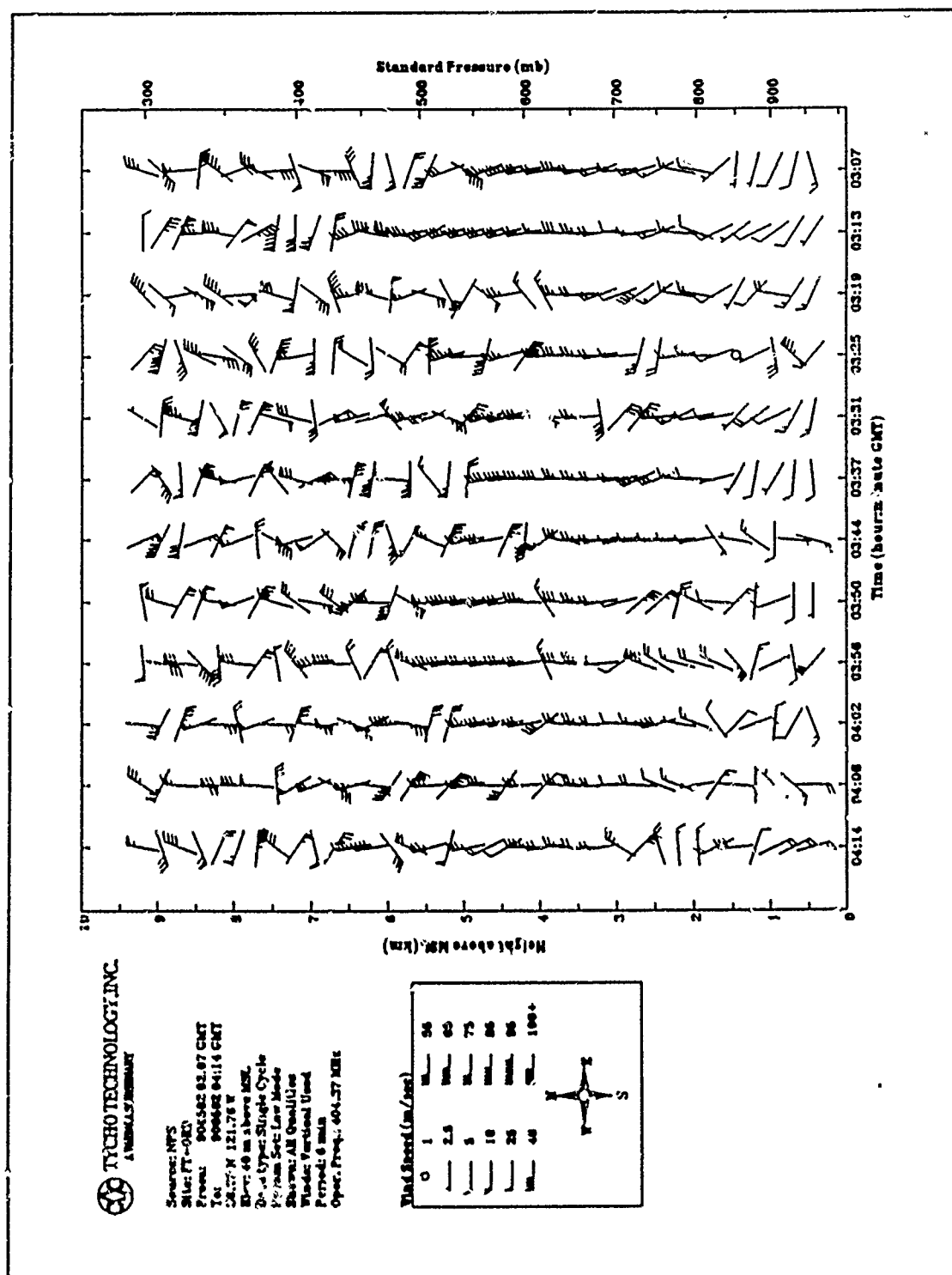


Fig. 45. NPS Radar Profiler Six-Minute Data for 02 May 1990

Table 4. SALINAS HOURLY SURFACE WEATHER OBSERVATIONS

YYMMDD/HHMM	STN	CLDL	CLDM	CLDH	VSBY	WTHR	PMSL	TMP	DWP	DDSSS	GST	ALTI
900502/0300	724917			250S	0.0			65	42	300	8	29.85
900502/0400	724917			200-S	20.0		1011.7	58	51	330	10	29.87
900502/0500	724917			200-S	15.0		1012.0	56	52	350	8	29.88
900502/0600	724917				0.0			55	52	340	9	29.88
900502/0700	724917				15.0		1012.0	54	50	320	7	29.88
900502/0800	724917				15.0		1011.7	52	50	0	0	29.87
900502/1000	724917				15.0		1011.3	48	47	0	0	29.86
900502/1100	724917				15.0		1011.3	46	46	0	0	29.86
900502/1200	724917	- 5S			3.0	F	1011.3	48	47	0	0	29.86
900502/1300	724917				5.0	F	1012.7	51	50	0	0	29.90
900502/1600	724917				15.0		1013.0	58	50	150	6	29.91
900502/1800	724917				20.0		1012.7	68	46	300	4	29.90
900502/1900	724917				20.0		1012.7	67	55	300	12	29.90
900502/2100	724917				12.0		1012.3	67	53	320	14	29.89
900502/2200	724917				12.0		1012.3	66	53	340	11	29.89
900502/2300	724917				12.0		1011.7	64	53	330	12	29.87
900503/0000	724917				12.0		1012.0	63	53	320	13	29.88
900503/0100	724917				12.0		1012.0	61	54	330	13	29.88
900503/0500	724917	7B			5.0	F	1014.1	53	53	340	7	29.94
900503/0600	724917	70			6.0	F	1014.1	54	53	310	9	29.94
900503/0800	724917	50			5.0	F	1014.4	53	53	320	7	29.95
900503/0900	724917	50			5.0	F	1014.7	53	53	310	6	29.96

V. CONCLUSIONS

This study determined the accuracy of the NPS profiler to be $3-4 \text{ m s}^{-1}$, i.e., the standard deviation values taken from the atmospheric layers which exceeded a .90 correlation coefficient in Chapter III. However, by obtaining a consensus with a 1 m s^{-1} velocity threshold, which was similar in all aspects to the manufacturer's consensus, suggests that the accuracy of the profiler is significantly better than $3-4 \text{ m s}^{-1}$. Thus there is an indication that the profiler does meet its contractual requirements. This disparity is easily explained by (1) the dislocation of sensors, (2) the recent evidence (Thomson and Williams 1990) that rawinsondes are less accurate than radar profilers, and (3) the extremely small data set available for this study.

Reliable data was found within the six-minute profiles, it is not as random as it first appears. The parameter thresholds determined in Chapter IV are very effective for identifying bad data and can be useful in improving the individual six-minute profiles. The thresholds also can be used individually to isolate certain physical characteristics of the air column such as turbulence. And when all the data is assimilated, a good picture of what is occurring in the PBL (up to 6 km) is obtained. Ironically, even the presence of bad data has a meaning, such as the presence of a dry, subsiding air mass. It is then not enough to say the data is bad, it must be understood why the data is bad.

Although the data quality checks which were developed to clarify the six-minute data were very successful, the presumption that they would also improve the hourly consensus was not proven with as much success; the hourly consensus was not dramatically affected by the improvement of six-minute data.

Despite the large vertical spatial resolution (250 to 1000 m) in the radar data, the overall radar performance appears to be very good. A great deal of detail can be drawn from the wind profiles. It has been shown that high frequency meteorological wave phenomena can be detected with the six-minute data, but other fluctuations in the local meteorology can also be detected. The six-minute data can accurately depict the dramatic and sudden changes in the land/sea breeze circulation. Furthermore, there are complex topographic interactions which may be understood by analyzing the six-minute data. The high-temporal resolution and accuracy of the profiler in determining three dimensional meteorology is certainly an exciting addition to the NPS Meteorology curriculum.

VI. RECOMMENDATIONS

This study has been able to demonstrate the quality and usefulness of the profiler data during its early period of operation. However, there is considerable potential for future and more complete meteorological studies. The following list of recommendations are things that may help check the quality of the data and better define the detailed meteorology sampled by the profiler.

A. MEASUREMENT VALIDATION AND DATA QUALITY IMPROVEMENT

- Improve the manufacturer's algorithm for spectral averaging based on local meteorology.
- Allot a rawinsonde system dedicated to work with the profiler.
- As Thomson (1990) indicates, the uncertainty in profiler-derived wind speeds and direction is clearly significantly less than the natural variability of the wind. Rather than using rawinsondes which are highly prone to sampling errors, another radar profiler, LIDAR, or SODAR should be used to accurately gage NPS profiler performance--not the rawinsonde system.
- Investigate techniques such as those listed in Appendix D which can improve data quality outside the hourly-profiles.

B. ACADEMIC RESEARCH

- Use a 50 MHz profiler for comparison with the NPS profiler. It should detect winds higher in the atmosphere.
- Investigate the possibility of acquiring a complete network of at least three profilers, either through outright purchasing or coordination with other agencies or academic institutions. For example, San Jose State University might be inter-

ested in purchasing a profiler, placing it within the Monterey Bay local, and then recover the data remotely via telephone lines.

- Add the NPS 2 kHz SODAR to the operational data base.
- Coordinate 5 kHz SODAR operations with the Physics Dept.
- Pursue implementation of the manufacturer's software regarding C_N^2 calculations.
- Investigate the possibility of determining a Power to Humidity algorithm.
- Rigorously employ the Radio-Acoustic Sounding System (RASS) modification package within the profiler.
- Make all remote connections to automate delivery and storage of the profiler data, especially the capability to upload data into the NPS IDEA Laboratory.
- Get more students involved. Draw real-time information into the classroom.
- Conduct a detailed study of land/sea breeze and topography interaction along the Monterey Bay.
- Incorporate real-time ground- and space-based remote sensing data, such as wind profiles from the NPS Doppler wind profiler, in as many of the meteorology courses as is possible.

APPENDIX A. EQUIPMENT CONFIGURATION

A. WIND PROFILER

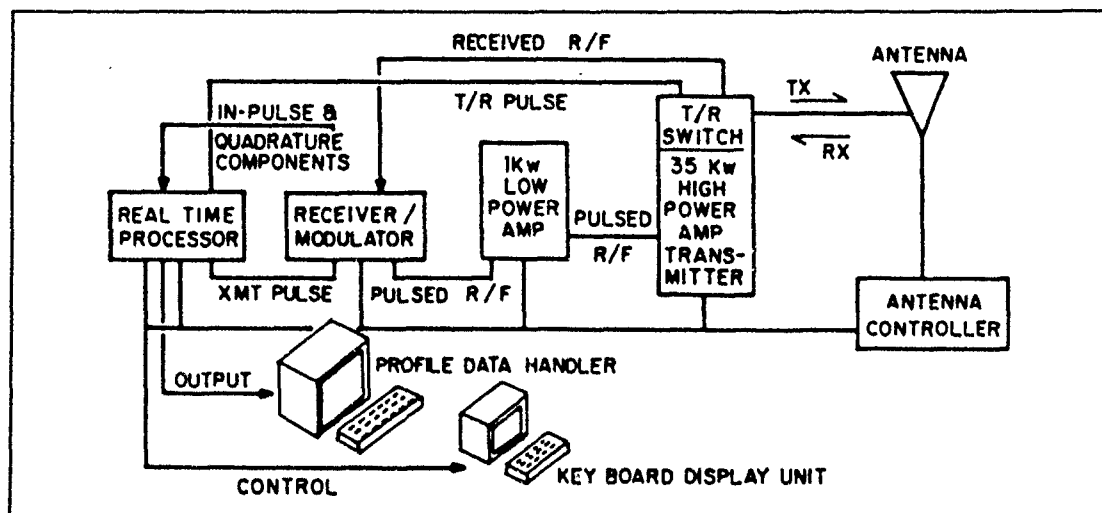


Fig. A-1. Functional Diagram of Wind Profiler

The wind profiler consists of a two-stage transmitter, antenna, receiver, transmit/receive (T/R) switch, and processor with its firmware. Fig A-1 illustrates the basic operation of a Tycho-engineered wind profiler. On command from the Real-Time Processor (RTP) the antenna controller sets up the proper phasing for the desired antenna beam position (i.e., vertical, 15° southeast, or 15° southwest). The T/R pulse sets up the T/R switch for transmit mode. The RTP sends a prompt signal (or pulse) to the receiver/modulator, which produces a pulsed RF signal. This is then disconnected from the antenna during the transmit cycle to prevent overloading. The system is then set to the "receive" configuration. The receiver is reconnected and the T/R switch directs the weak return signal from the antenna to the receiver. The receiver amplifies the signal and extracts the in-phase and quadrature (or sine and cosine) phase components from which the radial velocity is derived. Filtered outputs are sent to the RTP, which performs the various processing steps necessary to produce the radial wind components, noise levels, signal power strength, and velocity variance. The Profiler Data Handler (PDH) is a VAX 3100 smart terminal which processes these parameters to derive time-height wind profiles, C_z profiles, wind speed and direction profiles, radial velocity variance versus height, and signal-to-noise (S/N) profiles. The Keyboard Display Unit

(KDU) has four functions: (1) it provides the ability to edit operating parameters, (2) displays individual mode spectra, (3) monitors profiler operation, and (4) controls profiler operation.

B. RAWINSONDE

The upper air profiling system utilized for this analysis integrated the Vaisala-DigiCORA receiver-processor with Vaisala RS80-series rawinsondes. The specific software version installed within the DigiCORA system was the Corex version. Measurements are based on the use of a free-ascent balloon rawinsonde. The rawinsonde, or "sonde", transmits data to the station at 402 MHz. Refer to Fig. A-2. Pressure, temperature, and humidity are measured by sensors in the sonde. Each of the capacitive sensors controls the frequency of an oscillator through an electronic switch. Relationship between the frequency and corresponding parameter value is established in the calibration process prior to launch. (Specifications of the individual sensors are provided in Fig. A-3. The location of the sonde is determined by means of a third generation Navaid (Omega + Very Low Frequency (VLF))-based windfinding program called "multifrequency composite VLF". In the composite solution more than one frequency from each Omega transmitter and one frequency of the USSR VLF network are used. Navaid signals are relayed to the ground station for processing and for wind profile computation. Briefly, the signals are processed in a correlation processor to derive their relative phases from which the sonde's movements can be calculated. Wind speed and direction over the range of 0 to 180 m s^{-1} is computed with an accuracy of 0.5 m s^{-1} , regardless of balloon distance from the ground station.

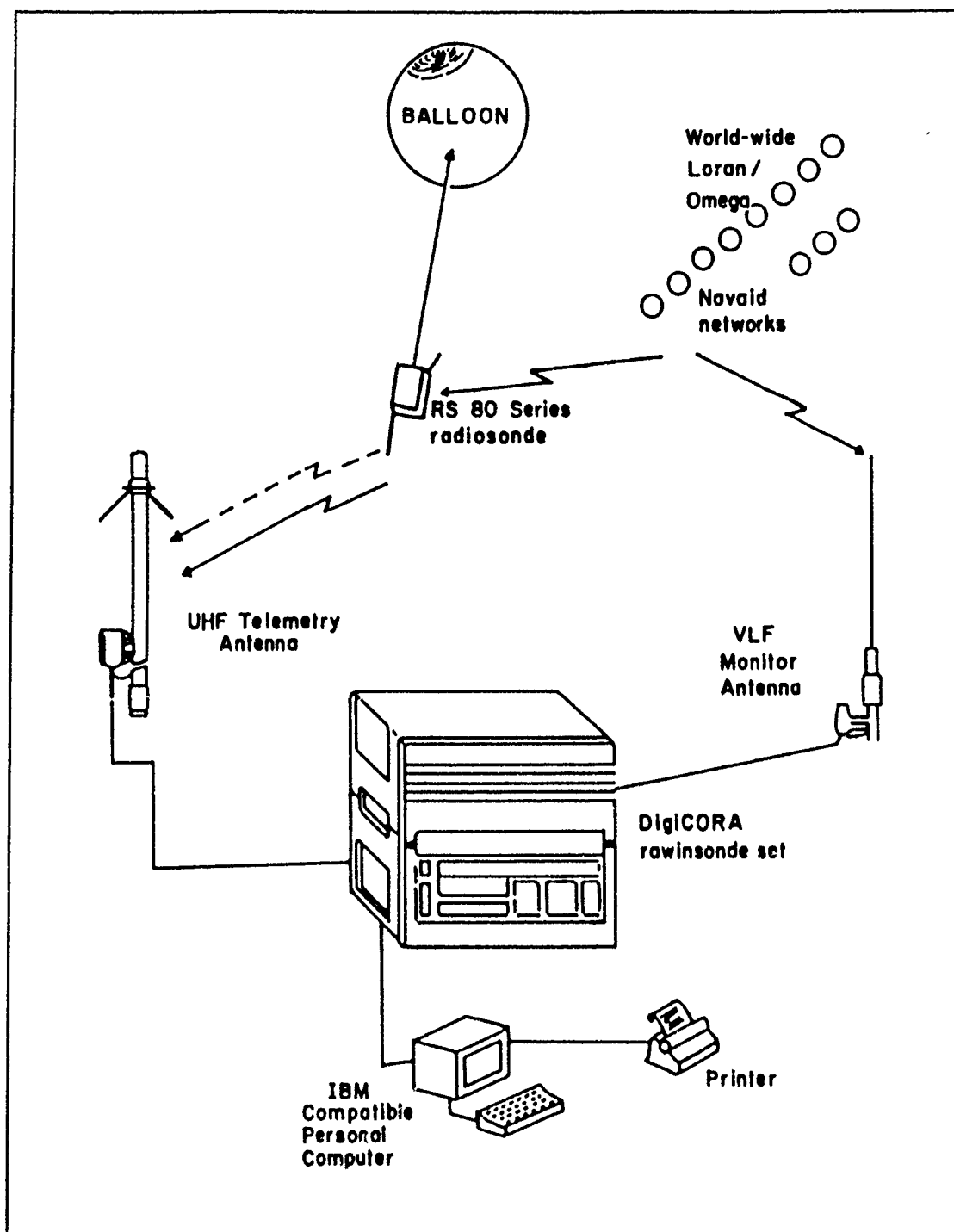


Fig. A-2. Vaisala DigiCORA Upper Air Sounding System: (Source: Vaisala DigiCORA Repair Manual)

Table A-1. RAWINSONDE METEOROLOGICAL SENSOR TECHNICAL DATA (from Vaisala Corporation)

<i>Pressure</i>	
Type	Capacitive Aneroid
Measuring Range	1060 hPa to 3 hPa (mb)
Resolution	0.1 hPa
Accuracy	0.5 hPa
<i>Temperature</i>	
Sensor Type	Capacitive Bead
Measuring Range	+ 60°C to -90°C
Resolution	0.1°C
Accuracy	0.2°C
<i>Humidity</i>	
Sensor Type	HUMICAP® Thin Film Capacitor
Measuring Range	0 to 100% RH
Resolution	1% RH
Lag	1 s (6 m s ⁻¹ flow at 1000 hPa, +20°C)
Accuracy	2% RH

APPENDIX B. DERIVATION OF THE RADAR EQUATION FOR CLEAR AIR PROFILERS

The radar equation relates the received power (echo power) to radar parameters and target parameters. If the radiating source radiates isotropically, that is, equally in all directions, the power density (P_r , power per unit volume) at range R from the radiator is

$$P_r = \frac{P_t}{4\pi R^2}, \quad (B-1)$$

where P_t is the peak transmitted power. Radar antennas do not radiate isotropically however, but rather transmit the energy in a beam. The energy density actually received at any given range and direction relative to isotropic, is called the gain (G) or

$$G = \frac{P_{\text{Beam}}}{P_{\text{Isotropic}}}. \quad (B-2)$$

If the target scatters isotropically, the power intercepted by the receiver is

$$P_r = \alpha_t P_t \frac{G_t}{4} \pi R_t^2 \sigma \frac{A_r}{4\pi R_R^2}, \quad (B-3)$$

where σ is the back-scatter cross section of the target, and A_r is the effective antenna aperture, and α is the transmitter antenna efficiency.

The widths of the main beam in the north-south and east-west directions, θ and ϕ respectively, are generally specified by the widths at the half-power points. These widths depend mostly upon the size of the antenna and wavelength of the radiation, although the shape of the antenna and power distribution across the antenna also influence these widths. To a good approximation

$$\sin \theta = \frac{\lambda}{L_1}, \quad (B-4a)$$

$$\sin \phi = \frac{\lambda}{L_2}, \quad (B-4b)$$

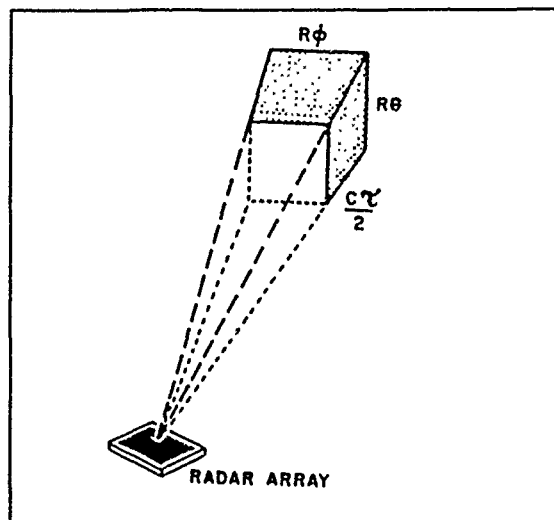


Fig. B-1. Illustration of Geometry for Beam Volume Calculations

where L_1 and L_2 are the linear dimensions of the antenna in the directions that correspond to θ and ϕ , and λ is the transmitted wavelength. For narrow beams, the sine of the angle can be replaced by the angle itself:

$$\theta = \frac{\lambda}{L_1}, \text{ and} \quad (B-5a)$$

$$\phi = \frac{\lambda}{L_2}. \quad (B-5b)$$

The width of the beam between the first nulls (the nulls between the main beam and sidelobes on either side of the main beam) is about twice these half-widths. The solid angle corresponding to these half-widths (Ω) using Eqs. (B-5a) and (B-5b) is

$$\Omega = \theta\phi = \frac{\lambda^2}{L_1 L_2}. \quad (B-6)$$

The area of a rectangular planar array (A_p) by substitution into Eq. (B-6) is the same as the physical area:

$$A = L_1 L_2 = \frac{\lambda^2}{\Omega}. \quad (B-7)$$

But if the power distribution across the antenna is tapered, the effective area will be slightly different from this. In general, the effective aperture is smaller than the physical aperture, the ratio being called the antenna efficiency (α):

$$\alpha = \frac{A_e}{A}, \text{ or } A_e = \alpha A. \quad (B-8)$$

The antenna gain can be related to the aperture by making the simplifying approximation that the actual beam pattern can be replaced by a rectangular beam pattern that has a given gain G over a width equal to the half-width and zero everywhere else. In this case

$$G = \frac{\frac{P_t}{\Omega R^2}}{\frac{P_T}{4\pi R^2}} = \frac{4\pi}{\Omega}; \quad (B-9)$$

but by substituting Eq. (B-7) into (B-9)

$$G = \frac{4\pi A_e}{\lambda^2}. \quad (B-10)$$

Substituting Eq. (B-10) into Eq. (B-3) returned power becomes

$$P_r = P_t G_t A_r \alpha_r \alpha_t \frac{\sigma}{16\pi^2 R_t^2 R_r^2}. \quad (B-11)$$

but, $\alpha_t = \alpha_r = \alpha$, $R_t = R_r = R$, $G_t = G_r = G$, and $A_t = A_r = A$, because the antenna is the same hardware used for the transmitter and receiver, therefore

$$P_r = P_t G A \alpha^2 \frac{\sigma}{16\pi^2 R^4}. \quad (B-12)$$

For a distributed target such as encountered in meteorology, we must sum over all the scatterers in the sample volume. This sample volume is defined by the radar range resolution, $\Delta R = c\tau/2$ (where τ is the pulse length, and c is the propagation speed of radio energy), and by the half-widths of the radar beam θ and ϕ :

$$V = \frac{c\tau}{2} (R\theta)(R\phi) = \frac{c\tau R^2 \lambda^2}{2A} \quad (B-13)$$

Assume the scatters don't "shadow" each other and that they don't have appreciable absorption. Then, the radar reflectivity is the sum of all the σ 's in the volume divided by the volume:

$$\eta = \frac{\sum \sigma}{V}; \text{ or } \sigma = \eta V. \quad (B-14)$$

By substitution of Eq. (B-14) into Eq. (B-12) the radar equation becomes

$$P_r = P_t G A \alpha^2 \frac{\eta V}{16\pi^2 R^4}. \quad (B-15)$$

Utilizing Eq. (B-10), by substitution into Eq. (B-15)

$$P_r = P_t A^2 \frac{4\pi}{\lambda^2} \alpha^2 \frac{\eta V}{16\pi^2 R^4}. \quad (B-16)$$

Utilizing Eq. (B-13), Eq. (B-16) becomes

$$P_r = P_t A^2 \frac{4\pi}{\lambda^2} \alpha^2 \eta \frac{\frac{c\tau R^2 \lambda^2}{2A}}{16\pi^2 R^4} = P_t A \alpha^2 c\tau \frac{\eta}{8\pi R^2}. \quad (B-17)$$

The above assumption can be made more accurate by using a more appropriate form of the gain equation. If a Gaussian beam shape is used, instead of a rectangular shape, the fact that the edges of the sample volume are not illuminated as powerfully as the central portion can be compensated by adding a shape factor:

$$P_r = [P_t A^2 \alpha^2 c\tau \frac{\eta}{8\pi R^2}] \times [ShapeFactor]. \quad (B-18)$$

For a planar array according to Gossard and Strauch (1983) the shape factor is $4/9(\lambda^2/A)$. Substituting the shape factor into Eq. (B-18) the radar equation evolves into

$$P_r = P_t A \alpha^2 c\tau \frac{\eta}{18\pi R^2}. \quad (B-19)$$

Eq. (B-19) is appropriate for the scattered signal. The radar is, of course, also sensitive to noise. Noise comes from a variety of sources, the main ones being system noise (also called Johnson noise) and cosmic noise. System noise can be controlled somewhat by

the design of the radar but it can never be completely eliminated. Noise power is typically expressed in terms of the equivalent temperature that a blackbody would emit at the given frequency to account for the power observed. The noise power (P_N) is

$$P_N = kB(\alpha T_C + T_S), \quad (B - 20)$$

where k is Boltzmann's constant, B is the receiver bandwidth (which is designed to match the transmitted bandwidth, approximately $1/\tau$ at the half-power points), T_C is the cosmic noise temperature, and T_S is the system noise (also called the receiver noise). The factor α arises because inefficiencies in the system affect the noise power received as well as the signal power:

$$P_r = P_t A_e \alpha^2 c \tau^2 \frac{\eta}{8\pi R^2 k(\alpha T_C + T_S)}. \quad (B - 21)$$

This is a basic equation used by the Tycho profiler and is consistent with research done by Röttger and Larsen (1990). Finally, the radar constants are taken out of the equation and grouped together for ease, as used in the body of the study:

$$P_r = \frac{\alpha^2 c}{8\pi k(\alpha T_C + T_S)} P_t A_e \tau^2 \frac{\eta}{R^2} = K P_t A_e \tau^2 \frac{\eta}{R^2}, \quad (B - 22)$$

where K is a "radar constant".

APPENDIX C. RADAR WIND PROFILER TRIGONOMETRY

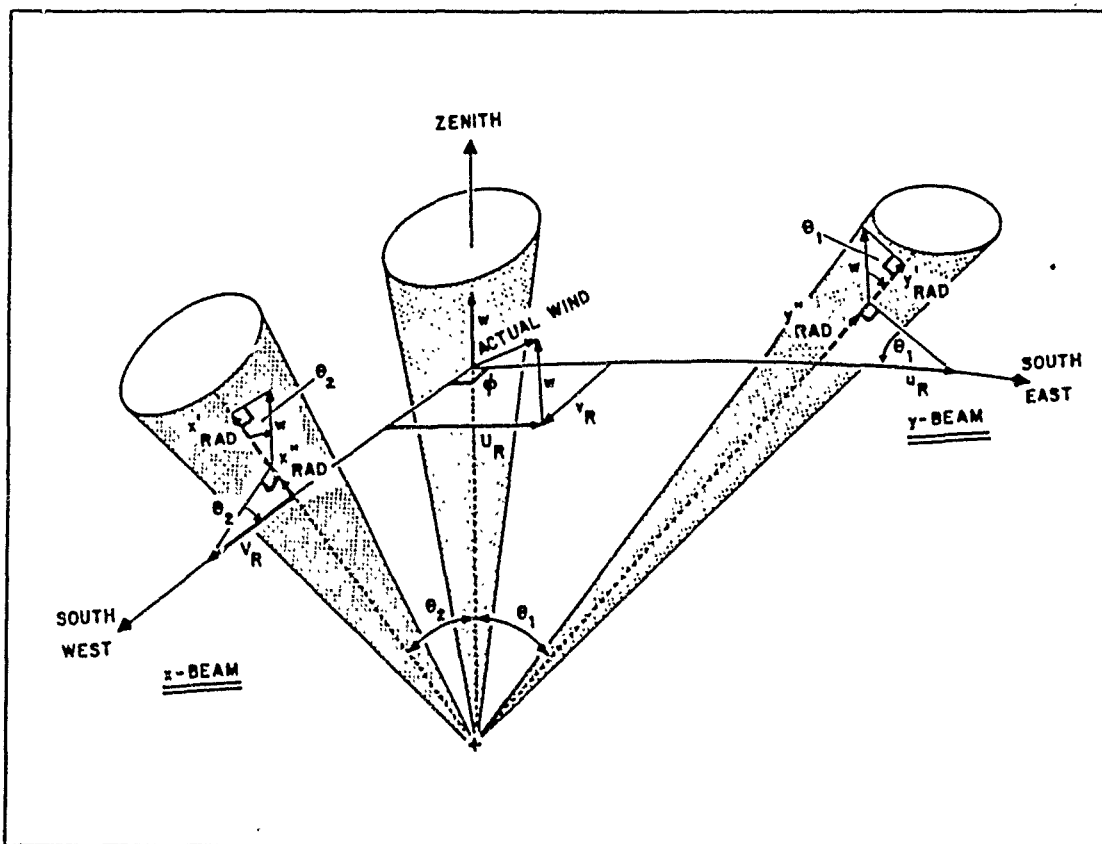


Fig. C-1. Horizontal Velocity Calculation from the Three Radial Velocities

Figure C-1 illustrates how the horizontal wind components can be derived from the profiler-measured radial velocities. Fig. C-1 illustrates three beams which are utilized in either the low- or high-power mode. The "zenith", or vertical beam, measures the w -component of the wind directly. The radial velocities of the other two off-vertical beams, X_{RAD} and Y_{RAD} , have not only a vertical component, but also horizontal components related by the following equations:

$$\begin{aligned} X_{RAD} &= X'_{RAD} + X''_{RAD} & Y_{RAD} &= Y'_{RAD} + Y''_{RAD} \\ X_{RAD} &= -(-V_x \sin \theta_2 + w \cos \theta_2) & Y_{RAD} &= -(w \cos \theta_1 + u_R \sin \theta_1) \end{aligned}$$

Note: The negative sign compensates for the scheme depicting velocities toward the radar as positive. If w , X_{RAD} , and Y_{RAD} (the three radial velocities processed by the profiler) are known; then

$$u_R = (-Y_{RAD} - w \cos \theta_1) / \sin \theta_1; \text{ and}$$

$$v_R = -(-X_{RAD} - w \cos \theta_2) / \sin \theta_2$$

Note: A negative sign must be applied to v_R , to compensate for the usual horizontal cartesian coordinate system, i.e., v to the north. θ_1 and θ_2 are the angles which the off-vertical beams are offset from the vertical. These angles are currently set at 15° . u_R is the Eastward wind component computed from the radial velocities, and v_R is the Northward wind component computed from the profiler radial velocities.

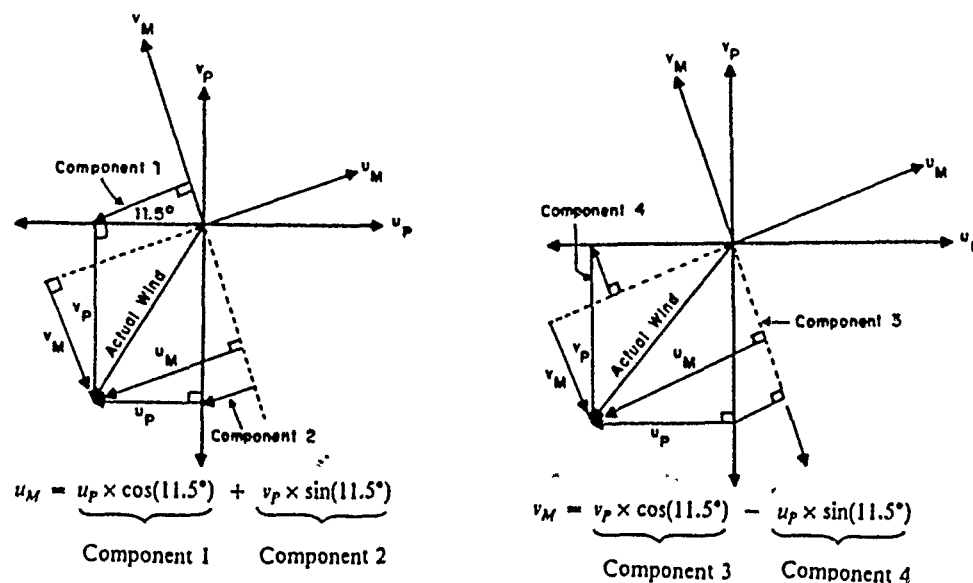


Fig. C-2. Trigonometry Relating Coordinate Axes in the Horizontal Plane

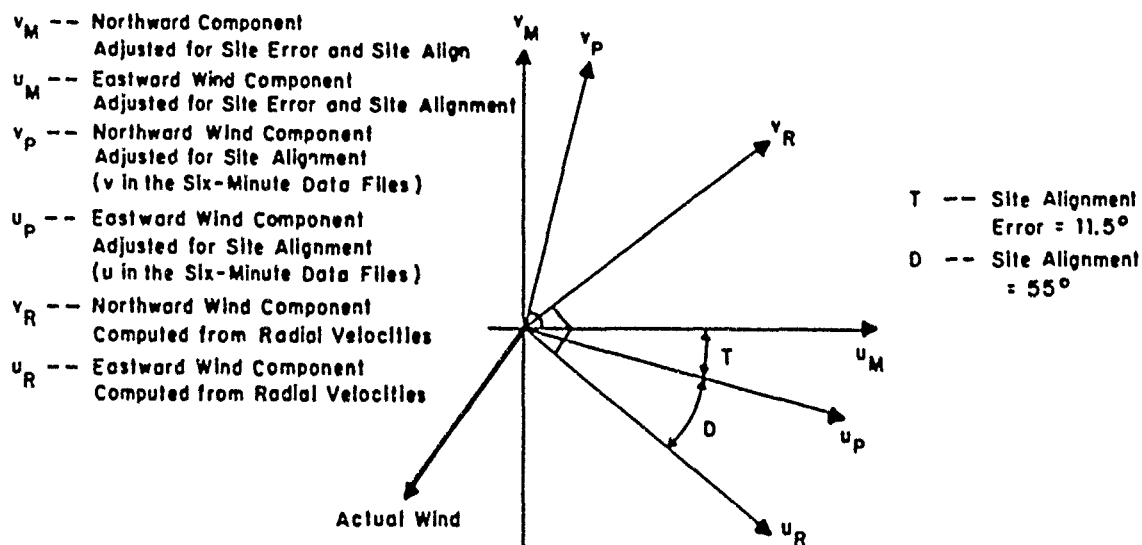


Fig. C-3. Trigonometry of Axis Translation for Site Correction

Note: Correction for site alignment to files before 03 May 1990 2200 (UTC) must be applied. After 03 May 1990 2200 (UTC), the elevation and orientation are correct--no correction needs to be applied.

APPENDIX D. CONSENSUS TECHNIQUES

Because we know that spurious data can enter the profiler system, much more readily than a direct-measuring system, automated quality control (QC) procedures have been developed. This appendix contains excerpts from Brewster (1989). These procedures take advantage of the consistency of the winds in time and height (on the scale of sample separation, 250 meters in height and 6 minutes or 1 hour in time). The QC algorithms for the profiler data calculate an expected value to the measured value. The expected value is typically a function of the measurements surrounding the datum in time and space. It may also depend on some sort of "first guess" provided by a forecast model or expressed as a function of the surrounding data. If the difference between the expected and measured values exceeds a threshold, then the datum is considered suspect. Various procedures may be followed to determine if the datum arises from a plausible but extreme meteorological event or if the large difference is caused by a bad datum among those used to calculate the expected value. In this appendix several techniques that can be applied to wind profiler data are described--first that which is developed for use by the Tycho profiler, then some others that can be applied in-house by forecasters and are included for reference as techniques to apply in future studies using the NPS profiler.

For wind profiler data distributed to data networks in the future the QC must be done in real time, that is, the data for the current hour must be checked before data from the next hour arrive. Estimating measured values is more difficult because the data are unevenly distributed in time--plentiful data from past times, but none from future times. For some applications, more precise "two-sided" quality control, done after future data have arrived, is not only possible but desirable. Two factors merit consideration: 1) how long after the data collection can one wait before running the QC, and 2) how sensitive is the application to data errors.

A. CONSENSUS AVERAGING

The 1-hour wind averages produced at NPS are derived from the 6-minute radial velocity samples by a technique known as consensus averaging. Primarily an averaging process, this technique also has built-in QC. As suggested by the name, not all the data are averaged, but only those that mutually agree within a threshold. A 2.0 m s^{-1} window

is used for the velocity. We review the effect of this technique by considering these ten 6-minute radial velocity samples:

3.3 4.6 20.9 2.8 3.6 4.1 -6.8 3.4 4.0 22.2 ($m s^{-1}$)

The average of all samples is $6.2 m s^{-1}$. Looking at the individual points you can see that $6.2 m s^{-1}$ does not at all represent the typical sample value during the hour; it has been severely contaminated by three outliers. Now if we collect with each sample all other samples agreeing within $\pm 1.5 m s^{-1}$, that is falling within a $3.0 m s^{-1}$ window, we get the groups from Table D-1. The greatest number of samples in a group is seven, a tie among five groups. The group of seven coming latest in the hour (indicated by the arrow) is then selected for the consensus; in this case all five groups of seven are identical so the position within the hour doesn't matter. The consensus average is the average of that group, $3.7 m s^{-1}$, which almost anyone would agree is representative of the entire sample set.

Table D-1. FUNCTIONAL CONSENSUS PROCESS: Example of individual sample cross-comparisons involved with consensus process.

sample	samples within window						
3.3:	2.8	3.3	3.4	3.6	4.0	4.1	4.6
4.6:	3.3	3.4	3.6	4.0	4.1	4.6	
20.9:	20.9	22.2					
2.8:	2.8	3.3	3.4	3.6	4.0	4.1	
3.6:	2.8	3.3	3.4	3.6	4.0	4.1	4.6
4.1:	2.8	3.3	3.4	3.6	4.0	4.1	4.6
-6.8:	-6.8						
3.4:	2.8	3.3	3.4	3.6	4.0	4.1	4.6
4.0:	2.8	3.3	3.4	3.6	4.0	4.1	4.6 ←
22.2:	20.9	22.2					

In practice, mathematical shortcuts speed calculation of the average value that has the most samples lying within the threshold window. If no group has at least four

members to form a consensus (as might be found if the data are made up of random values), then the average value is reported as zero.

Consensus averaging handles isolated spikes in the data quite well, as in the example. It also handles cases in which the returned atmospheric signal is too weak to be detected. Then, the data samples are nearly random, and a missing value will be reported.

B. COMBINED MEDIAN FILTER AND SHEAR CHECK

As the name suggests, this routine consists of two checks applied sequentially to hourly averaged data. In the median check (see Fig. D-1) data are gathered from adjacent hours (the current hour and the last two available hours) and adjacent levels. The median (the reported value of which half the samples are greater and half are less) of this collection of data is then computed for the two horizontal wind components. If the difference between the datum and median is greater than a threshold, the median is recalculated using only those data from the current hour and the last hour. This is done to preserve data in the event of a strong wind shift with time as might be found in a dramatic trough passage. Data are flagged bad if the observed datum and the recalculated median also differ by more than the threshold. The threshold value depends on the height of the datum (greater thresholds at greater altitudes), the wind speed (greater thresholds for high speeds), and the time difference between the datum and the data collected for the median computation (greater threshold when there are missing data in previous hours). In the current implementation, the median check is quite loose; it is designed to flag the most widely varying data but may pass along a substantial number of spurious data. The philosophy is to discard the implausible values before the shear check and to leave the more difficult decisions to that second step.

The vertical consistency check uses a gate-to-gate shear threshold, which is a function of height, distance between the observations, wind speed, and the difference in wind direction (greater shear is allowed if the wind direction is unchanging). A typical threshold is about 20 m s^{-1} per kilometer or about 13 kts per thousand feet.

If the magnitude of the vector shear between the first and second gates exceeds the threshold, the shear between the second and third gates is checked. If the second shear is nearly the same magnitude as the first and in the opposite direction, the data in the second gate are flagged bad (both horizontal components). This situation is illustrated in Fig. D-2. The magnitude of the shear between the first and second gates, 22.6 kt, is excessive, thus prompting a check on the shear between the second and third gates (27.5

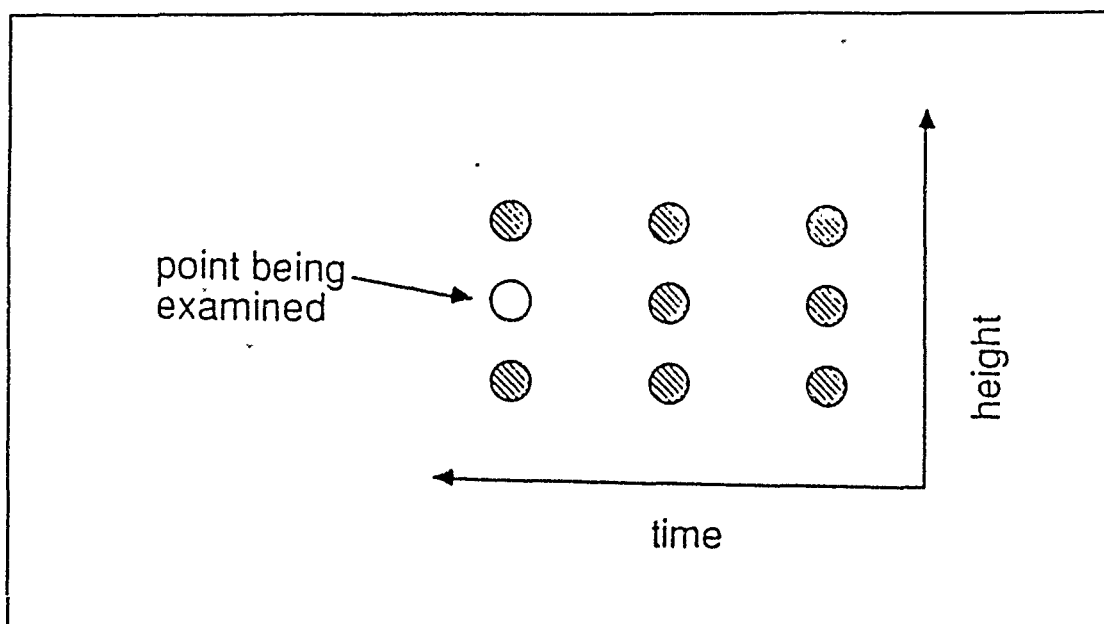


Fig. D-1. Data Points from which Median is calculated in the Median Check

kt). The two shears are comparable in magnitude and nearly opposite in direction (the components have opposite signs). Thus the light northwest wind in the second gate is flagged.

If the wind in the third gate tends to continue the shear between the first and second gates, a straight line is plotted through the u - and v -components of winds in the first and fourth gates. If both components in the second and third gates lie reasonably close to their respective lines, they are accepted as valid measurements. This is the condition shown in Fig. D-2b, where the sample winds imply strong shear across a frontal boundary. On the other hand, if either component in the second and third gates lies far from the line, both winds are flagged as bad. Fig. D-2c illustrates the case of two spurious winds between two valid winds. The line for the u -components lies along the horizontal axis. Although the middle two u -components lie close to the line for u , the middle two v -components lie far from the line for v . Thus the middle two winds are flagged. Note that the scale for u and v in Figs. D-2b and D-2c has been held constant to facilitate comparisons.

The practical result of these tests is that a layer of winds containing four or five measurements that pass the median check and corroborate each other will be retained even if there is substantial shear at the layer interfaces. Moreover, two adjacent, spurious winds supporting each other are likely to be flagged correctly as bad, as in the above

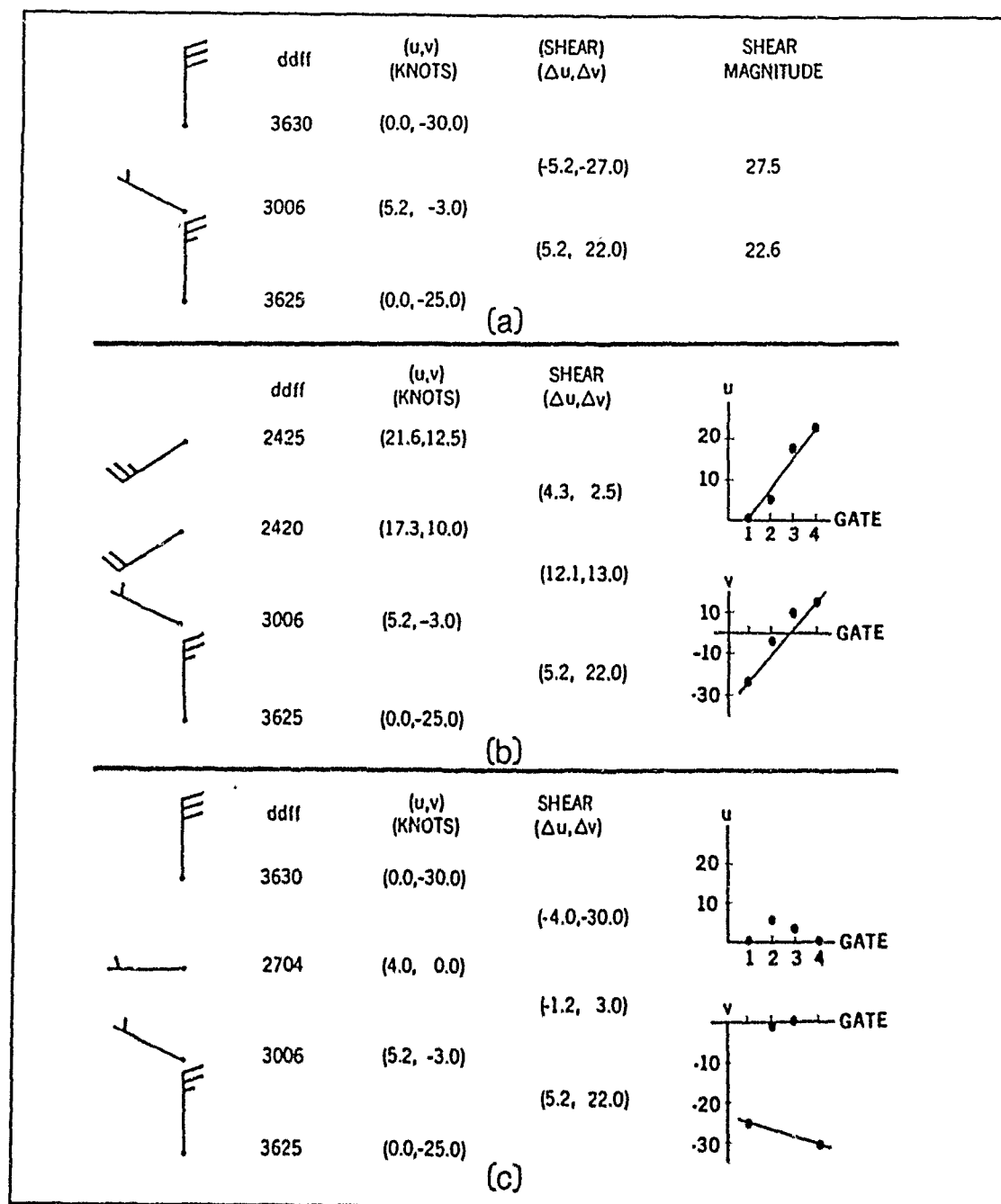


Fig. D-2. Three examples of the vertical consistency check.: (a) A bad wind between two good winds, (b) good winds with strong shear, and (c) bad winds in gates 2 and 3.

example; three such winds may not be. Conversely, if a layer of anomalous but valid winds is only sampled by two or three gates, those wind observations may be erroneously rejected.

The vertical consistency check is applied once to the low mode data and then to the entire profile, high and low modes meshed together. Checking in each case begins with the lowest gate and proceeds upward. Special processing with linear extrapolation of neighboring data is used at the lowest and highest gates in the profile, should large shear be indicated there.

To re-emphasize, the most powerful check in the system is the vertical consistency check. Substantial changes from one hour to the next are generally allowed to pass through the median check but are rejected later if there is insufficient continuity in the wind shift with height.

C. OPTIMAL INTERPOLATION

Statistical objective analysis, also known as Optimal Interpolation (OI), is widely used for analysis of meteorological variables on quasi-horizontal surfaces. In fact, OI is used today at many national weather centers, including the National Meteorological Center (NMC) and Fleet Numerical Oceanography Center (FNOC), for model initial analysis. This method utilizes statistical properties of the observations and the background field (also called a "first guess"). The background is usually a model forecast but climatological averages or persistence can serve the same purpose. The OI analysis takes into account the positions of the observations relative to each other and relative to the analysis point; it has an extrapolative property that aids analyses near data edges.

Optimal interpolation can be used for quality control. The datum under scrutiny is compared with a value analyzed at the same location by means of OI. Surrounding observations (but not the central one) and the background field contribute to the analyzed value. If the difference between the analyzed and observed value exceeds some threshold, the datum requires further testing. Since the OI method provides an estimate of the analysis error, the threshold can be specified as a function of the analysis error. This allows for more variation when observations are sparse or distant from the datum in question and less variation when the observations are dense or located very close to the datum.

Large discrepancies between the observed and analyzed value may arise either because the subject observation is erroneous or because one of the observations contributing to the analysis is erroneous. To find out which is true, the data are re-analyzed

several times, removing one of the surrounding observations each time to see if that produces agreement (Fig. 3). The removed observation is returned for subsequent re-analyses so that only one observation is absent for each re-analysis. If no agreement is found for any re-analysis, the datum being examined is flagged. Should the removal of one of the observations produce agreement, the removed observation is flagged as suspect and is not used in any subsequent QC analysis. Suspect flags are internal to the QC program and are generally not part of the QC output. Typically, a datum is flagged only when it is the subject datum.

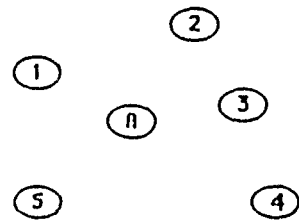
This technique just described can be used to check data in a time-height cross-section as well as on the horizontal surfaces for which it was originally designed. The correlation statistics must then be specified in time-height space. OI time-height quality control of profiler data in real time presents a special problem. Because there is an attempt to always examine the latest hour, the analyses are not centered in time (i.e., it is always analyzing on the edge of the time-height domain). A second, often vexing problem is that spurious winds are not always isolated--repeated errors in a given beam, extending over several gates, can cause the re-analysis technique to fail.

The majority of cases can be handled properly if data selection for each analysis is done to minimize the possibility of multiple bad data points being included. An OI QC algorithm developed at PROFS makes two passes through the data with the flagging threshold decreasing on the second pass. In the first pass, data are checked in sequence from the lowest gate to the highest. The two nearest data points are collected from each of the numbered sectors shown in Fig. D-4, except those which have not yet been checked (those in the shaded area--Sector 1 and part of the sector containing the subject point P). The eight data points which correlate best with the point being examined (as determined from historical data) are used in the analysis. The flagging system is the same as described in the paragraph above. The second pass proceeds as the first, but data are accepted from all the sectors. In this pass it is presumed that if there are any spurious data above the point being examined (i.e., not yet checked on this pass), they have been flagged bad in the first pass or flagged suspect when they were used as a contributing observation on the second pass.

D. RECURSIVE FILTER

Quality control can be built into the analysis itself by adjusting the observation weights based on the observation difference from a first guess or, more commonly, from

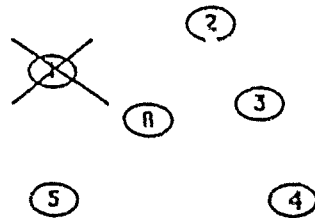
Original analysis for observation A



A= observation being checked
analysis location

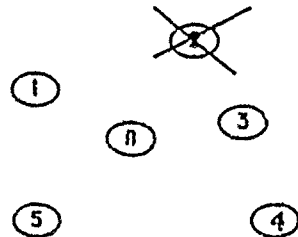
1...5 neighboring
observations

First reanalysis



Analysis is redone at point A
using observations 2 - 5.

Second reanalysis



Continue eliminating each
successive observation
while retaining all the others.

Fig. D - 3. Schematic of Successive Elimination Process

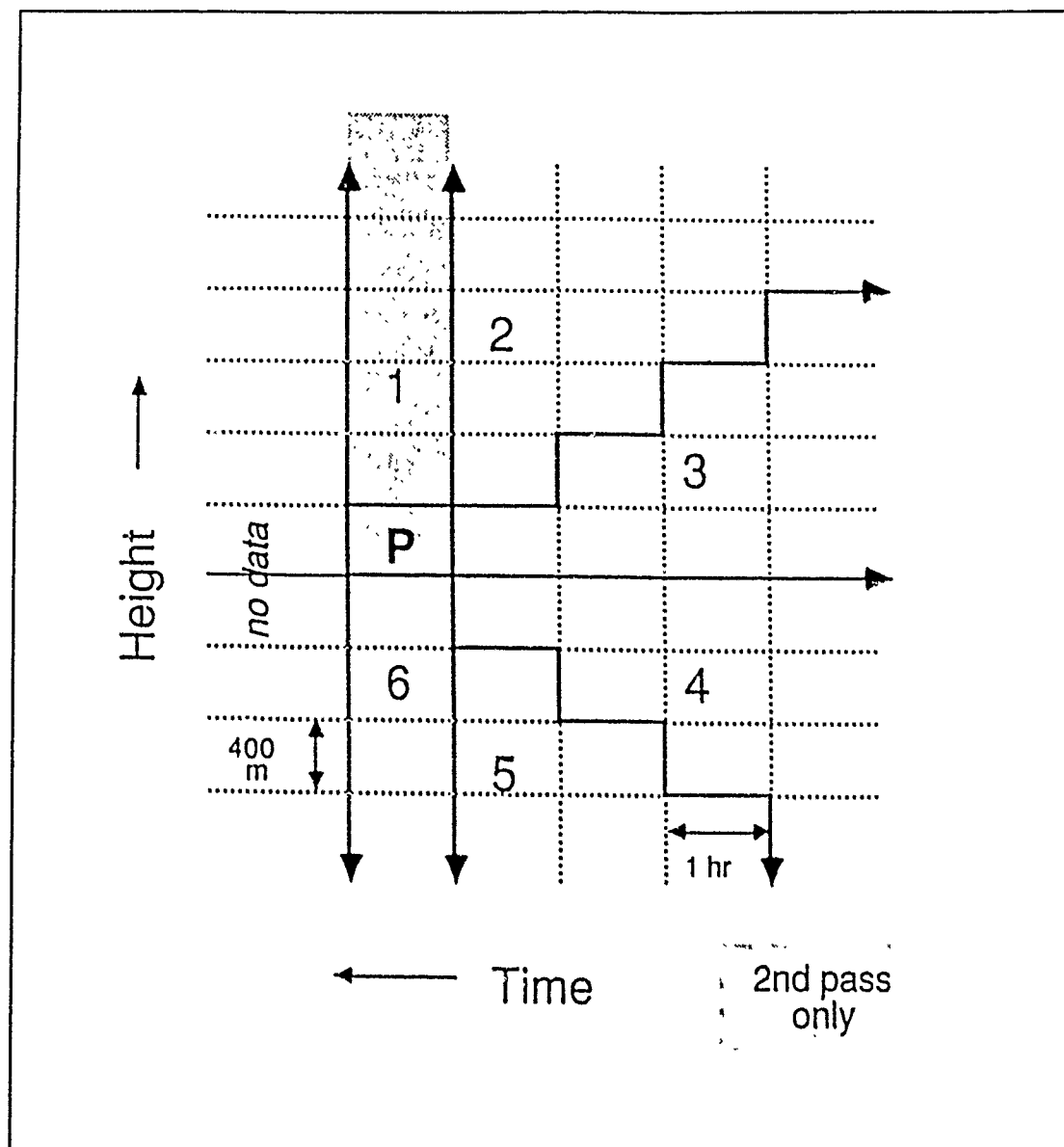


Fig. D-4. Data Search Strategy for Optimal Interpolation Analysis (OI)
 QC: Sector searching assures an even distribution of data around the datum being checked. Data within shaded area are excluded in the first pass; all sectors are searched in the second pass.

the previous analysis in a multiple pass (successive correction) analysis method. In this approach, data points are not discarded but are given a very small weight.

The recursive filter analysis uses bilinear interpolation to place the observed data (actually the difference from a first guess field) onto a regularly spaced grid. To smooth

the analysis, a numerical filter (similar to a weighted running average) is applied to the grid-point values. Then the process is repeated using the last analysis as a first guess. With each pass, the filter is modified so that less smoothing is done. Quality control is introduced by weighting each observation according to its difference from the previous analysis. One can discard an observation if its "quality weight" becomes very small, or, if the data density is high enough, one can presume that observations with very small weight will be overwhelmed by those with large weight (good quality observations). Because the recursive filter requires far less computation than optimal interpolation and no data searching it is much faster than OI. The speed depends upon the number of re-analysis passes necessary and the number of filter passes performed for each analysis pass. A good first guess can make the number of analysis passes very small (e.g., five) and can greatly increase the accuracy of the quality control decisions.

This technique has been tested on six-minute profiler data at PROFS. The analysis is done on a 100-m by 6-minute grid and the first guess consists of the median of 11 observations around each grid point. A time-to-space conversion which equates six minutes to 100 meters is used, and data are discarded (QC flag set to "bad") if their weight is less than 10^{-3} .

APPENDIX E. INDIVIDUAL PROFILER COMPARISONS AND RAWINSONDE LAUNCHINGS

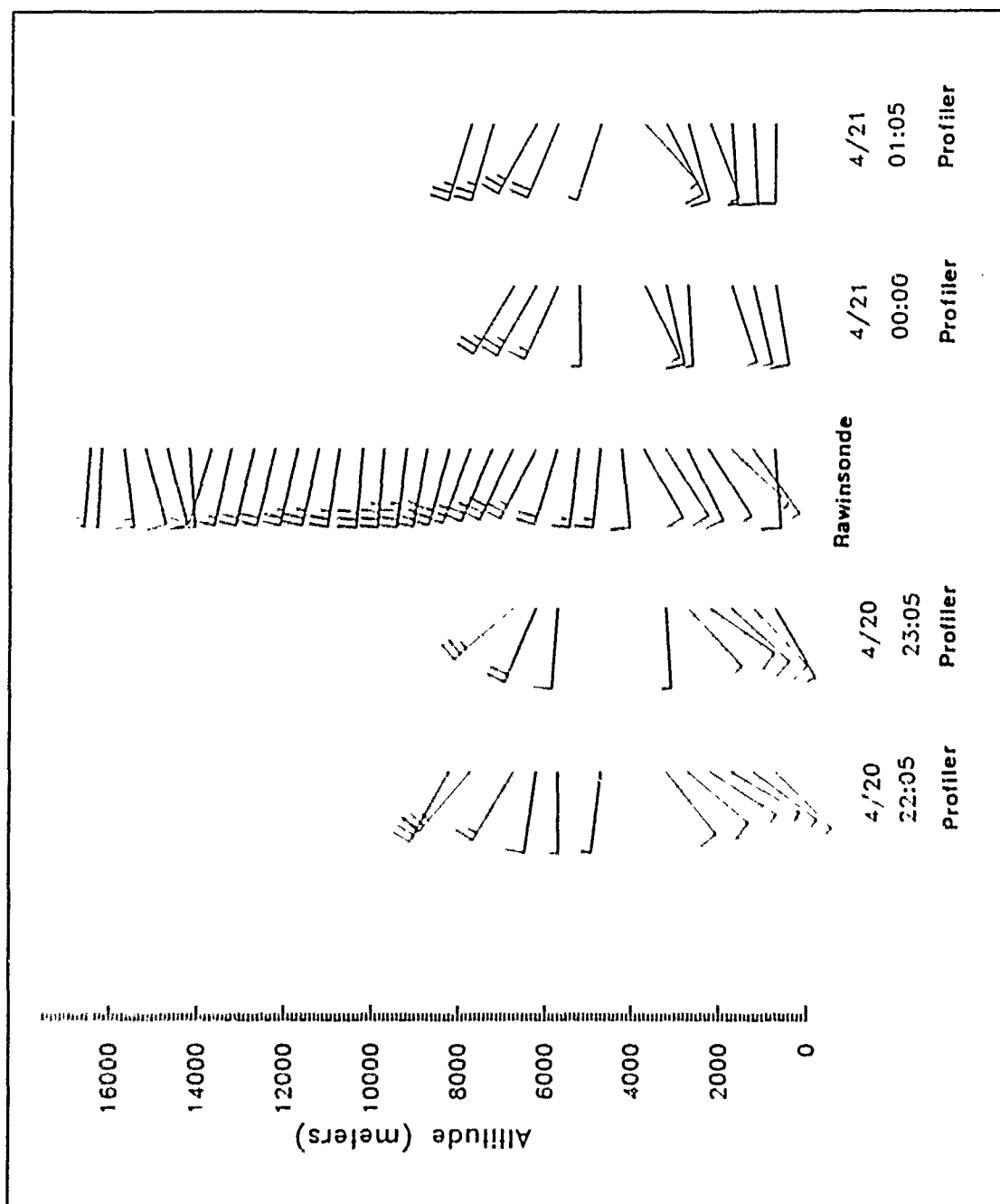


Fig. E - 1. Profiler-Rawinsonde Wind Comparisons for 20 April 1990

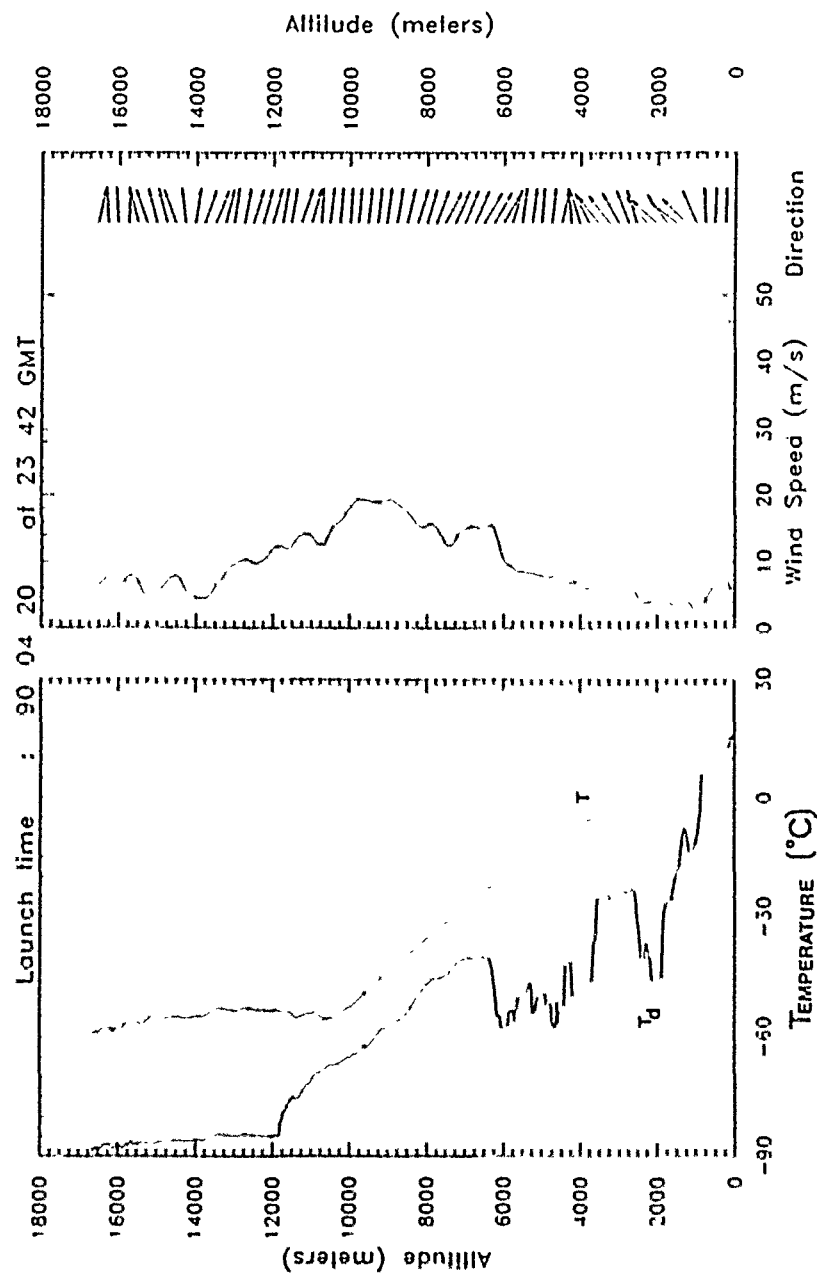


Fig. E-2. Rawinsonde Sounding from 20 April 1990

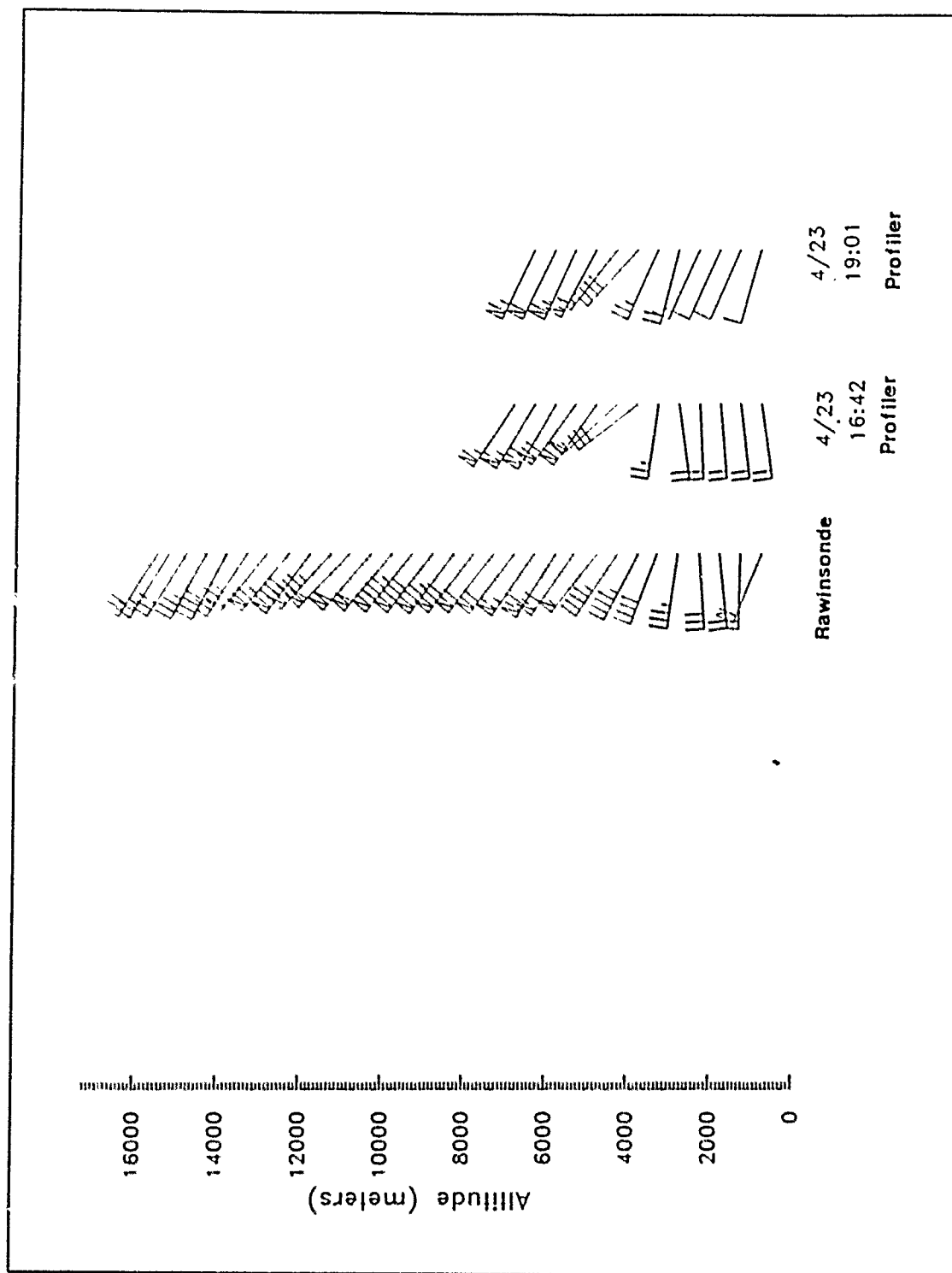


Fig. E - 3. Profiler-Rawinsonde Wind Comparisons for 1600 UTC 23 April 1990

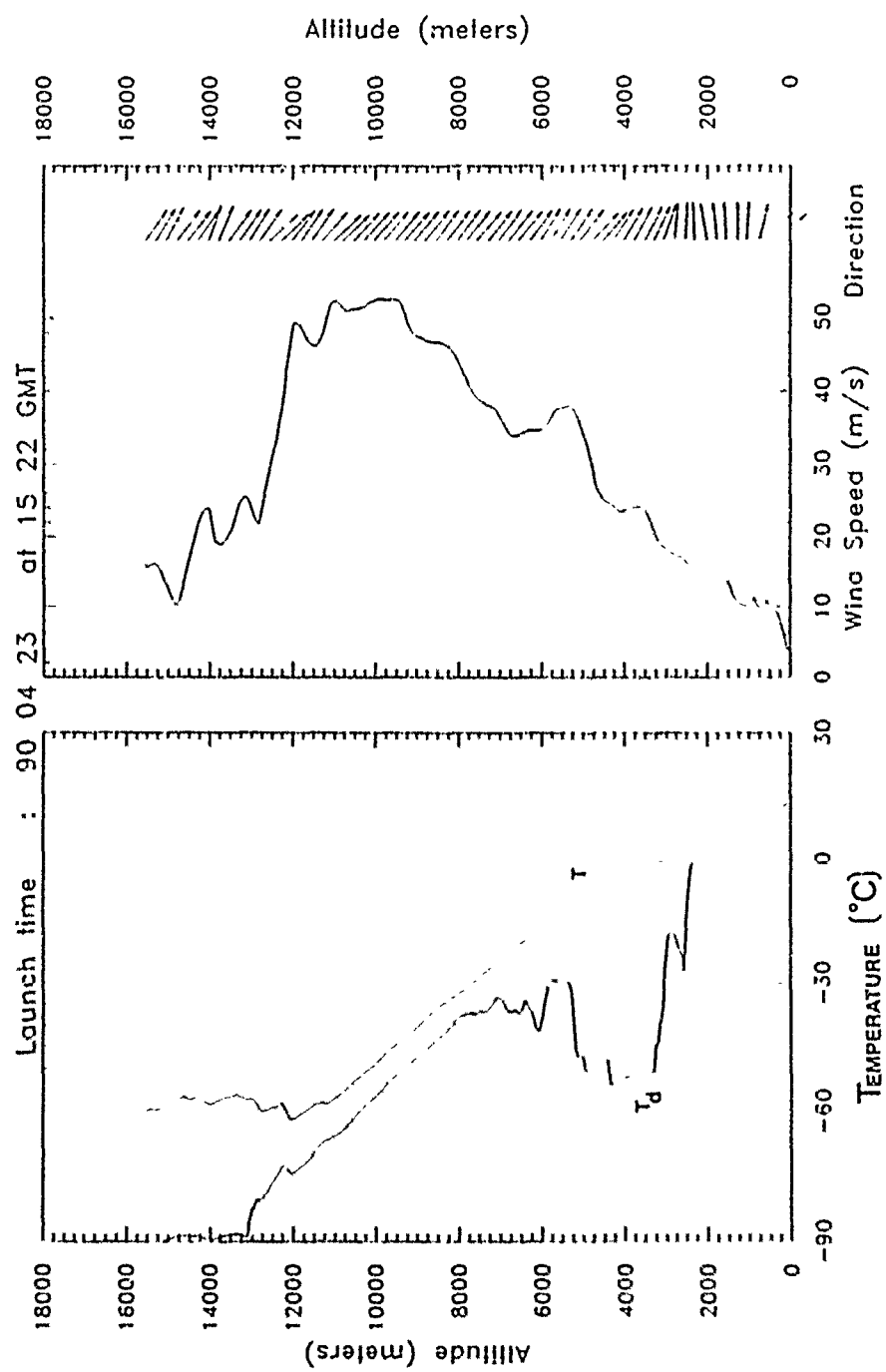


Fig. E-4. Rawinsonde Sounding from 1600 UTC 23 April 1990

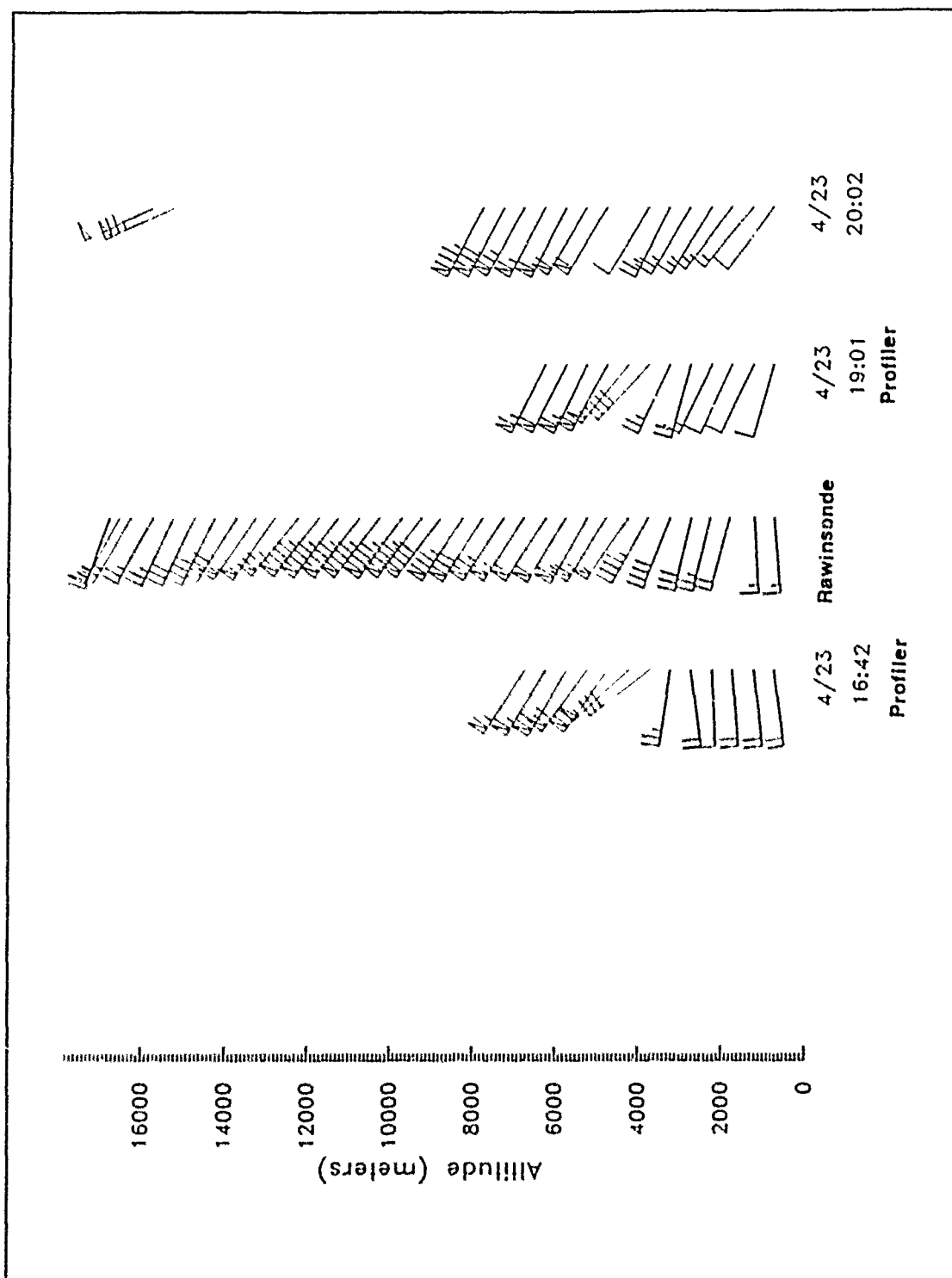


Fig. E - 5. Profiler-Rawinsonde Wind Comparisons for 1900 UTC 23 April 1990

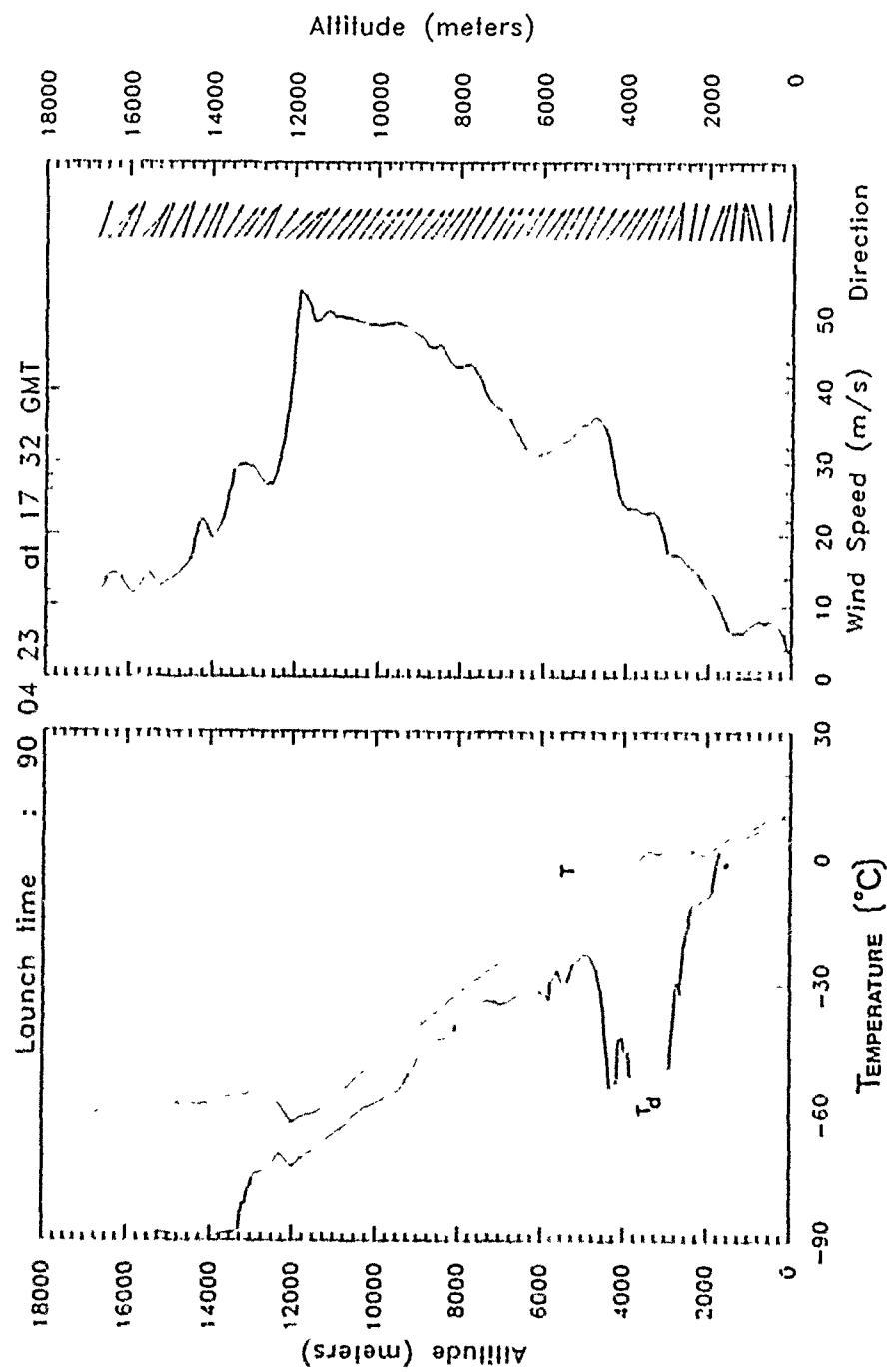


Fig. E-6. Rawinsonde Sounding from 1900 UTC 23 April 1990

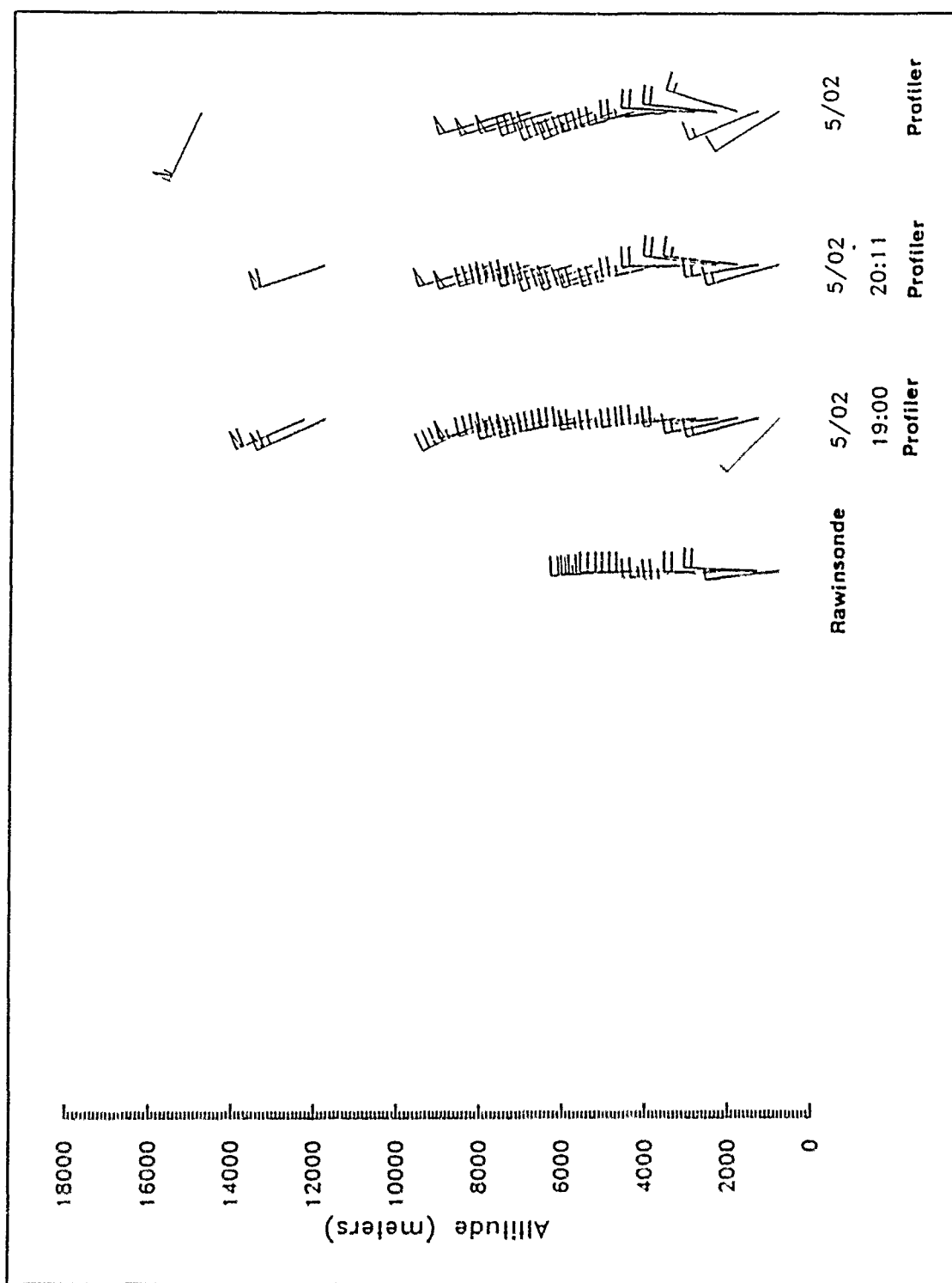


Fig. E-7. Profiler-Rawinsonde Wind Comparisons for 2000 UTC 02 May 1990

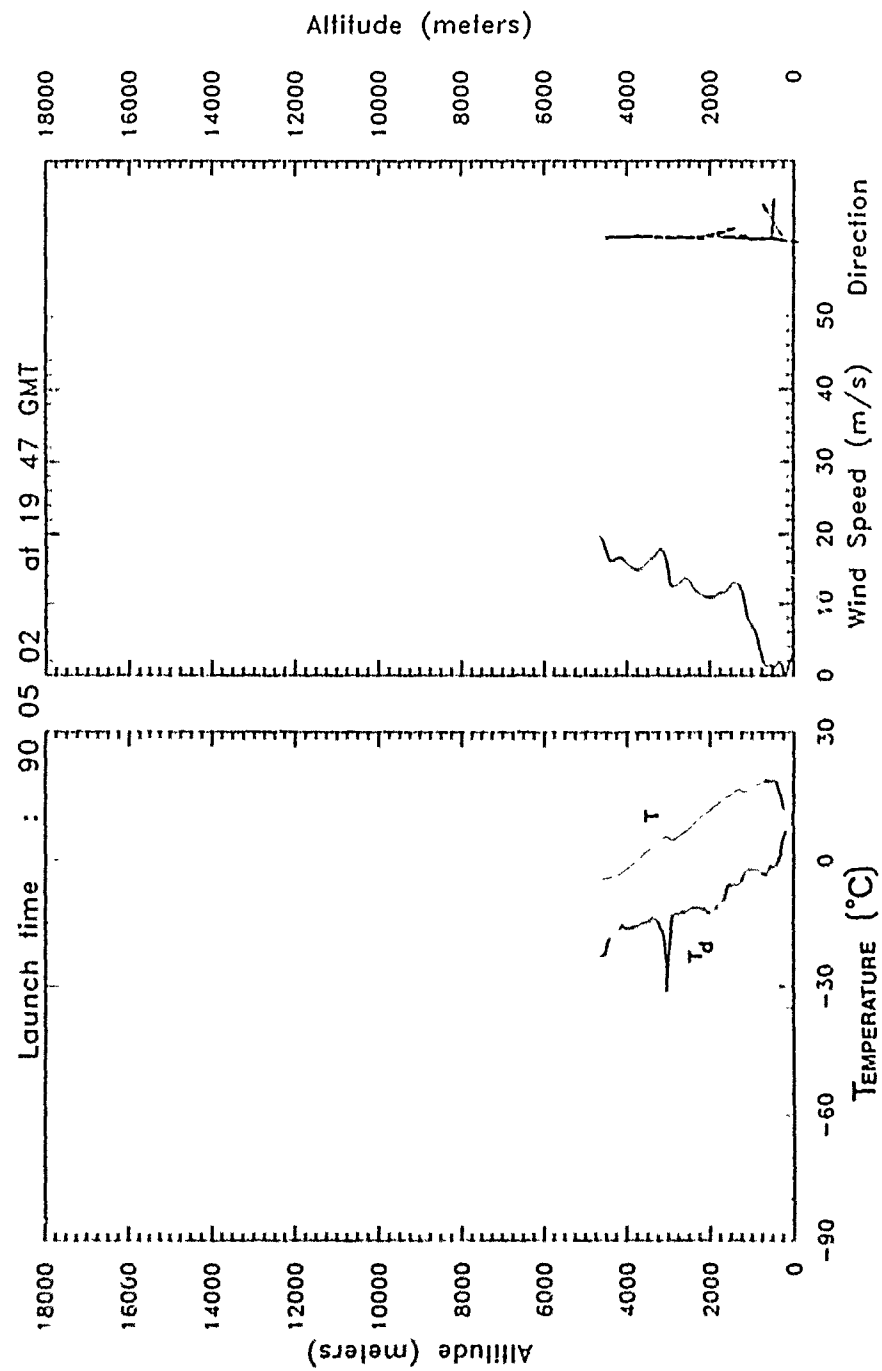


Fig. E-8. Rawinsonde Sounding from 1900 UTC 02 May 1990

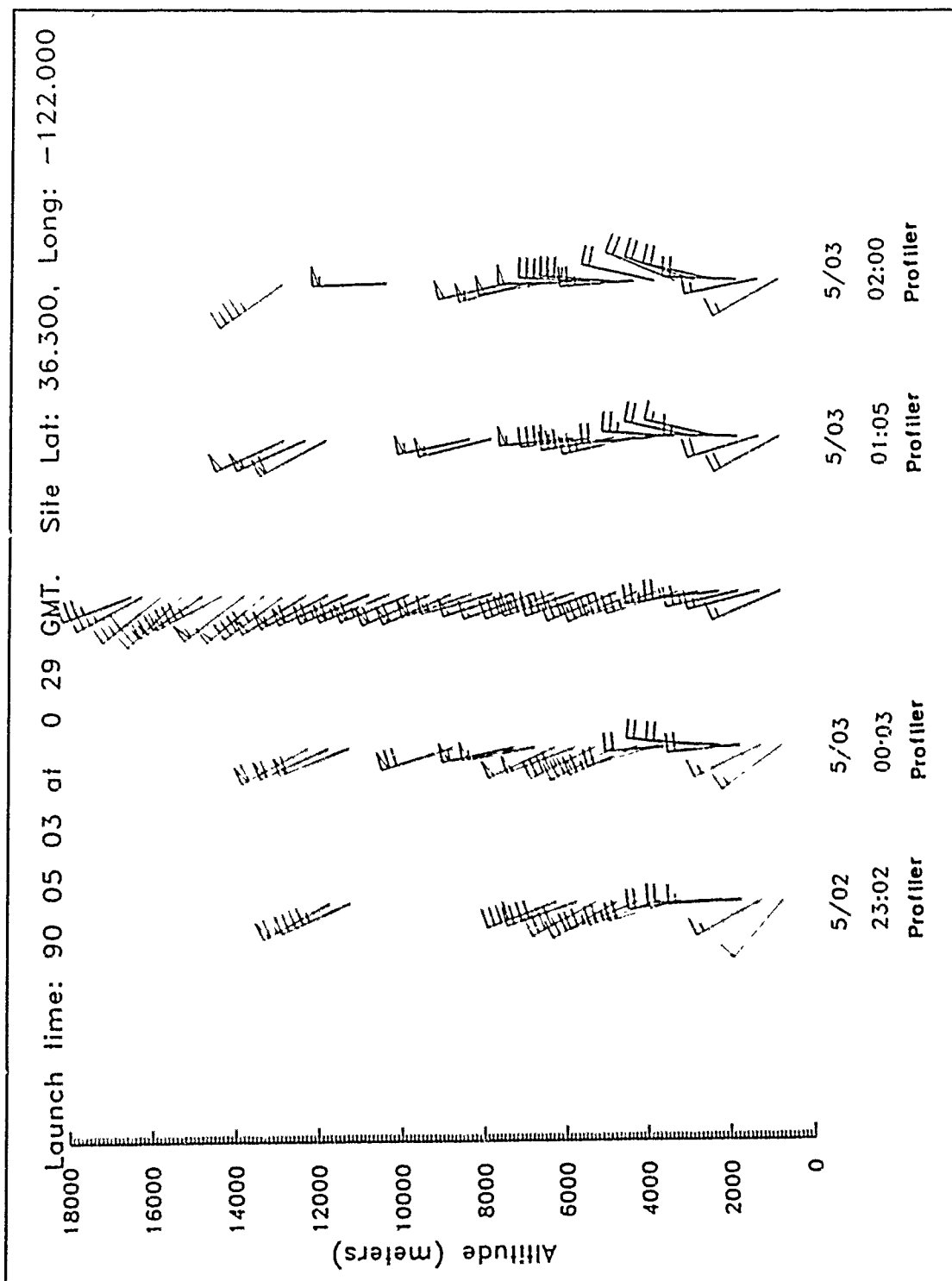


Fig. E-9. Profiler-Rawinsonde Wind Comparisons for 0100 UTC 03 May 1990

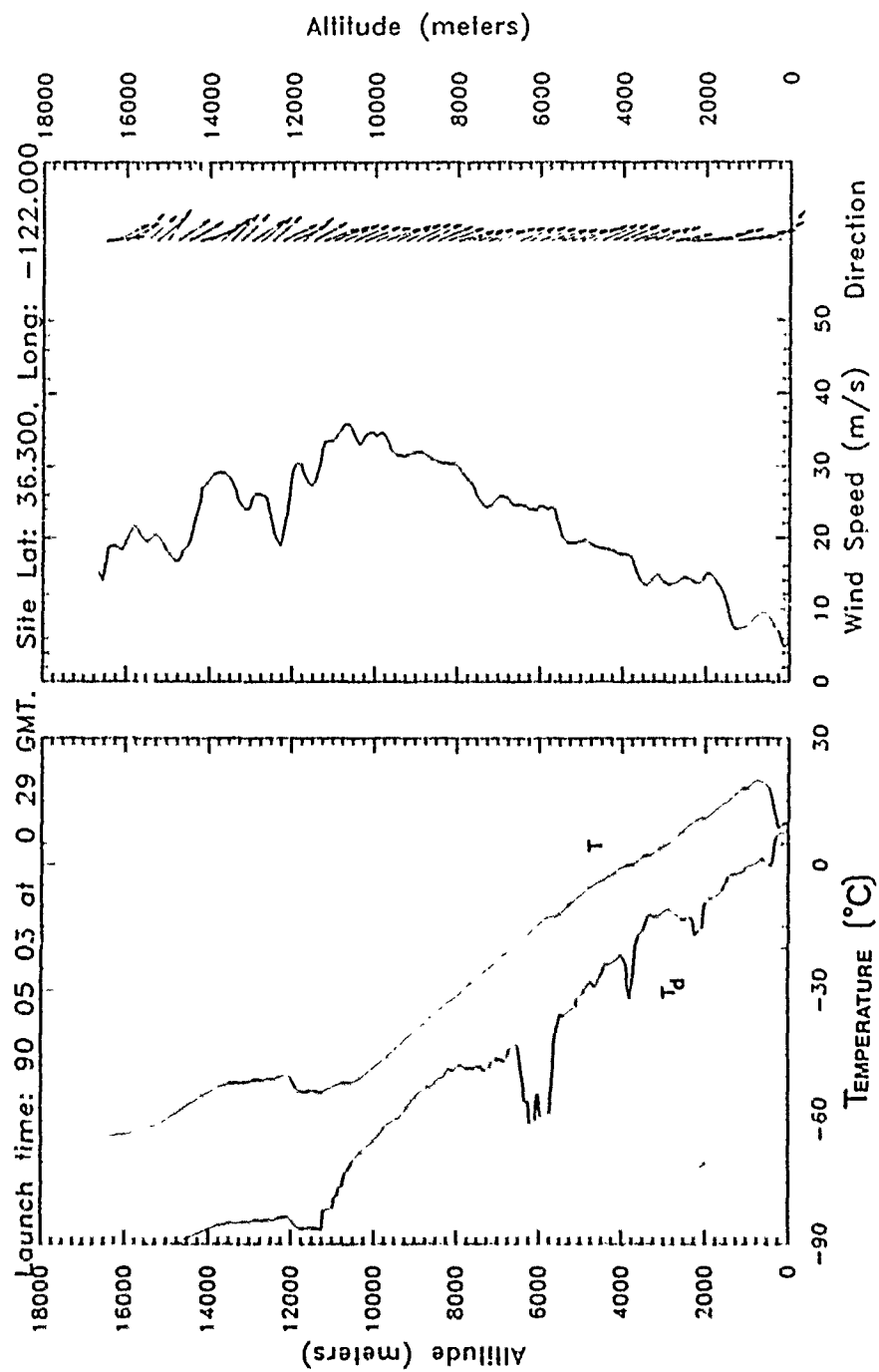


Fig. E-10. Rawinsonde Sounding from 0100 UTC 03 May 1990

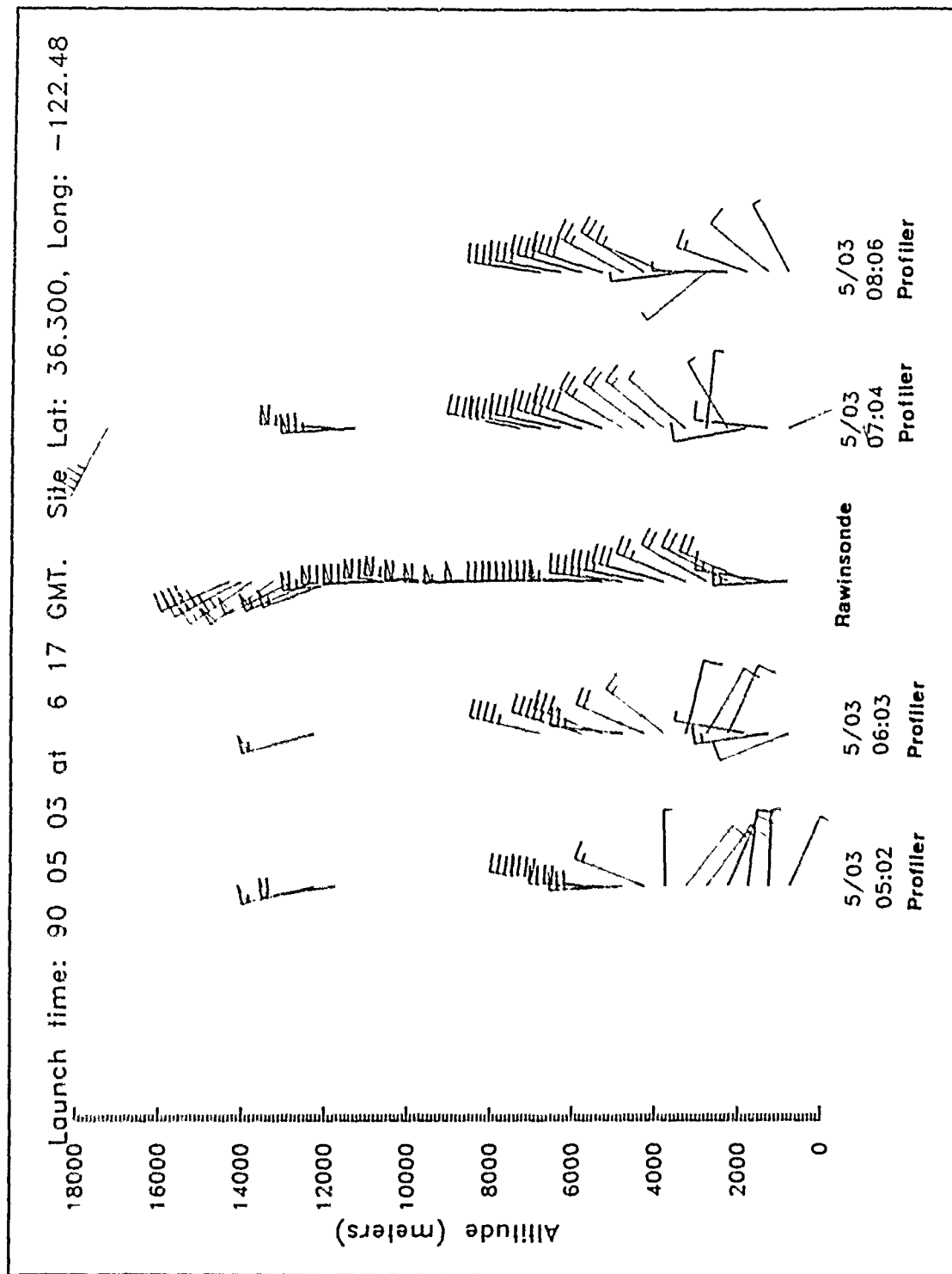


Fig. E - 11. Profiler-Rawinsonde Wind Comparisons for 0700 UTC 03 May 1990

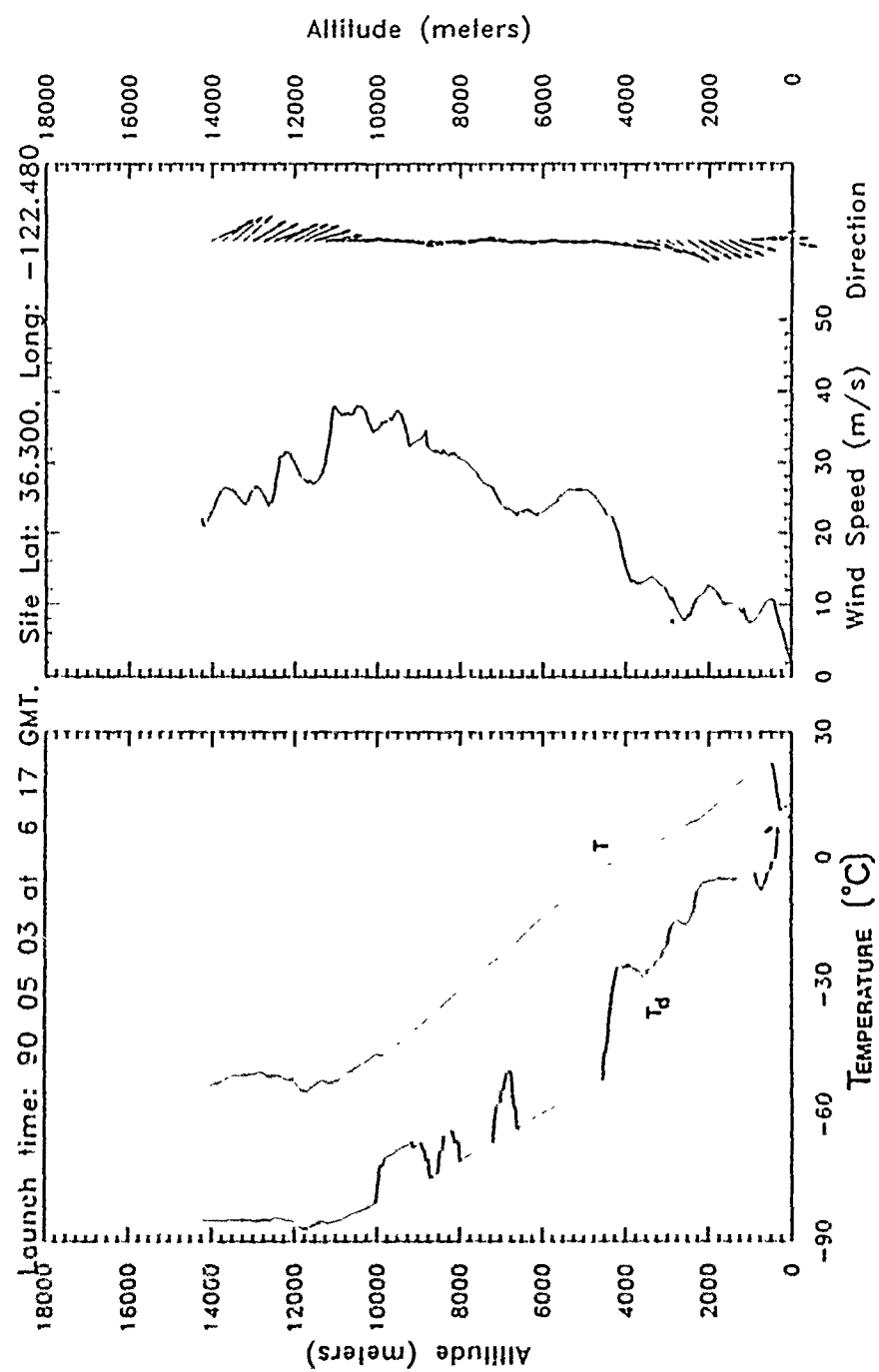


Fig. E - 12. Rawinsonde Sounding from 0700 UTC 03 May 1990

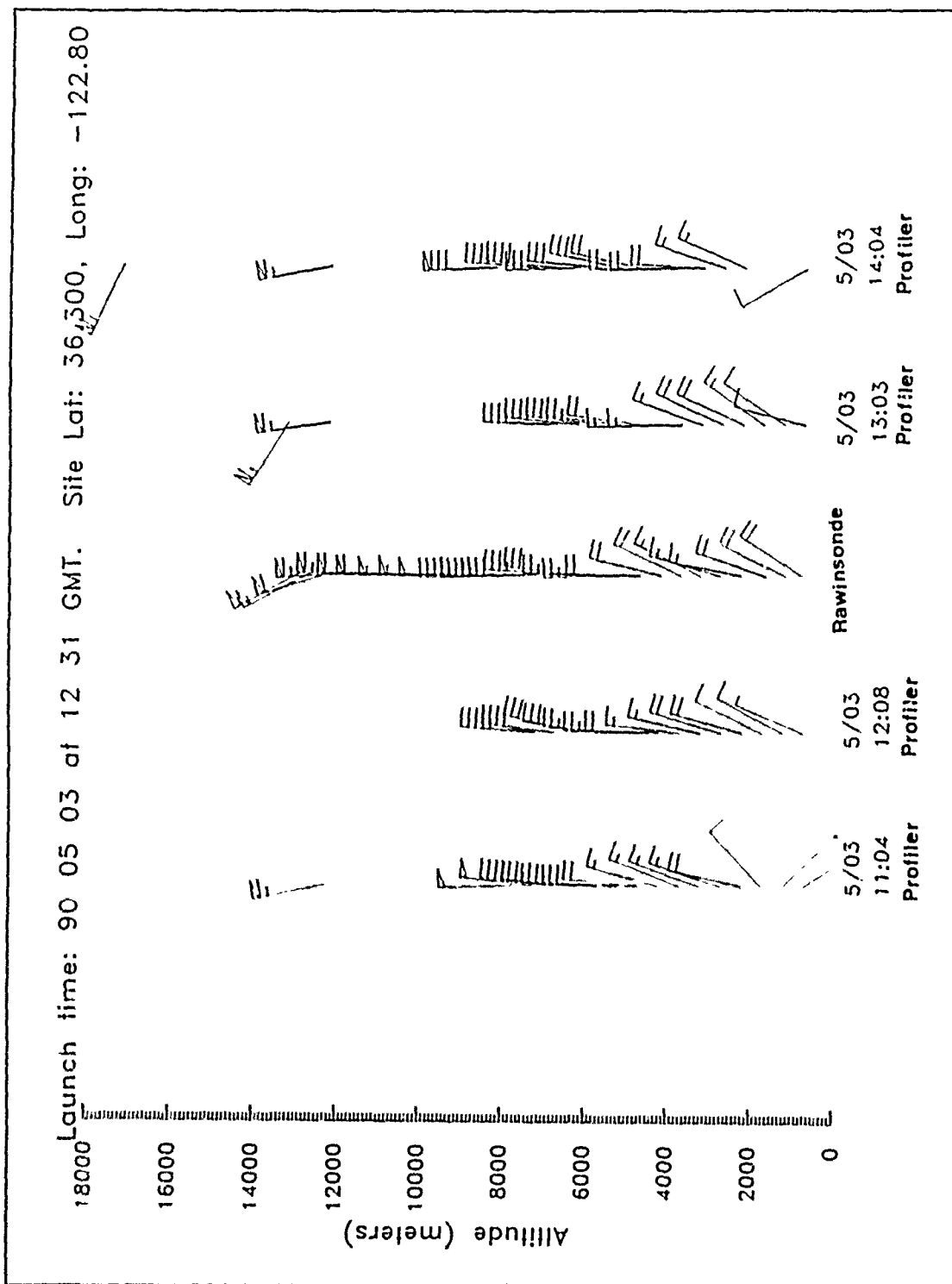


Fig. E-13. Profiler-Rawinsonde Wind Comparisons for 1300 UTC 03 May 1990

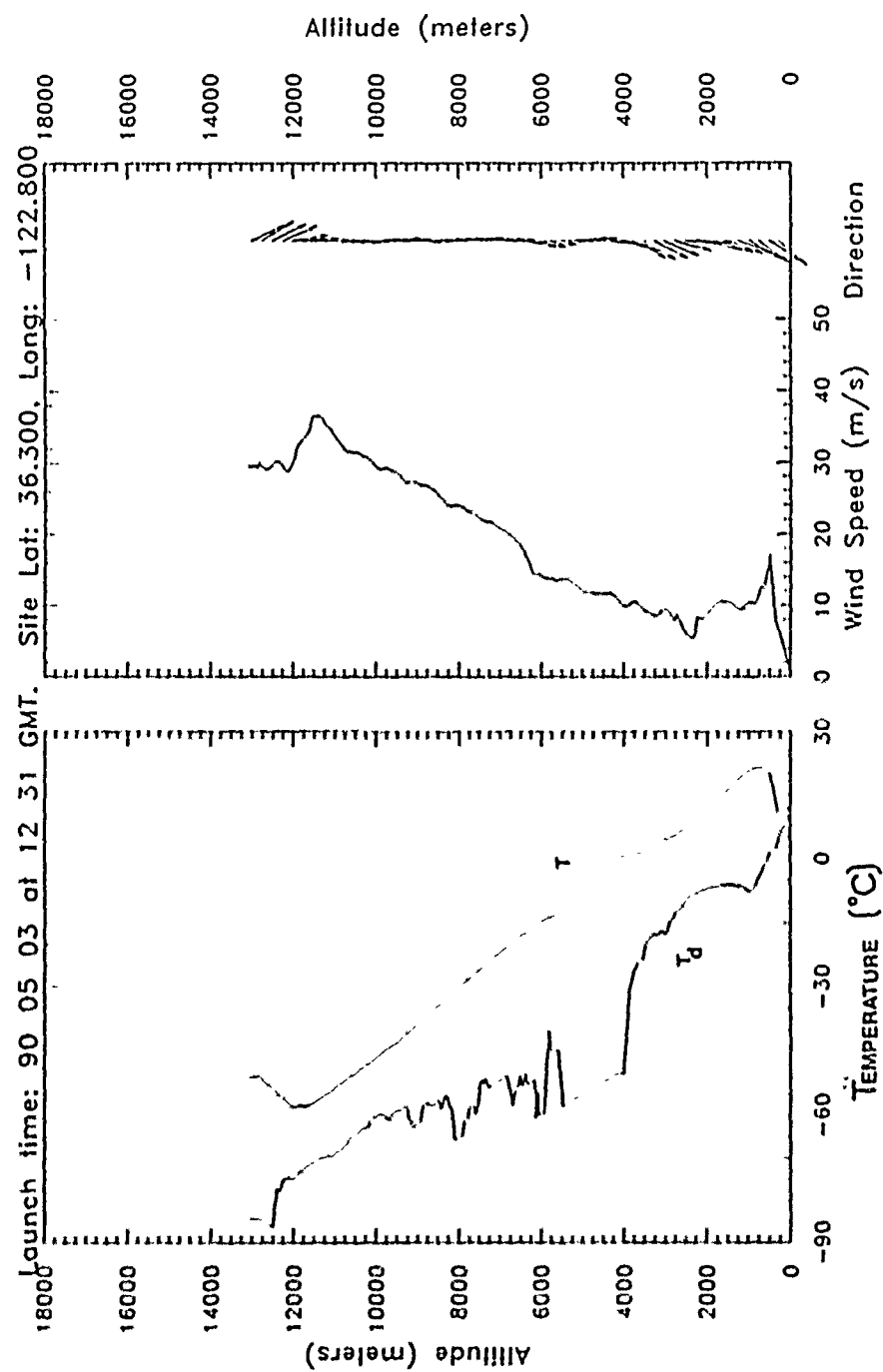


Fig. E - 14. Rawinsonde Sounding from 1300 UTC 03 May 1990

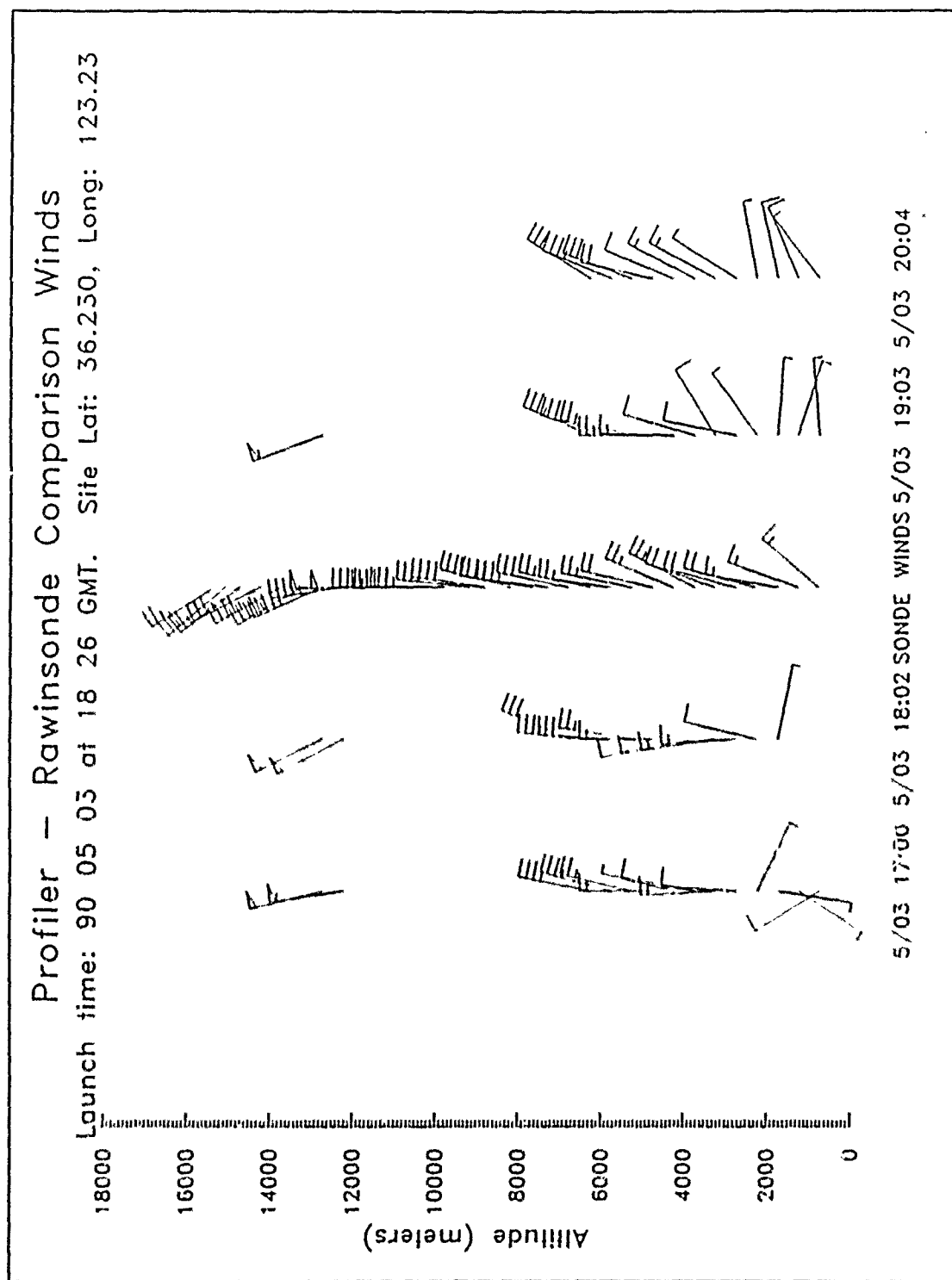


Fig. E-15. Profiler-Rawinsonde Wind Comparisons for 1900 UTC 03 May 1990

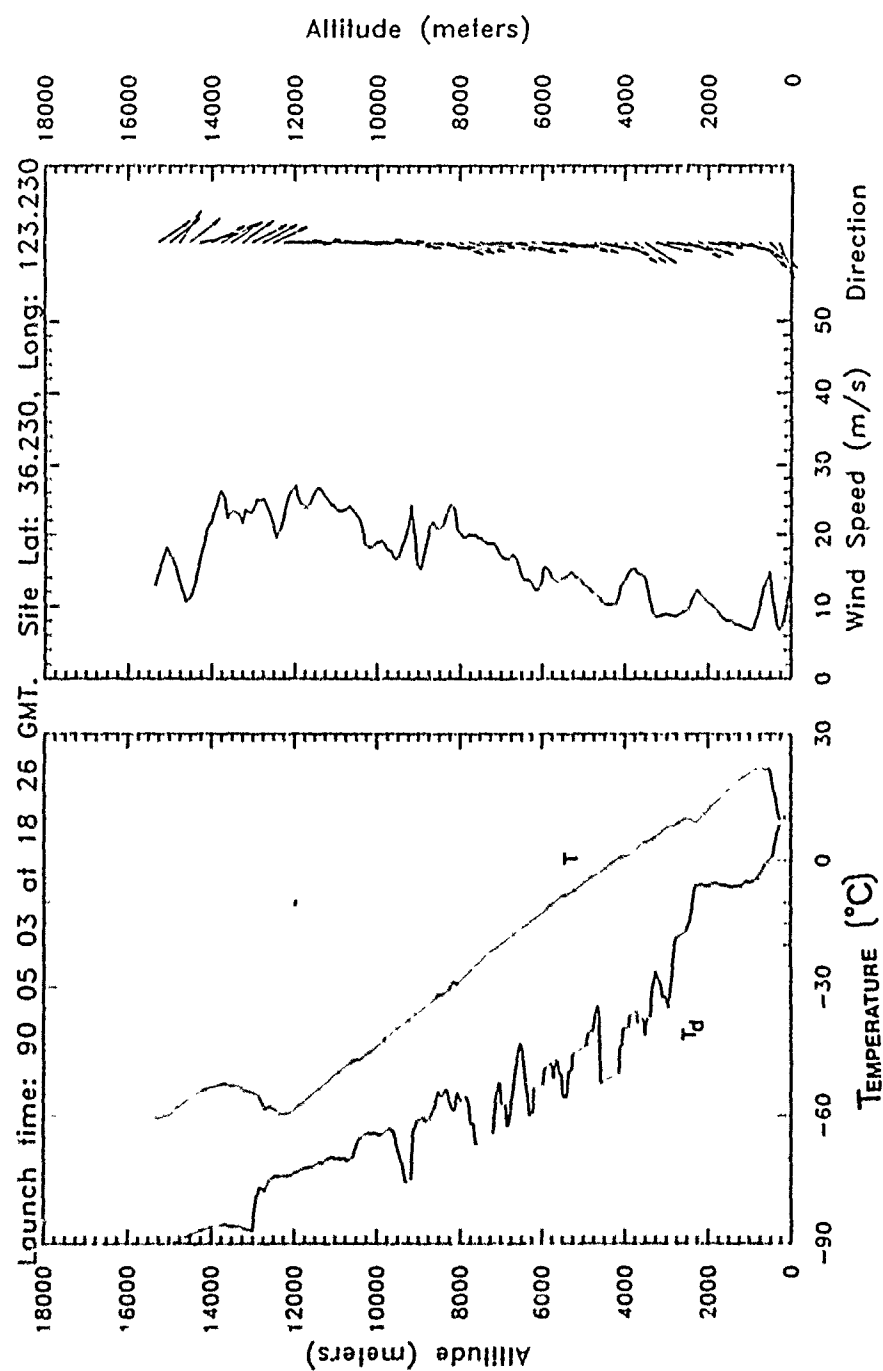


Fig. E-16. Rawinsonde Sounding from 1900 UTC 03 May 1990

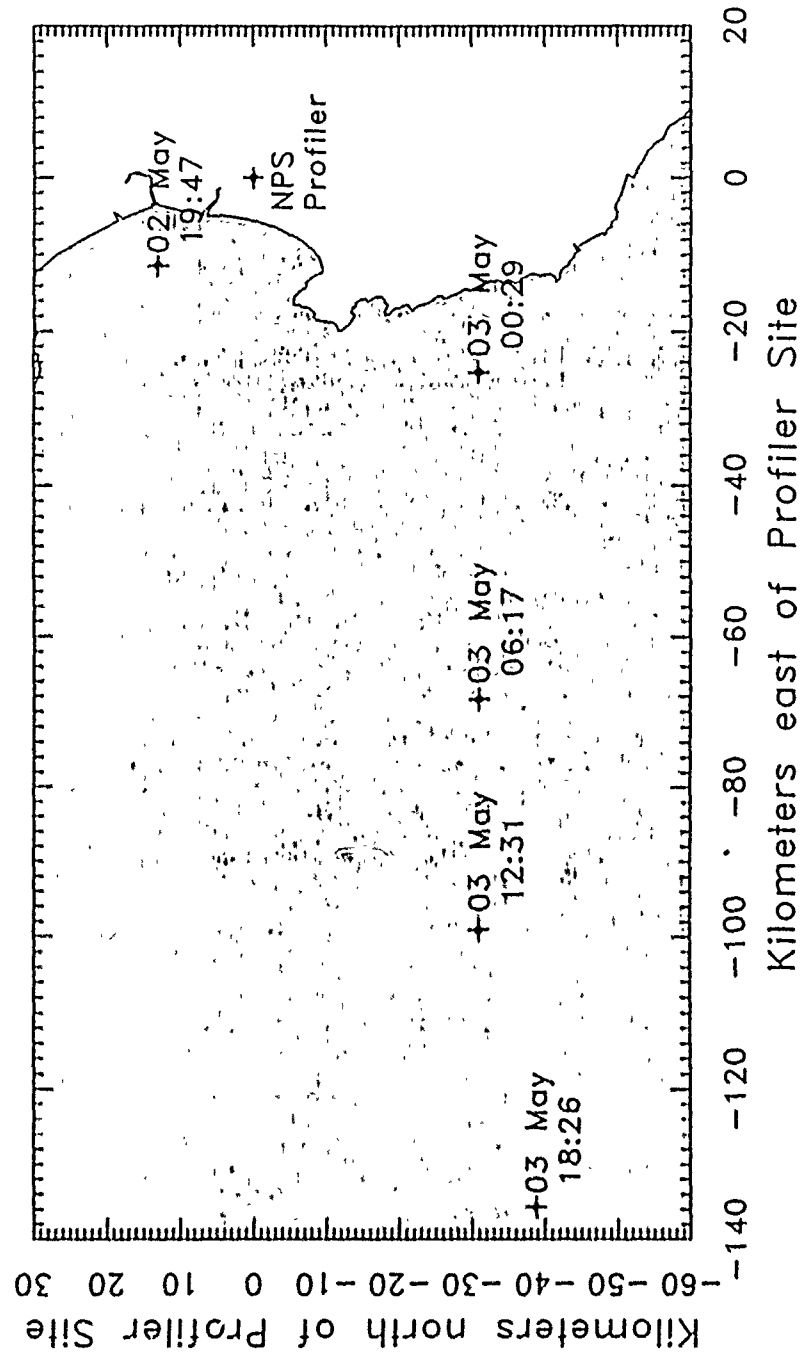


Fig. E-17. Rawinsonde Launch Locations: Rawinsonde launches were conducted at the NPS profiler site unless otherwise indicated here by their respective launch date and time.

APPENDIX F. NPS PROFILER SITE SURVEY RECORD AND LAYOUT

Naval Postgraduate School
Department of Oceanography

19 APR 90

From: Commander Kurt Schnebele, NOAA (Code OC/Sn)
To: Professor William Shaw (Code NR)

Subj: AZIMUTH & POSITION OF FORT ORD PROFILER

Encl: (1) Azimuth & Position Determination of Fort Ord Profiler
(2) Fort Ord Profiler Survey Worksheets
(3) Positions & Descriptions of Control Stations

1. At the request of LCDR Dan Streed, USN; Mr. James Cherry and I completed a survey to determine a geodetic azimuth and position for the profiler array at Fort Ord. The results are summarized below and discussed in Enclosure (1).

Azimuth of Side 336° 07.8' (linear error 95% = 3.3')
(western side)

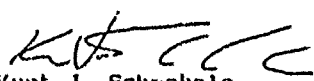
Azimuth of North 021° 07.8' (assuming array is square)
South Diagonal

Array Center N 36° 41' 43.716" (circular error 95%)
Position on W 121° 45' 29.824" (= 3 cm relative to)
NAD 83 datum (station DAIRY.)

Elevation 51 meters above sea level (NGVD 29)
Array Top

2. Note that the elevation was determined from only one point (station DAIRY). Lacking an independent check from another survey point, it is best to assume that elevation is only good to ±1 meter. Both the position and azimuth were determined using redundant measurements in a least-squares adjustment, which gave the precision estimates cited above.

3. Note that we set a new survey monument (DAIRY OFFSET) on the hill overlooking the profiler. If needed, the azimuth could be checked from there in the future.


Kurt J. Schnebele
Commander, NOAA

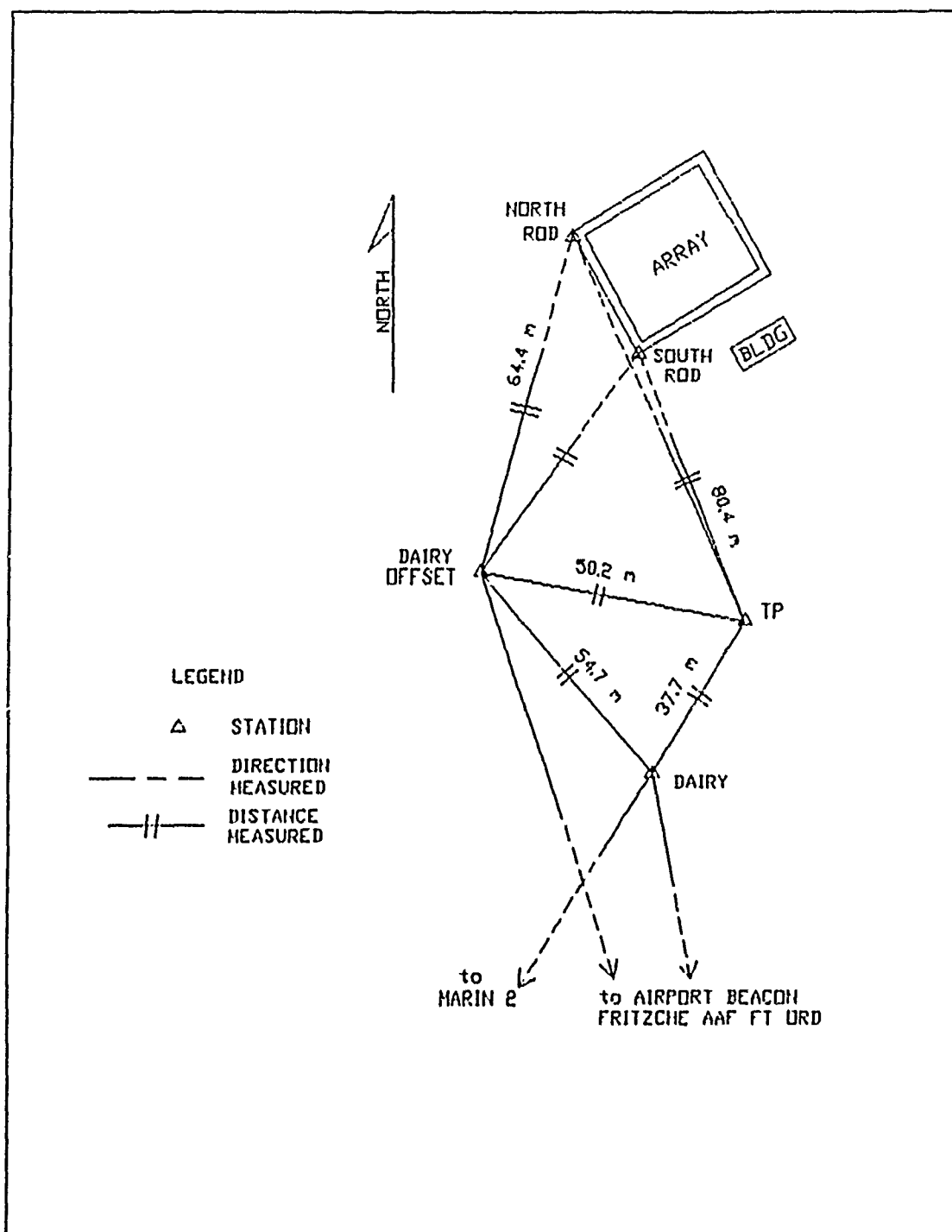


Fig. F-1. Atmospheric Profiler, Fort Ord Survey Observation Sketch: Conducted 19 April 1990 by Cdr. Schnebele (no scale).

APPENDIX G. HIGH-FREQUENCY METEOROLOGICAL DATA

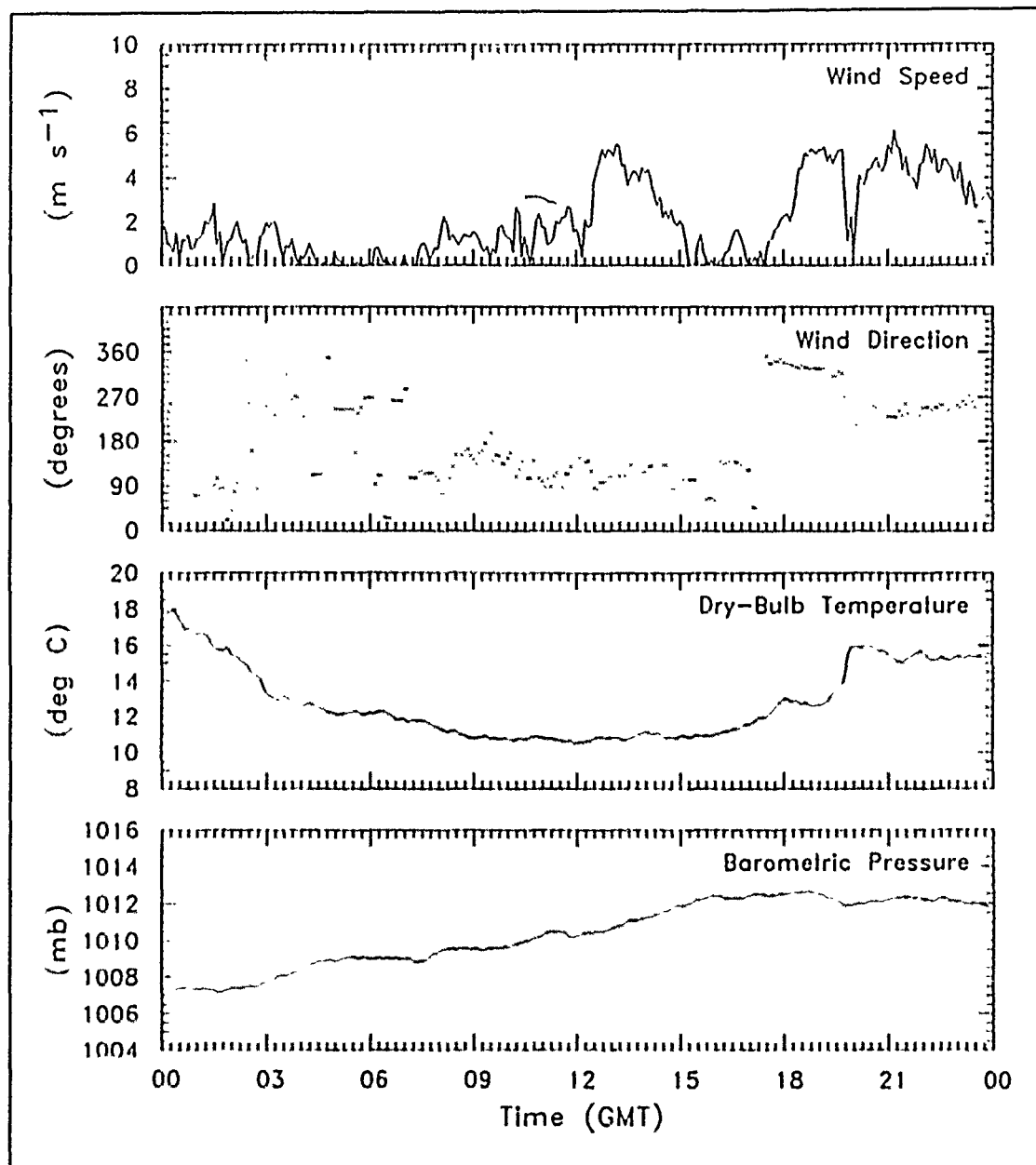


Fig. G-1. Recorded Data for 03 May 1990.: From the Monterey Bay Aquarium Research Institute.

LIST OF REFERENCES

- Balsley, B.B., and K.S. Gage, 1980: The MST radar technique: potential for middle atmospheric studies. *Pure Appl. Geophys.*, 118, 452-493.
- Batten, L.J., 1973: Radar observation of the atmosphere. University of Chicago Press, Chicago, 324pp.
- Brady, R.H., and K.A. Brewster, 1989: Profiler training manual 3. NOAA/ERL Boulder, Colorado, 103pp.
- Brewster, A.B., 1989: Quality control of wind profiler data, profiler training manual 2. NOAA/ERL Boulder, Colorado, 39pp.
- Cage, K.S., 1990: Radar in meteorology; chapter 28a, Radar observations of the free atmosphere: structure and dynamics. Amer. Met. Society, Boston, 534-565.
- Campbell, R.G., 1973: Foundations of fluid flow theory, 428pp.
- Dorman, C.E., 1985: Evidence of Kelvin waves in California's marine layer and related eddy generation, *Monthly Weather Review*, 113, 827-839.
- Doviak, R.S., and D.S. Zrnic, 1984: Doppler radar and weather observations. Academic Press, 485pp.
- Forbes, Gregory S., D.W. Thomson, J.J. Cahir, C.A. Carlson, P.J. Neiman, S.R. Williams, and A.A. Person, 1989: Analysis of significant weather on meso-alpha scales using conventional and remotely-sensed data. Pennsylvania State University, Final Report October 1984-September 1985, 228pp.
- , T. Dye, M. Lee, D.N. Thomson, J.J. Cahir, S.R. Williams, and A.A. Person, 1990: Analysis of significant weather on meso-alpha scales using conventional and

- remotely-sensed data--further studies. Pennsylvania State University, Final Report February 1986-February 1988, 116pp.
- Gill, A.E., 1982: Atmospheric-ocean dynamics. Academic Press, Orlando, 662pp.
- Gossard, E.E., and R.G. Strauch, 1983: Radar observation of clear air and clouds. El Sevien Science Publishing, New York, 286pp.
- , 1990: Radar in meteorology, radar research on the atmospheric boundary layer. Amer. Met. Society, Boston, Chaper 27a, 51pp.
- Holton, J.R., 1979: An introduction to dynamic meteorology. Second edition, Academic Press, Orlando, 391pp.
- Kuo, Ying-Hwa, D.O. Gill, and L. Cheng, 1987: Retrieving temperature and geopotential fields from a network of wind profiler observations. *Monthly Weather Review*, 115, 3146-3165.
- , Yang-Run Guo, and M.A. Shapiro, 1989: *Profiler Forum*, March.
- McGillen, and Cooper, 1974: Continuous and discrete signal and system analysis. Holt, Rinehart, and Winston, New York, NY, 395pp.
- Peterson, Vern L., 1988: The history, principles, and applications of clear-air doppler radar. Tycho Technologies, Inc., 26pp.
- Röttger, J. and M.F. Larsen, 1990: UHF/VHF radar techniques for atmospheric research and wind profiling radar applications in meteorology, 806pp.
- Strauch, R.G., 1981: Radar measurement of tropospheric wind profiles. *Preprints, 20th Conference on Radar Meteorology*, Boston, Amer. Meteor. Soc., 430-434.
- , B.L. Weber, A.S. Frisch, C.G. Little, D.A. Merritt, K.P. Moran, and D.C. Welsh, 1987: The precision and relative accuracy of profiler wind measurements. *J.Atmos.Oceanic Technol.*, 4, 563-571.

- Stull, Roland B., 1988: An introduction to boundary layer meteorology. Kluwer Academic Publisher, Boston, 666pp.
- Thomson, D.W., and S.R. Williams, 1990: Analysis of comparative wind profiler and radiosonde measurements. Preprints, 10th Int'l Geosc. Remote Sensing Symp., College Park, MD, pp537-540.
- van de Kamp, Douglas W., 1988: Profiler training manual 1, principles of wind profiler operation. NOAA/ERL Boulder, Colorado, 49pp.
- Waterman, A.T., T.Z. Hu, P. Czechowsky, and J. Röttger, 1985: Measurement of anisotropic permittivity structure of the upper troposphere with clear-air radar. *Radio Sci.*, 20, 1580-1592.
- Weber, B.L., and D.B. Wuertz, 1990: Comparison of rawinsonde and wind profiler radar measurements. *Journal of Atmos. and Oceanic Technology*, 7, 157-174.
- Winant, C.D., C.E. Dorman, C.A. Friehe, and R.C. Beardsley, 1988: The marine layer off northern California: an example of supercritical channel flow. *J. Atmos. Sci.*, 45, 3588-3605.
- Woodman, R.F., and A. Guillen, 1974: Radar observations of winds and turbulence in the stratosphere and mesosphere, *J. Atmos.Ocean.Tech.*, 1, 37-49.
- Wuertz, D.B., B.L. Weber, R.G. Strauch, A.S. Frisch, C.G. Little, D.A. Merritt, K.P. Moran, and D.C. Welsh, 1988: Effects of precipitation on UHF wind profiler measurements. *J. Atmos. Oceanic Tech.*, 5, 450-465.
- Zamora, R.J., and M.A. Shapiro, 1988: Wind profiler observations of a pre-convective environment, *Journal of Atmospheric Sciences*, 148-155.

INITIAL DISTRIBUTION LIST

	No. Copies
1. Defense Technical Information Center Cameron Station Alexandria, VA 22304-6145	2
2. Library, Code 52 Naval Postgraduate School Monterey, CA 93943-5002	2
3. Chairman (Code MR/Hy) Department of Meteorology Naval Postgraduate School Monterey, CA 93943-5000	1
4. Professor Wendell A. Nuss (Code 63NU) Department of Meteorology Naval Postgraduate School Monterey, CA 93943-5000	2
5. Professor Carlyle H. Wash (Code 63WX) Department of Meteorology Naval Postgraduate School Monterey, CA 93943-5000	1
6. Ledr. Daniel H. Streed, USN OA Div, USS Forrestal CV-59 FPO Miami, FL 34080-2730	1
7. Commander Naval Oceanography Command Stennis Space Center, MS 39529-5000	1
8. Commanding Officer Naval Ocean Research and Development Activity Stennis Space Center, MS 39529-5004	1
9. Commanding Officer Fleet Numerical Oceanography Center Monterey, CA 93943-5005	1
10. Director Naval Oceanographic and Atmospheric Research Laboratory Monterey, CA 93943-5006	1

- | | | |
|-----|---|---|
| 11. | Chief of Naval Research
800 North Quincy Street
Arlington, VA 22217 | 1 |
| 12. | Office of Naval Research (Code 420)
Naval Ocean Research and Development Activity
800 N. Quincy Street
Arlington, VA 22217 | 1 |